THE ASTROPHYSICAL JOURNAL, 342:306–336, 1989 July 1

MOLECULE FORMATION AND INFRARED EMISSION IN FAST INTERSTELLAR SHOCKS. III. RESULTS FOR *J* SHOCKS IN MOLECULAR CLOUDS

DAVID HOLLENBACH
NASA Ames Research Center

AND

CHRISTOPHER F. MCKEE
Departments of Physics and of Astronomy, University of California, Berkeley
Received 1988 June 15; accepted 1988 November 23

ABSTRACT

The structure and emission-line spectra of fast ($v_s = 30$–150 km s^{-1}), steady interstellar shocks in molecular gas at densities $n_0 = 10^3$–10^6 cm^{-3} are presented. The results are for *J* shocks, in which the shock front is treated as a discontinuity and ambipolar diffusion is negligible. The relative concentrations of H_2, H, and H^+ entering the shock front are determined by the photoionizing precursor, for which a theory is developed. In almost the entire parameter space studied, the H_2 is completely dissociated, either by the precursor field or by collisions in the shock, and then is reformed on grain surfaces over a column density $\sim 10^{21-22}$ cm^{-2} downstream. A chemical reaction network follows the chemistry of H, C, O, and, to a lesser extent, Si. The radiative cooling of the gas is partially offset by heating due to absorption of UV radiation from the hot gas near the shock front and due to the release of chemical energy by the formation of H_2.

The spectra of fast *J* shocks show the following features: (1) H_2 emission is dominated by collisional excitation in the low-*J* rotational lines and by formation pumping in the high-*J* rotational lines and the vibrational lines; as a result, the H_2 spectrum can mimic that of pumping by ultraviolet radiation. The intensity of the 1–0 *S*(1) line is less than 10^{-3} ergs cm^{-2} s^{-1} sr^{-1}, far less than in *C* shocks in dense gas and far less than inferred in many sources. (2) O I(63 μm) is proportional to the particle flux through the shock for $n_0 v_s \leq 10^{12}$ cm^{-2} s^{-1}. O I(63 μm)/C II(158 μm) is a good discriminant between *J* shocks and photodissociation regions when the O I line is strong. The line to continuum ratios and the line profiles may also discriminate *J* shocks from photodissociation regions. (3) Ne II(12.8 μm) and Si II(35 μm) are good discriminants between *J* shocks and *C* shocks, since *C* shocks have very low ionic abundances. (4) S I(25 μm), C II(11.4 μm), Fe I(24 μm), Fe II(26 μm), Fe II(35 μm), and Ni II(6.6 μm) are predicted in *J* shocks in dense ($n_0 \gtrsim 10^5$ cm^{-3}) gas. (5) C I λ9849, N I(1.04 μm), Fe II(1.3 μm), and Fe II(1.7 μm) are predicted to be strong near infrared emission lines. (6) Intensities of CO rotational lines, of the total intensity of OH and H_2O rovibrational cooling, and of Hα, Hβ, Pα, Pβ, Brα, Brβ, and Brγ are also given.

These results have direct application to Herbig-Haro objects, winds from protostars, supernova remnants in molecular clouds, and H_2O masers. The prime diagnostics for a *J* shock in the protostellar outflow source in the BN-KL region of Orion are the infrared hydrogen lines and the fine structure lines of ions such as Si^+. Broad, intense O I(63 μm) emission is predicted to be the signature of supernova remnants "buried" in molecular clouds. The temperature plateau produced by H_2 formation heating behind *J* shocks in dense gas ($n_0 \gtrsim 10^6$ cm^{-3}) provides an ideal site for H_2O maser emission.

Subject headings: interstellar: grains — interstellar: molecules — molecular processes — shock waves

I. INTRODUCTION

Interstellar molecular clouds are frequently traversed by shock waves which compress, heat, chemically alter, and accelerate the ambient gas. These shock waves are driven by a variety of sources including stellar winds, expanding H II regions, cloud-cloud collisions, and supernova blast waves, Over the past decade, it has become increasingly clear that high-velocity outflows are a common occurrence in protostars and that the interaction of this pre–main-sequence wind with the surrounding natal molecular cloud is probably the dominant source of strong shocks in many molecular clouds (see, e.g., Bally and Lada 1983). Herbig-Haro objects are likely manifestations of such a shock phenomenon (see, Schwartz 1983).

Molecular shocks generally can be described as "*C* shocks" or as "*J* shocks" (Draine 1980), depending on their velocity v_s, the ambient ionization fraction, and the strength of the component of the ambient magnetic field $B_{0\perp}$ perpendicular to v_s. In *C* shocks, gas is accelerated and heated by collisions between charged particles (which have a low abundance and are coupled to the magnetic field) and neutral particles; this ambipolar heating persists throughout the radiating region, the neutral gas temperature rarely exceeds 3000–4000 K, and the emission is almost entirely infrared emission lines—often vibrational or rotational transitions of H_2, CO, and H_2O. The *C* shocks occur in weakly ionized molecular gas for shock velocities below $\sim$40–50 km s^{-1} (Chernoff *et al.* 1982). In *J* shocks, gas properties "jump" from their preshock to their postshock values in a shock front with a thickness less than one mean free path (the initial compression, acceleration and all the shock heating are delivered without appreciable radiation). The *J* shock radiation is emitted downstream behind the shock front, primarily in the visible and ultraviolet, but with a few strong infrared lines such as O I(63 μm). The *J* shocks occur in ionized or neutral atomic gas, or at high veloc-

ities ($v_s > 40$–50 km s^{-1}) in molecular gas; in the latter case, the shocks dissociate the ambient molecules (see, e.g., McKee, Chernoff, and Hollenbach 1984). The UV radiation emitted from J shocks can flow upstream and preionize or predissociate the gas. A recent review of C shocks, J shocks, and intermediate cases has been given by Shull and Draine (1987).

This paper presents the results of a large number of numerical computations of the structure and emission from J shocks in molecular clouds. We have substantially enlarged and updated the physical processes described in Hollenbach and McKee (1979, hereafter HM79) for the numerical code. We highlight these changes in § II, which discusses the physical processes in fast interstellar J shocks. Section III presents the results of the computer runs for densities spanning the range 10^3 cm$^{-3} \leq n_0 \leq 10^6$ cm^{-3} (a future paper will address higher preshock densities in the context of the production of H_2O masers in the postshock gas; Elitzer, Hollenbach, and McKee 1989) and 30 km s$^{-1} \leq v_s \leq 150$ km s^{-1}. Section III also discusses these results and presents some analytic analysis which clarifies the important processes operating in the various shock waves. Section IV reviews applications made with preliminary versions of these results and outlines further potential applications. Section V summarizes the main conclusions. Appendix A describes the photoionizing precursor; Appendix B lists the chemical reactions in the code; Appendix C summarizes the atomic cooling.

II. PHYSICAL PROCESSES IN J SHOCKS

HM79 discuss the main physical processes incorporated into our J shock code. However, we have made numerous modifications to the treatment of the physical processes which we summarize below, along with some of the main features of the one-dimensional steady state code.

a) *Hydrodynamics*

The hydrodynamic equations for J shocks are relatively simple because most of the complexity in the shock structure is confined to the shock front, where the relative kinetic energy of the shocked and unshocked fluids is dissipated; in J shocks, the shock front has negligible thickness. The basic assumption we make is that the shock is *steady* (the generalization to weakly time dependent shocks is discussed by McKee *et al.* 1987). For steady shocks, the flow behind the shock front is governed by the Rankine-Hugoniot relations, as described by HM79. These three relations express the conservation of mass, momentum, and energy, and allow the determination of the density of hydrogen nuclei n, the flow velocity v, and the temperature T behind the shock front. Eliminating the velocity, HM79 obtained two differential equations for the density and temperature. We have found it more accurate to use the mass and momentum jump conditions and to solve the resulting cubic equation for the density explicitly. A single differential equation incorporating the energy jump condition is then integrated to find the temperature (HM79, eq. [2.29]) as a function of position behind the shock front (or, equivalently, as a function of time if we follow a parcel of gas flowing downstream from the shock front). The initial temperature just behind the shock front is given (HM79, eq. [2.30]) as

$$T_s = 3.18 \times 10^5 \frac{v_{s7}^2}{x_t} \text{ K} , \tag{2.1}$$

where x_t is the number of particles per hydrogen nucleus and $v_{s7} = v_s/100$ km s^{-1}. We assume a helium number abundance of 0.1 relative to hydrogen nuclei.

Magnetic fields in self-gravitating molecular clouds are expected to scale with density as $B_0 \propto n_0^{0.3-0.5}$, where n_0 (cm^{-3}) is the density of hydrogen nuclei in the cloud (Mouschovias 1976). Following HM79, we write

$$B_0 = b n_0^{0.5} \ \mu\text{G} \tag{2.2}$$

so that

$$b = v_A/(1.84 \text{ km s}^{-1}) , \tag{2.3}$$

where v_A is the Alfvén velocity. In the interstellar medium b is typically of order unity, although deviations of an order of magnitude in either direction can occur. In particular, the velocity dispersion observed in molecular clouds ($\sim$0.5–5 km s^{-1}) is currently thought to be about equal to the mean Alfvén velocity (e.g., Myers 1987), corresponding to $b \sim 0.3$–3. The magnetic field places an upper limit on the density behind the shock of n_m, where (HM79)

$$\frac{n_m}{n_0} = 76.7 \frac{v_{s7}}{b} . \tag{2.4}$$

The temperature at which the magnetic field becomes important—i.e., the temperature at which the density is about half its final value—is (HM79)

$$T_m = 2.2 \times 10^4 \frac{v_{s7} b}{x_t} \text{ K} . \tag{2.5}$$

Radiative shocks transform the relative kinetic energy of the shocked and unshocked gas into radiation. For a strong radiative shock, the shocked gas moves at almost the shock velocity. The radiated energy per hydrogen nucleus passing through the shock is then $0.5\mu_H v_s^2$, where μ_H is the mass per hydrogen nucleus. Half of this energy is initially directed upstream and half downstream, so that the upstream and downstream fluxes are each

$$F = 0.25 n_0 \mu_H v_s^3 = 5.8 \times 10^{-4} n_0 v_{s7}^3 \text{ ergs cm}^{-2} \text{ s}^{-1} . \tag{2.6}$$

In many cases a substantial fraction of this flux is in Lyα, and the resonance line scattering outside the cooling region can alter the ratio of the upstream to downstream Lyα flux (Neufeld and McKee 1988).

b) *Initial Conditions and Radiation Field*

Fast ($v_s \sim 100$ km s^{-1}) dissociative shocks, which are an important focus of this parameter study, produce a strong precursor ultraviolet radiation field and a complicated postshock structure and chemistry as the postshock temperature drops from $\gtrsim 10^5$ K to $\lesssim 100$ K (see Fig. 1). The preshock gas first experiences the radiation field from the approaching shock; our treatment of the chemical effects produced by the precursor field is based on the method of Shull and McKee (1979) and is described in Appendix A. Once shocked, the gas is dissociated and ionized in the immediate postshock environment and generally radiates copiously in the ultraviolet. Downstream, at a hydrogen column density $N_{cool} \sim 10^{17}$ cm^{-2} from the shock front, the gas cools to $\sim 10^4$ K and begins to recombine. An equilibrium is produced temporarily between recombination and photoionization by the UV photons produced upstream (the so-called "recombination plateau"). Once the ionizing photons are absorbed (at $N \sim 10^{18-19}$ cm^{-2}), the gas cools, recombines, and molecular chemistry commences. Cur-

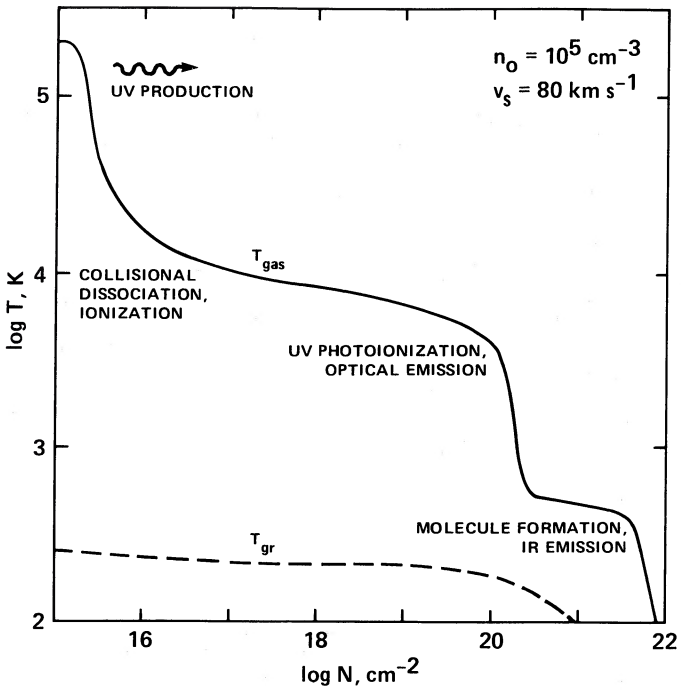

FIG. 1.—The postshock temperature structure of a fast molecular shock ($n_0 = 10^5$ cm^{-3}, $v_{s7} = 0.8$ shown here). Three regions are delineated: (1) the hot, $T \sim 10^5$ K, immediate postshock region, where gas is collisionally dissociated and ionized and UV photons are produced which affect both the preshock and postshock gas; (2) the "recombination plateau," where the Lyman continuum photons are absorbed, maintaining $T \sim 10^4$ K; and (3) the recombining and molecule-forming gas downstream, where chemical energy of H_2 formation can maintain a lower temperature plateau (*see text*). The column densities of the first two regions are nearly independent of n_0. Note that the grains are weakly coupled to the gas, so that $T_{gr} \ll T_{gas}$.

rently, it is not practical to construct and run a code which treats both the high temperature chemistry (i.e., the multiple ionization states of the species) and the production of UV radiation by metallic ions as well as the low-temperature molecular chemistry and the predominantly infrared radiation produced in the cooler ($T < 10^4$ K), neutral gas (however, MacLow and Shull 1986 and Shapiro and Kang 1987 calculate the chemistry and cooling behind fast, *nonmetallic*, pregalactic shocks where the relatively simple hydrogen and helium chemistry enable a complete calculation to be made up to shock velocities of $v_s \lesssim 400$ km s^{-1}). Several previous papers (see Pikel'ner 1954; Cox 1972; Dopita 1977; Shull and McKee 1979; Raymond 1979, Cox and Raymond 1985; Hartigan, Raymond, and Hartmann 1987; Seab, Shull, and McKee 1989) have treated the J shocks with emphasis on the structure of and the emission from the high-temperature gas. For J shock velocities greater than ~ 100 km s^{-1}, we have taken the physical parameters (e.g., the ionization fractions and UV fluxes) at $T = 10^4$ K from the shock code of Seab, Shull, and McKee (1989) as our initial conditions, and have continued the integration of the postshock parameters. We then follow the complex chemistry, heating, cooling, and radiative transfer which transpires in the cooling gas.

Because the code treats collisional ionization to singly ionized states and the production of UV radiation from the recombination of H^+ and He^+, we can follow the entire postshock structure (including the $T > 10^4$ K gas) as long as $v_s \lesssim 100$ km s^{-1}. This ensures that negligible UV flux and cooling is caused by higher ionization states of He and the heavier elements. Here, we use the Seab *et al.* results in order to predict, prior to the numerical integration of the shock variables, the precursor UV field and its chemical effect on the preshock gas (see Appendix A). A comparison of these results with the results obtained when we splice onto the Seab *et al.* results at $T = 10^4$ K has been made for 30 km s$^{-1} < v_s < 120$ km s^{-1} and 10^3 cm$^{-3} < n_0 < 10^7$ cm^{-3}. The predicted dominant emission line intensities produced below 10^4 K begin to differ by more than $\sim 50\%$ at $v_s = 100$ km s^{-1}, indicating the need to use the splice method for $v_s \gtrsim 100$ km s^{-1}.

Downstream from the $T = 10^4$ K point, the UV flux is attenuated by dust, atoms, and molecules as described in HM. The main sources of ultraviolet in this cooling gas is the recombination of H^+ and He^+ and the collisional excitation of the Lyα line of H and the Lyman and Werner bands of H_2. We discuss the treatment of atomic hydrogen in § II*d*(i). The recombination of He^+ is treated by considering rates which link 1^1S, 2^1S, 2^3S, and 2^1P, including collisions which link 2^3S to 2^1S and 2^1P (see, e.g., Osterbrock 1974) and 2^1S to 2^1P (Berrington *et al.* 1985). We ignore collisions which link 2^3S to 2^3P. The production of photons with $h\nu > 13.6$ eV is treated with the on-the-spot approximation, and the He I two-photon process is a substantial source of continuum far ultraviolet FUV (4 eV $< h\nu <$ 13.6 eV). The production of $h\nu < 10.2$ eV photons by the H I two-photon process ($2s$–$1s$) is also included, with proton collisions ($2s$–$2p$) suppressing the two-photon production at high densities [$n(H^+) \gtrsim 10^4$ cm^{-3}; see, e.g., Osterbrock 1974]. In addition, we have included the conversion of trapped Lyα photons to the two-photon decay, but find this to be of minor importance.

The gas-phase elemental abundances (ratio by number to hydrogen nuclei) used for the standard cases are based on the depletions tabulated by Harris, Gry, and Bromage (1984) and the solar abundances given by Allen (1983, p. 30): $x_{He} = 0.1$; $x_O = 5.4 \times 10^{-4}$; $x_C = 2.3 \times 10^{-4}$; $x_{Ne} = 1.0 \times 10^{-4}$; $x_N = 9.1 \times 10^{-5}$; $x_S = 1.0 \times 10^{-5}$; $x_{Si} = 3.6 \times 10^{-6}$; $x_{Fe} = 1.0 \times 10^{-6}$; $x_{Cl} = 1.4 \times 10^{-7}$; and $x_{Ni} = 7.6 \times 10^{-8}$. An "MRN" (Mathis, Rumpl, and Nordsieck 1977) size distribution of grains, with minimum radius $a_{min} = 100$ Å, maximum radius $a_{max} = 0.25$ μm, and average grain mass density $\rho_{gr} = 2$ g cm^{-3}, is assumed to be formed out of the gas-depleted material. (We also run a case with $a_{min} = 10$ Å). Assuming *total* elemental abundances that are solar, from which we subtract the above gas phase abundances, we calculate that $f_{gr} = 4.86 \times 10^{-3}$ is the fraction of mass in grains for the standard case. The fractional number f_i of strong hydrogen atom-binding sites on the grain surface is taken to be $f_i = 10^{-2}$ in the standard case; the rate coefficient for H_2 for formation at high grain temperatures depends on f_i (see HM79) and § II*c* below). The absorption coefficient of the grains is taken to be

$$Q = C_1 \left(\frac{a}{\lambda}\right) \lambda_{\mu m}^{-\beta}, \qquad (2.7)$$

where $\lambda_{\mu m}$ is the wavelength in microns and where $C_1 = 1$ and $\beta = 0$ in the standard case (see HM79).

c) Chemistry

We have considerably expanded the chemistry considered in HM79 to include 236 reactions involving 35 species. Appendix B lists the reactions. This enlarged chemical code was motivated in part by a desire to use identical chemistry in the J shock code as will be incorporated in the C shock code of

Chernoff *et al.* (1982) in order to obtain a self-consistent comparison of the intrinsic difference in the spectra of *C* shocks and *J* shocks. In addition, the possible observation of Si II(35 μm) shocked emission in Orion BN-KL (Haas, Hollenbach, and Erickson 1986) led us to include a small subset of silicon-based chemistry. As noted in HM79, the code also follows the ionization state of N, Ne, S, Fe, Ni, and Cl, assuming collisional ionization, photoionization and electron and grain recombination. The basic chemical processes were discussed in HM79; here we highlight some key processes and the important changes to the code.

i) *Formation and Destruction of* H_2

In fully dissociative shocks, it is the formation of H_2 which initiates the production of all other molecules and molecular ions in the postshock gas. The dominant process for forming molecular hydrogen is on the surfaces of the dust grains, although the H^- process has also been included. HM79 provide analytic expressions for each of these rate coefficients. The rate coefficient γ_{H_2} for H_2 formation on grains is defined so that the formation rate of H_2 is given by $\gamma_{H_2} n(H) n$, where $n(H)$ is the atomic hydrogen number density and n is the local hydrogen nuclei density. We have normalized the expression in HM79 so that $\gamma_{H_2} = 3 \times 10^{-17}$ cm^3 s^{-1} for cold gas and grains, assuming an MRN distribution with $a_{min} = 100$ Å. A typographical error appeared in the rate coefficient for the H^- process in HM79; equation (4.16) in HM79 should have the numerical coefficient 8.5×10^{-16} instead of 8.5×10^{-15}.

Photodissociation of H_2, including self-shielding, is treated as discussed in HM79. Collisional dissociation of H_2 occurs when a molecule in a vibrational state v is struck and makes a transition to the vibrational continuum. To calculate the dissociation rate, therefore, one must calculate the vibrational population of H_2. We have solved the matrix equations for the v population using the collisional rates of HM79, extrapolating these rates to higher v transitions by scaling $k(v, v-1) = vk(1, 0)$ (Sternberg and Dalgarno 1989). However, an improved fit to the collisional deexcitation rate coefficients of the $v = 2$-1 and $v = 1$-0 levels by H_2 collisions reveals that equation (6.29) in HM79 needs to be modified to:

$$\gamma_{21}^{H_2} = \gamma_{10}^{H_2} = 1.4 \times 10^{-12} T^{0.5} \exp\{-[18100/(T + 1200)]\} \text{ cm}^3 \text{ s}^{-1} . \quad (2.8)$$

The dissociation rates out of each v level are taken from the theoretical cross sections for H-H_2 collisions calculated by Blais and Truhler (1982), assuming a thermal distribution of *J* states within a given v state. We fitted a simple analytic expression to their numerical results, giving rate coefficients γ_{vd} for dissociation out of the v level,

$$\gamma_{vd} = 9 \times 10^{-11} \left(\frac{E_0}{\Delta E_{th}}\right) \left(\frac{T}{4500 \text{ K}}\right)^{0.5} \times \exp\left[-1.25 \left(\frac{\Delta E_{th}}{kT}\right)\right] \text{cm}^{-3} \text{ s}^{-1} , \quad (2.9)$$

where $E_0 = 4.48$ eV and ΔE_{th} is the dissociation threshold from v.

Using these rate coefficients for collisions with both H and H_2, we find that there is considerably less difference between the low-density rates (dissociation out of $v = 0$) and the high-density (LTE) rates than was found by Roberge and Dalgarno (1982), the $T \gtrsim 3000$ K results of Lepp and Shull (1983), or the He-H_2 results of Dove *et al.* (1987). Our results are most similar to the Dove *et al.* results, being nearly identical in the high-density limit and having very nearly the same low-density temperature dependence. Our low-density rates are quite similar to the low-density results for H-H_2 collisions given in Dove and Mandy (1986) and Mac Low and Shull (1986). We have also included electron-impact dissociation of H_2, using the experimental results of Corrigan (1965) for dissociation out of the $v = 0$ state.

ii) *The Oxygen Chemistry*

As discussed in HM79 and Hollenbach (1982), the essential oxygen chemistry involves a number of neutral-neutral reactions which are endothermic or which require activation energies to proceed (see Fig. 2). We use the rate coefficients of Wagner and Graff (1987) for many of the key rate coefficients, since they include important non–LTE effects. At low density, the molecules relax to the $v = 0$ state and the reaction rates differ from the LTE values. For a given reaction we use the rate coefficient

$$\gamma = \gamma_0 + \frac{(\gamma_{LTE} - \gamma_0)}{(1 + n_{cr}/n)} , \quad (2.10)$$

where n_{cr} is the critical density for vibrational excitation (see Appendix B), γ_0 is the $v = 0$ rate coefficient, and γ_{LTE} is the LTE rate coefficient. For reactions with OH and H_2O, the critical densities are large ($\gtrsim 10^{10}$ cm^{-3}) so that the $v = 0$ rates apply. However, for the reaction

$$H_2 + O \rightarrow OH + H$$

which initiates the oxygen chemistry, $n_{cr} \sim 10^4$ cm^{-3} for collisions with H atoms at $T \sim 10^3$ K, and equation (2.10) must be applied to the postshock gas (see Appendix B).

iii) *CO Dissociation*

Although CO has nearly 3 times the binding energy of H_2, we find that CO dissociation often follows H_2 dissociation. Part of the explanation of this surprising phenomenon can be seen by inspecting Figure 2. Once H_2 has completely collisionally dissociated, CO can be *chemically* dissociated at these same gas temperatures ($\gtrsim 3000$ K) by the endothermic reaction $H + CO \rightarrow C + OH$. Moreover, the photodissociation of CO proceeds by the line absorption of photons in the range 11 eV $< h\nu <$ 13.6 eV, and CO shields itself much like H_2 (see, e.g., van Dishoeck and Black 1987). In fact, the Lyman and Werner bands of H_2 overlap, to some extent, the photodestructive lines of CO so that once H_2 self-shielding is significant, the shielding of CO is enhanced (van Dishoeck and Black 1988). We have treated the CO self-shielding in a simplified manner, ignoring possible overlaps with H_2 lines, treating only photodissociation by the FUV continuum (mostly 2

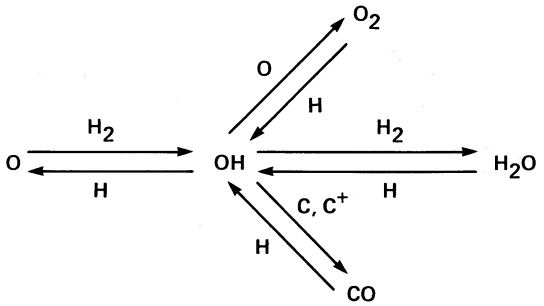

FIG. 2.—Fast neutral reactions with moderate activation energies or endothermicities dominate the oxygen chemistry in warm $T \gtrsim 300$ K postshock gas.

photon He decays), and approximating the complicated radiative transfer by a formula analogous to that for H_2 (see HM79). The photodissociation rate R_{CO} per molecule is then given by

$$R_{CO} = R_0 \left\{ \frac{\beta_{CO}}{[\beta_{CO}^2 + N(CO)]^{0.5}} \right\} \text{ s}^{-1}, \quad (2.11)$$

where R_0 is the unshielded rate (7×10^{-11} s^{-1} in the ambient interstellar field, see van Dishoeck 1987), $N(CO)$ is the column density of CO, and we estimate $\beta_{CO} = 3 \times 10^6$ cm^{-1} (this estimate has been recently confirmed by a more detailed treatment by Neufeld 1987).

iv) *Non-Maxwellian Electron Distribution*

At high temperatures $T \gtrsim 10^2$ K but low electron abundances $x_e \lesssim 10^{-3}$, such as occurs in the dissociating regions behind these J shocks, the high-energy tail of the electron distribution can be depleted relative to a Maxwellian distribution. In the case of J shocks, this depletion is caused mainly by the inelastic collisions which electrons with energies greater than ~ 8 eV experience in dissociating H_2. This depletion could, in principle, significantly lower the rates of all endothermic electronic reactions which require energies in excess of 8 eV (e.g., ionization of H or H_2 by electronic collisions). We have generalized the method of Shoub (1977) to treat the effects of non-Maxwellian distributions of electrons; however, we have found the effects to be of minor significance to the J shock structure and spectra, with the integrated intensities of the emission lines changing by less than 30%.

d) Cooling

i) *Atomic Hydrogen*

As discussed in McKee and Hollenbach (1987), much of the emission measure and, therefore, recombination radiation from a shock occurs at $T < 10^4$ K. In addition, most of the collisional excitation of H occurs in this region, where the H^+ recombines. The Balmer, Paschen, and Brackett lines from fast dissociative shocks are generally quite intense, and their intensities are diagnostic of the shock velocity (since v_s determines the level of ionization). Therefore, we have constructed a seven-level (n) model for H, assuming l mixing, and including collisional excitation, collisional ionization, photoionization, and radiative recombination. We have used recombination rates from Brocklehurst (1971) and Giles (1977) and collision rates from Giovanardi, Natta, and Palli (1987). We make the on-the-spot approximation for Lyman transitions to the ground, with the exception of Lyα, with the result that every recombination or collisional excitation leads to either a Lyα photon or to the hydrogen two-photon decay from the $2s$ state (collisional deexcitation to the ground state is negligible because of the large n_{cr}). The Lyα photon, however, is trapped for many scatterings because of the large optical depth in the line, before it is finally absorbed in the postshock gas and dust.

ii) *Cooling by Other Atoms and Ions*

We have included the lowest lying permitted (resonance) transitions of Fe I and Fe II; low-lying metastable transitions of C I, C II, N I, N II, O I, O II, Si I, Si II, S I, S II, Cl II, Fe I, Fe II, Ni I, and Ni II; and the fine-structure transitions of the ground electronic state levels of C I, C II, O I, Ne II, Si I, Si II, S I, Cl I, Cl II, Fe I, Fe II, Ni II. Appendix C lists the transitions and the relevant atomic parameters including the collisional rate coefficients assumed for collisions with H, H_2, and electrons. As coolants, the important transitions include the metastable lines of O I λ6300 and C I λ9849 for $T \sim 5000$ K and the fine-structure lines O I(63 μm), Si II(35 μm), and C II(158 μm) for $T < 5000$ K and predominantly atomic gas. The radiative transfer in the lines is treated by the escape probability formalism as described in HM.

iii) H_2 *Cooling*

The rotational population of the $v = 0$ state is calculated by solving the matrix equation for statistical equilibrium including collisions with electrons, H atoms, and H_2 molecules. Electronic rates are taken from Draine, Roberge, and Dalgarno (1983, hereafter DRD). H atom rates are taken from DRD but corrected according to Flower, Pineau des Fôrets, and Hartquist (1986). We include only those collisions which cause transitions of $\Delta J = \pm 2$. The rate coefficient for collisional deexcitations from J is taken as

$$\gamma_{\Delta J} = 4.6 \times 10^{-12}(2J - 3)T^{0.5}(1 + x)^{0.5} \times \exp\left\{ -\left[\frac{10.0B(2J-1)}{kT + BJ(J+1)} \right] + 0.1187(4J - 2) \right\} \text{ cm}^3 \text{ s}^{-1} \quad (2.12)$$

where $x = 2B(2J - 1)/kT$ and $B/k = 85.25$ K. The rate coefficients for H_2-H_2 collisions are taken from HM79 except for those transitions with $J > 9$ or $\Delta J > 2$, where rates from DRD are used.

We make the simplifying approximation that the relative population of the J states in the $v = 0$ level also applies to the vibrational levels. Although this may appear somewhat crude, the individual collision rates between v, J levels necessary for a more accurate calculation are not available. Shull and Hollenbach (1978) discuss the complexities and uncertainties in the individual rates. The solution to the vibrational levels has been discussed in § I*c*(ii).

We treat the modification of these populations by UV pumping (Black and Dalgarno 1976; van Dishoeck and Black 1987) and H_2 formation pumping (Bieniek and Dalgarno 1979; Black, Porter, and Dalgarno 1981) in an approximate way as well. At low densities, $n < n_{cr}$, we add the pump line emission to the collisionally induced emission in calculating the total line emission; however, the cooling results solely from the collisional excitation. At high density, $n > n_{cr}$, the pumped rovibrational energy is collisionally deexcited and transferred to heat (see § II*e*).

iv) CO *Cooling*

The CO rotational cooling is derived from McKee *et al.* (1982), who adopt the formalism of HM79 to new cross sections for collisional excitation of CO. Viscuso and Chernoff (1988) show that the new results of Schinke *et al.* (1985) for CO collisional rate coefficients do not appreciably modify these results. The vibrational rate coefficients for transitions to the $v = 1$ state of CO were taken from Millikan and White (1963), Thompson (1973), and von Rosenberg, Taylor, and Teare (1971), and are given by

$$\gamma_{CO}^{H} = 3.0 \times 10^{-12} T^{0.5} \exp\left[-\left(\frac{2000}{T} \right)^{3.43} \right] \times \exp\left(\frac{-3080}{T} \right) \text{ cm}^3 \text{ s}^{-1}, \quad (2.13a)$$

$$\gamma_{CO}^{H_2} = 4.3 \times 10^{-14} T \exp\left[-\left(\frac{3.14 \times 10^5}{T}\right)^{0.333}\right] \times \exp\left(\frac{-3080}{T}\right) \text{cm}^3 \text{ s}^{-1}, \quad (2.13b)$$

where H and H_2 denote collisions with H atoms and H_2 molecules, respectively.

v) H_2O *and* OH *Cooling*

We have adopted the HM79 formalism to detailed numerical results for H_2O cooling derived from new H_2-H_2O rates supplied by Sheldon Green (1987, private communication). In order to match these results, the total rotational deexcitation cross section for H_2O, as defined in HM79, is $\sigma = 1.5 \times 10^{-16}$ cm^{-2} and the multiplicity factor $\eta_T = 175 T_3^{1.5}$, where $T_3 = T/1000$ K. Furthermore, we use results on OH rate coefficients by Dewangen and Flower (1982) and Schinke and Andreson (1984) to estimate that $\sigma = 2 \times 10^{-16}$ cm^{-2} for OH. The vibrational excitation rate coefficients to the lowest v state of H_2O are taken from the general formula of Millikan and White (1963):

$$\gamma_{H_2O}^{H} = 2.3 \times 10^{-14} T \exp(-34.5/T^{0.333}) \times \exp(-2325/T) \text{ cm}^3 \text{ s}^{-1}, \quad (2.14a)$$

$$\gamma_{H_2O}^{H} = 3.2 \times 10^{-14} T \exp(-47.5/T^{0.333}) \times \exp(-2325/T) \text{ cm}^3 \text{ s}^{-1}. \quad (2.14b)$$

vi) *Grain Cooling*

The cooling of the gas by the cooler dust grains is important at high postshock densities $n \gtrsim 10^8$ cm^{-3}, and at somewhat lower densities when H_2O and OH contain only a fraction of the cosmic abundance of O. The cooling rate per unit volume is given (HM79)

$$L_{gr} = 1.2 \times 10^{-31} n^2 \left(\frac{T}{1000 \text{ K}}\right)^{1/2} \left(\frac{100 \text{ Å}}{a_{min}}\right)^{1/2} \times [1 - 0.8 \exp(-75/T)](T - T_{gr}) \text{ ergs cm}^{-3} \text{ s}^{-1}, \quad (2.15)$$

where n is in cm^{-3} and T_{gr} is an effective grain temperature, averaged over the assumed MRN size distribution. Since the gas generally collides with the smaller grains, we take T_{gr} to be the temperature of grains of radius a_{min}.

e) Heating

i) *Grain Photoelectric Heating*

We use the results of deJong (1980) to calculate the heating by the photoelectric ejection of electrons from grains by FUV photons. We ignore grain photoelectric heating by Lyman continuum photons, since these are preferentially absorbed by the neutral gas.

ii) *Gas Photoelectric Heating*

The photoionization of H, He, and C by ultraviolet photons produced in the shock can be a significant heating source. Like the grain photoelectric heating, this process involves energetic electrons which are ejected into the gas where their excess energy is thermalized by collisions. As discussed in § II*b*, the H photoionization heating causes a temperature plateau at $T \sim 5000$–10^4 K where the recombining postshock gas absorbs Lyman continuum photons from the hot gas immediately behind the shock front. The photoionization rates are given in HM79; here we note a more subtle process. The recombination of He^+, as discussed in § II*b*, involves the production of H ionizing photons in the following transitions: 2^3S–1^1S (19.8 eV), 2^1P–1^1S 21.3 eV), and 2^1S–1^1S (two photon with 13.6 eV < $h\nu$ < 20.7 eV 56% of the time). These Lyman continuum photons are treated with an on-the-spot approximation as being instantly absorbed by hydrogen atoms and H_2 molecules.

iii) *Cosmic Rays*

We use the cosmic-ray ionization rates given in Appendix B for H, H_2, and He and assume that 3.4 eV of heat is deposited in the gas per ionization (Spitzer and Scott 1969). Cosmic-ray heating is negligible in the cooling ($T \gtrsim 100$ K) postshock gas, but can affect the cooler gas downstream.

iv) *Heating by* H_2 *UV Pumping, Photodissociation, and Formation*

Line absorption of FUV photons in the range 11 eV < $h\nu$ < 13.6 eV by H_2 electronically excites the H_2. Subsequent radiative decay leads to the vibrational continuum of the ground electronic state (i.e., dissociation) 10% of the time with ~0.5 eV of excess kinetic energy deposited as heat. The remaining 90% of the decays are to the bound vibrational states of the ground electronic state. In addition, the H_2 molecule forms in excited vibrational and rotational states. At low densities, $n < n_{cr}$, where n_{cr} is the critical density for collisional deexcitation of the vibrational levels, the H_2 molecule radiatively decays to the ground state. However, for $n > n_{cr}$ the FUV or formation-pumped H_2 molecule is collisionally deexcited and the vibrational energy is delivered as heat (see HM79 or Hollenbach 1988 for more discussion). At $T = 300$ K, $n_{cr}(H) \sim 10^5$ cm^{-3} for collisions with H atoms and $n_{cr}(H_2) = 7 \times 10^9$ cm^{-3} for collisions with H_2 molecules. Thus, H atoms are especially effective in transferring H_2 vibrational energy into heat. Behind J shocks which dissociate H_2 molecules, the heating due to H_2 (re)formation at high densities is especially important and can lead to enhanced column densities of relatively warm ($T \sim 100$–500 K) postshock gas of relatively high molecular abundance. This is discussed in more detail in § III*b* below.

III. RESULTS AND DISCUSSION

a) Parameter Study and the Standard Shock

We have computed the shock structure and the emergent line intensities from shock waves with preshock densities 10^3 cm$^{-3} \leq n_0 \leq 10^6$ cm^{-3}, velocities 30 km s$^{-1} \leq v_s \leq 150$ km s^{-1}, preshock magnetic fields set by $b = 0.5$ (see eq. [2.2]), gas phase abundances listed in § II*b*, and with the physical and chemical processes described in § II. The $v_s = 30$ and 40 km s^{-1} runs are to be viewed with some caution, since they may in reality be *C* shocks, as discussed in DRD and Chernoff *et al.* (1982). We take for our "standard" shock the parameters $n_0 = 10^5$ cm^{-3}, $v_s = 80$ km s^{-1}, and $b = 0.5$. This standard shock lies in the middle of the parameter space studied and its structure nicely exemplifies all the main features of the parameter study. In addition, it may be representative of a "wind shock" which has been proposed to explain O I(63 μm), Si II(35 μm), and H51α observations in Orion BN-KL (Chernoff *et al.* 1982; Werner *et al.* 1984; Haas *et al.* 1986; McKee and Hollenbach 1987).

We have also tested the sensitivity of the integrated intensities in the standard shock to variations in parameters other than n_0 and v_s. The parameters varied include the magnetic field, the radiation field and radiative transfer in the shock,

certain key chemical reaction rates, the gas-phase elemental abundances, the grain size distribution, and the formation heating by H_2.

b) Shock Structure

i) *Chemistry*

The preshock gas is largely neutral and molecular in the standard shock, although the precursor radiation field does dissociate $\sim 10\%$ of the preshock H_2 molecules and ionize $\sim 1\%$ of the neutral hydrogen (see Fig. 11, Appendix A). Directly behind the shock front, the gas temperature is $\sim 2 \times 10^5$ K and, as the gas cools, collisional dissociation, and ionization rapidly destroy the molecules and increase the ionization fraction to peak values of $x(H^+) \sim x(e) \sim 0.6$ at $T \sim 10^4$ K. Photoionization by UV photons produced in the hot shocked gas maintains this ionization fraction and temperature (the "recombination plateau") to $N \sim 10^{19}$ cm^{-2}, where the H ionizing photons are fully absorbed and the gas rapidly recombines (see Fig. 1).

As the gas recombines and the temperature drops, the reformation of the dissociated molecules commences. Figure 3 shows the temperature and chemical structure as a function of the hydrogen nucleus column density $N \geq 10^{19}$ cm^{-2} behind the standard shock. Note that the abundances of H_2 molecules, and H^+ ions are divided by 10^3 in order to place them in the range of the other species. With the exception of H_2, the molecular abundances are largely in statistical equilibrium since

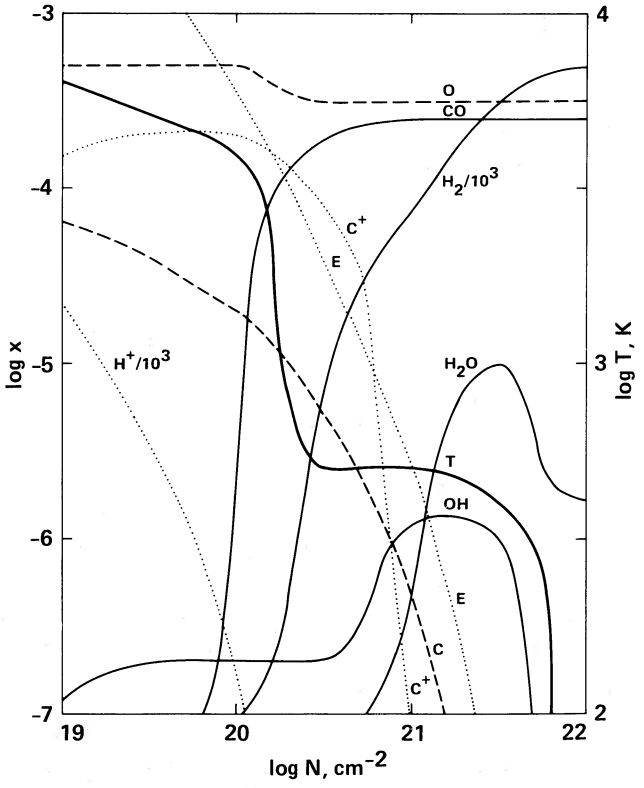

FIG. 3.—The temperature and chemical structure of the "chemical region," $N \gtrsim 10^{19}$ cm^{-2} and $T \lesssim 5000$ K, of the standard shock ($n_0 = 10^5$ cm^{-3}, $v_s = 80$ km s^{-1}, and $b = 0.5$). The fractional number abundances x of the species relative to hydrogen are plotted; note that we plot $x/10^3$ for H^+ and H_2. The temperature plateau at $T \sim 400$–500 K is caused by the heat of formation of H_2 (*see text*).

the chemical time scales $t_{chem} \lesssim [\gamma_{chem} \times (10^{-4} n)]^{-1} \sim 10^{12} b/(n_0 v_{s7})$ s are shorter than the cooling time scales $t_c \sim N_c/(n_0 v_s) \sim 10^{14} N_{c21}/(n_0 v_{s7})$ s, where $N_c = 10^{21} N_{c21}$ cm^{-2} is the cooling column density and $\gamma_{chem} \sim 10^{-10}$ cm^3 s^{-1} is a typical gas phase chemical rate coefficient. Thus, to first order, *the chemistry follows the formation of* H_2.

The formation of H_2 at high ionization levels [$x(e) \gtrsim 10^{-3}$] and gas temperatures ($T \gtrsim 3000$ K) proceeds by the H^- process, which produces $x(H_2) \sim 10^{-4}$–10^{-3}. As the gas recombines and cools further, the formation of H_2 proceeds slowly on grain surfaces, with an effective recombination rate coefficient of $\gamma_{H_2} \sim 10^{-17}$ cm^3 s^{-1} (see § II*b*). In contrast to the trace molecules, H_2 is not in statistical equilibrium but forms as $\dot{x}(H_2) \sim \gamma_{H_2} n(H)$. The postshock density n is very nearly constant in the H_2 formation region because the pressure is magnetically dominated there (see eq. [2.5]); therefore, the above expression for $\dot{x}(H_2)$ can readily be integrated to give

$$x(H_2) = \frac{1}{2}\left[1 - \exp\left(-0.153\gamma_{-17}\frac{N_{21}}{b}\right)\right] \sim 8 \times 10^{-2}\gamma_{-17}\frac{N_{21}}{b}, \quad (3.1)$$

where $N_{21} = N/10^{21}$ cm^{-2}, $\gamma_{-17} = \gamma_{H_2}/10^{-17}$ cm^3 s^{-1}, and the approximation applies to $x(H_2) \ll 1$. The column density required to convert half of the hydrogen to H_2 is

$$N_{1/2} = 4.5 \times 10^{21}\frac{b}{\gamma_{-17}}\ \text{cm}^{-2}. \quad (3.2)$$

The rate coefficient γ_{-17} is of order unity and relatively insensitive to gas temperature T and grain temperature T_{gr} for $T \lesssim 10^3$ K and $T_{gr} \lesssim 100$ K. However, the expression of HM79 for γ_{-17} drops significantly for $T_{gr} \gtrsim 100$ K, because of the rapid evaporation of H atoms from grain surfaces. We find that grain temperatures exceed 100 K in the molecule-forming regions ($N > 10^{20}$ cm^{-2}) when $n_0 v_{s7}^3 \gtrsim 10^6$ cm^{-3}, and that the expression

$$N_{1/2} = 4.0 \times 10^{21} b\left\{1 + 100\exp\left[-\frac{58}{(n_0 v_{s7}^2)^{0.2}}\right]\right\}\ \text{cm}^{-2} \quad (3.3)$$

is good to 25% for the entire space studied. This corresponds to a distance behind the shock given by $z_{1/2} = N_{1/2}/n_m$ with n_m given by equation (2.4)

$$z_{1/2} = 5.2 \times 10^{14} b^2 (n_{05} v_{s7})^{-1} \times \left\{1 + 100\exp\left[-\frac{58}{(n_0 v_{s7}^3)^{0.2}}\right]\right\}\ \text{cm}, \quad (3.4)$$

where $n_{05} = n_0/10^5$ cm^{-3}.

Carbon monoxide is the first molecule to completely reform. The formation of CO is initiated by the fast (at $T \gtrsim 300$ K) reaction $H_2 + O \rightarrow OH + H$, with the resultant OH reacting with C^+ and C to ultimately form CO. CO destruction is by FUV photodissociation, by endothermic reaction with H, or by reaction with He^+. Once CO has self-shielded, these reactions are sufficiently slow that all the carbon can be channelled into CO even when the H_2 abundance is low.

The abundances of H_2O, OH, and O_2 all rise to appreciable values ($\sim 10^{-5.5}$–$10^{-4.5}$) in the $T \lesssim 300$ K post(standard)shock gas because of the relatively rapid neutral-neutral chemistry shown in Figure 2, with some suppression of their abundances by FUV photodissociation.

However, most of the oxygen not tied up in CO remains atomic for $T \gtrsim 100$ K in the standard shock because in this case the H_2O formation freezes out before the FUV flux is fully attenuated.

The gas phase silicon is mainly Si^+ to $N \lesssim 10^{21}$ cm^{-2} ($T \gtrsim 500$ K), whereafter the silicon is predominantly in SiO. We therefore note that a more complete chemical code may be necessary for S, Cl, Fe, and Ni, whose "molecularization" we presently ignore. For example, a significant fraction of the sulfur may be channelled into SO and SO_2, and chlorine may become HCl.

ii) *Heating, Cooling, and Temperature Structure*

Directly behind the shock front, collisional dissociation, ionization, and excitation of Lyα dominate the cooling to $T \sim 10^4$ K. Heating by the photoionization of H maintains $T \sim 10^4$ K to $N \sim 10^{19}$ cm^{-2}. Figure 4 plots the temperature and dominant coolants of the standard shock for $N \geq 10^{19}$ cm^{-2}. In the temperature range 10^4 K $\gtrsim T \gtrsim 5000$ K, metastable cooling becomes dominant, with O I λ6300, C I λ9849, and C II λ2326 the prime coolants. Figure 4 shows O I λ6300 as an example. From 5000 K to 100 K the cooling is dominated by O I(63 μm) emission for low-density gas ($n_0 \lesssim 10^5$ cm^{-3}), by CO at intermediate density ($n_0 \sim 10^5$ cm^{-3}), and by grains and H_2O for high-density gas ($n_0 \gtrsim 10^5$ cm^{-3}).

A second temperature plateau occurs at $T \sim 400$–500 K for $n_0 \gtrsim 10^5$ cm^{-3}. This plateau is caused by the gas heating due to the formation of H_2 in excited vibrational states followed by the collisional deexcitation by atomic hydrogen of this excitation energy (see § IIe). The plateau disappears for $n_0 \lesssim 10^5$ cm^{-3} because the postshock densities are insufficient to collisionally deexcite the newly formed H_2. This plateau extends to $\sim 2N_{1/2}$, where the formation of H_2 is essentially complete and the heating process is terminated. The temperature of this plateau can analytically be approximated by equating the H_2 formation heating to the grain cooling:

$$T_{1/2} \sim 10^3 (f_a a_{-6}^{1/2})^{0.43} \text{ K}, \quad (n_0 \gtrsim 10^5 \text{ cm}^{-3}) \tag{3.5}$$

where f_a (≤ 1) is the efficiency factor in H_2 formation which accounts for H atom evaporation from grains (see HM79), $a_{-6} = a_{\min}/(10^{-6}$ cm) in the MRN grain size distribution, and $n_0 \gtrsim 10^5$ cm^{-3} so that grain cooling is significant. Equation (3.5) overestimates $T_{1/2}$ by a factor ~ 2 at $n_0 = 10^5$ cm^{-3} because it underestimates the cooling by neglecting other coolants, such as H_2O, OH, CO, and O I(63 μm), each of which is comparable to grains; at $n_0 = 10^6$ cm^{-3}, the grain cooling is about half the total, but f_a is ~ 0.4 so that $T_{1/2} \sim 500$ K. Equation (3.5) shows, however, the relative insensitivity of $T_{1/2}$ to n_0 in this range, as well as to v_s in the range 30 km s$^{-1} < v_s < 150$ km s^{-1}. For $n_0 \lesssim 10^5$ cm^{-3}, O I(63 μm) dominates the cooling and the postshock temperature drops to $T \lesssim 200$ K, where the critical density for collisional deexcitation of H_2 by H atoms exceeds the postshock density. Under these conditions, the H_2 formation heating is extinguished, as most of the H_2 formation energy is radiated away in the quadrupole vibrational transitions of H_2.

It is convenient, for the purposes of approximating shock structure and estimating line intensities, to give the column density to $T = 10^4$ K, $N_{10^4\,\mathrm{K}}$, and the column density to 100 K, $N_{100\,\mathrm{K}}$, as functions of n_0 and v_s. We have made an analytic fit to $N_{10^4\,\mathrm{K}}$ obtained in our numerical results for 10^3 cm$^{-3} \leq n_0 \leq 10^6$ cm^{-3} and $0.3 \leq v_{s7} \leq 0.8$, where the entire shock is calculated:

$$N_{10^4\,\mathrm{K}} = 3 \times 10^{16} v_{s7}^{-2} \exp\left(\frac{0.4}{v_{s7}}\right)^4 \text{ cm}^{-2}, \quad (0.3 \leq v_{s7} \leq 0.8). \tag{3.6}$$

This expression is good to $\pm 40\%$ if we ignore the $n_0 = 10^3$ cm^{-3}, $v_{s7} = 0.3$ run which did not completely dissociate the molecules and therefore led to a very small value, $N_{10^4\,\mathrm{K}} = 6.5 \times 10^{16}$ cm^{-2}. The distance behind the shock front, $z_{10^4\,\mathrm{K}} = N_{10^4\,\mathrm{K}}/(0.25 n_m)$, with n_m given by equation (2.4). The factor 0.25 arises because the gas density at $T = 10^4$ K is $\sim 0.25 n_m$ for $b = 0.5$. Utilizing equation (2.4), we anticipate that the b-dependence of this factor is $\sim (1 + 1.5/b)^{-1}$. The column $N_{100\,\mathrm{K}}$ can analytically be fitted over the entire velocity range by two expressions, representing the low-density regime with no H_2 formation plateau and the high-density regime with the H_2 formation plateau:

$$N_{100\,\mathrm{K}} = 1 \times 10^{21} n_{05}^{0.5} v_{s7} \text{ cm}^{-2} \quad (0.01 \lesssim n_{05} \lesssim 0.3, b = 0.5), \tag{3.7}$$

$$N_{100\,\mathrm{K}} = 3 N_{1/2} \quad (0.3 \lesssim n_{05} \lesssim 10). \tag{3.8}$$

The first expression is accurate to within a factor 1.5 for $0.4 \leq v_{s7} \leq 1.5$, and the second is accurate to within a factor 1.3 for $0.3 \leq v_{s7} \leq 1.5$. Similarly accurate expressions for $z_{100\,\mathrm{K}}$ can be obtained by setting $z_{100\,\mathrm{K}} = N_{100\,\mathrm{K}}/n_m$.

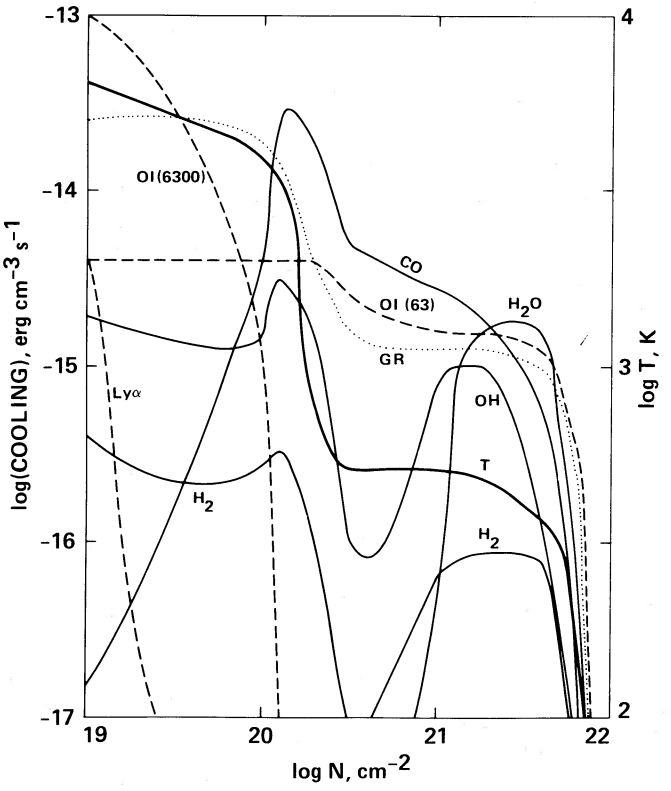

FIG. 4.—The temperature and cooling profiles behind the standard shock. GR denotes the gas cooling by collisions with the cooler grains. The molecular cooling includes vibrational and rotational contributions.

c) Variation of Shock Spectra with n_0 and v_s

In the following discussion we will present figures which give the integrated intensities of the various transitions excited in

the shocked gas. Because the line photons may be subject to absorption and scattering, we calculate the flux F_l emerging from the shock front using the escape probability formalism described in HM79. In the simplest case in which neither absorption nor scattering is important (e.g., the rovibrational lines of H_2), the specific intensity in the direction of the shock normal is

$$I_l' = \frac{F_l}{2\pi}, \tag{3.9}$$

and it is this quantity we plot in the figures. In this case, I_l' is simply $\int j_l dz$, where j_l is the line emissivity in units of ergs cm^{-3} s^{-1} sr^{-1}, and the specific intensity in any other direction is $I_l(\mu) = I_l'/\mu$, where μ is the direction cosine of the ray with respect to the shock normal. The singularity in $I_l(\mu)$ at $\mu = 0$ is not present in reality, both because of the finite lateral extent of the shock and because of the finite amount of absorption present in any interstellar plasma (I_l reaches the blackbody limit; see Shull and McKee 1979).

Some lines, such as the resonance lines of atoms and ions and some of the CO lines, are subject to resonance scattering, but not absorption, in the region in which the lines are produced. Radiative transfer effects leave the emergent flux of these lines unaltered, but they do alter the angular distribution of the emitted radiation (Raymond *et al.* 1980). In the limit of large scattering optical depth, the emergent radiation is isotropic and the specific intensity is

$$I_l(\mu) = \frac{F_l}{\pi} = 2I_l' . \tag{3.10}$$

If shocked regions are observed with sufficient angular resolution, then edge-on shocks ($\mu \ll 1$) will appear brightest, and for such shocks the lines which are opaque to scattering will be suppressed in intensity relative to the optically thin lines (Raymond *et al.* 1980).

We generally assume that the upstream and downstream fluxes for a line are equal, but this will not be true if scattering is important outside the region where the line is emitted. This is mainly important for the resonance scattering of Lyα. If the H I column behind the shock substantially exceeds that ahead of the shock because of H_2 dissociation in the shock, then the upstream Lyα flux could be twice that given in equation (3.10), since the shocked H I acts like a mirror. If the H I column ahead of the shock is also large, then the Lyα line profile can be altered as well as the specific intensity (Neufeld and McKee 1988).

i) H_2 *Spectra*

The H_2 rovibrational infrared transitions are optically thin because they are highly forbidden quadrupole transitions with small absorption cross sections. Two major components contribute to the H_2 spectra: (1) the formation pumping of H_2, and (2) collisional excitation in the H_2 formation plateau for $n_0 \gtrsim 10^5$ cm^{-3}. The latter contribution, coming from gas at $T \sim 500$ K, is only significant for the low-lying (0–0)S(0–5) pure rotational lines. Figure 5 presents the results for the density range 10^3 $cm^{-3} \leq n_0 \leq 10^6$ cm^{-3}. We have only calculated up to $S(11)$ because the formation pumping scheme is inadequate for $J > 13$. The $n_0 = 10^3$ cm^{-3} case is nearly pure formation pumping, except for the upturn at low velocities caused by collisional excitation in incompletely dissociated H_2. These nondissociative molecular shocks are quite likely C shocks, and not J shocks as we have assumed, so that this upturn is not likely to be significant in reality. The $n_0 = 10^4$ cm^{-3} case shows pure formation pumping at $v_{s7} \leq 1$, with a thermal contribution arising at $v_{s7} = 1.5$ because of the onset of the H_2 formation plateau. The $n_0 = 10^5$, 10^6 cm^{-3} cases show the two components clearly: as J increases, we see two peaks in the intensities of the $S(J)$ transitions, the first at $\sim S(3)$ and the second at $\sim S(11)$. The first peak is the thermal contribution from the H_2 formation plateau; the second comes from the formation pumping. Note that (1–0)S(1)/(2–1)S(1) ratios are of order 2–3, typical of "pump" ratios (although this is *shock* emission). Note also that the (1–0)S(1) intensity is always $\ll 10^{-1}$ ergs cm^{-2} s^{-1} sr^{-1}, the observed (extinction corrected) intensity in BN-KL; this result forces one to adopt nondissociative C shock models for the bulk of the BN-KL (1–0)S(1) emission. The formation-pumped line intensities increase with n_0 for $n_0 \lesssim 10^5$ cm^{-3}, but saturate for higher preshock densities. Although the flux of forming molecules is proportional to n_0, the collisional deexcitation at high n_0 of the pumped levels offsets the linear n_0 dependence of the pumped flux.

ii) CO *Spectra*

Figure 6 presents the CO spectra for shocks of preshock density 10^3 $cm^{-3} \leq n_0 \leq 10^6$ cm^{-3}. The CO intensities are very low ($\lesssim 10^{-5}$ ergs cm^{-2} s^{-1} sr^{-1}) in the $n_0 = 10^3$ cm^{-3} case due to the combined effect of low CO column densities at $T > 100$ K and low postshock densities which fail to appreciably excite the higher J levels. The $n_0 = 10^4$ cm^{-3} intensities are also lowered by these effects. The $n_0 = 10^4$ cm^{-3}, $v_s = 30$ km s^{-1} case is anomalous because of incomplete destruction of CO in this run. The $n_0 = 10^{5-6}$ cm^{-3} cases are relatively similar in shape and absolute intensity. The low J ($J \lesssim 15$–20) emission arises from the moderately optically thick H_2 formation plateau, which has relatively constant column density $N_{CO} \sim 3 \times 10^{-4} N_{1/2} \sim 10^{18} b$ cm^{-2} and temperature $T_{1/2} \sim 400$ K as a function of n_0 and v_s for $n_0 \gtrsim 10^5$ cm^{-3}. The high J emission is more dependent on velocity and declines with J with a curvature unlike either optically thick or thin emission from an *isothermal* slab. This emission is largely optically thin emission from postshock gas cooling from 3000 K to 500 K. The J dependence is somewhat steeper and the overall intensities somewhat lower for $n_0 \lesssim 10^5$ cm^{-3} because of the drop of high J populations from LTE. The overall similar intensity levels for $n_0 \gtrsim 10^5$ cm^{-3} attests to the relatively constant column of the $\sim 10^3$ K cooling gas in these cases; the relatively weak v_s dependence is caused by the somewhat greater columns of the higher T gas at higher velocities. We conclude that CO emission will not be a good diagnostic of v_s and n_0 unless very high quality spectra of the detailed shape of the J dependence around J_{max}, the J of maximum intensity, are obtained.

iii) *Fine-Structure Spectra*

Figure 7 shows the fine-structure emission for 10^3 $cm^{-3} \leq n_0 \leq 10^6$ cm^{-3}. It is immediately evident that these dissociative shocks produce a plethora of intense atomic and ionic fine-structure lines. Most of the fine-structure emission from these shock waves is optically thin, as can be seen by comparing N_τ (Appendix C) with $N_{100\,K}$. Notable exceptions are O I(63 μm, 145 μm), Si I(68 μm, 130 μm), and Fe I(24 μm, 34 μm) for $n_0 \gtrsim 10^5$ cm^{-3}, where the H_2 formation plateau produces a large column density, $N \sim 10^{22}$ cm^{-2}, of predominantly neutral gas. We discuss five major features of the fine-structure spectra.

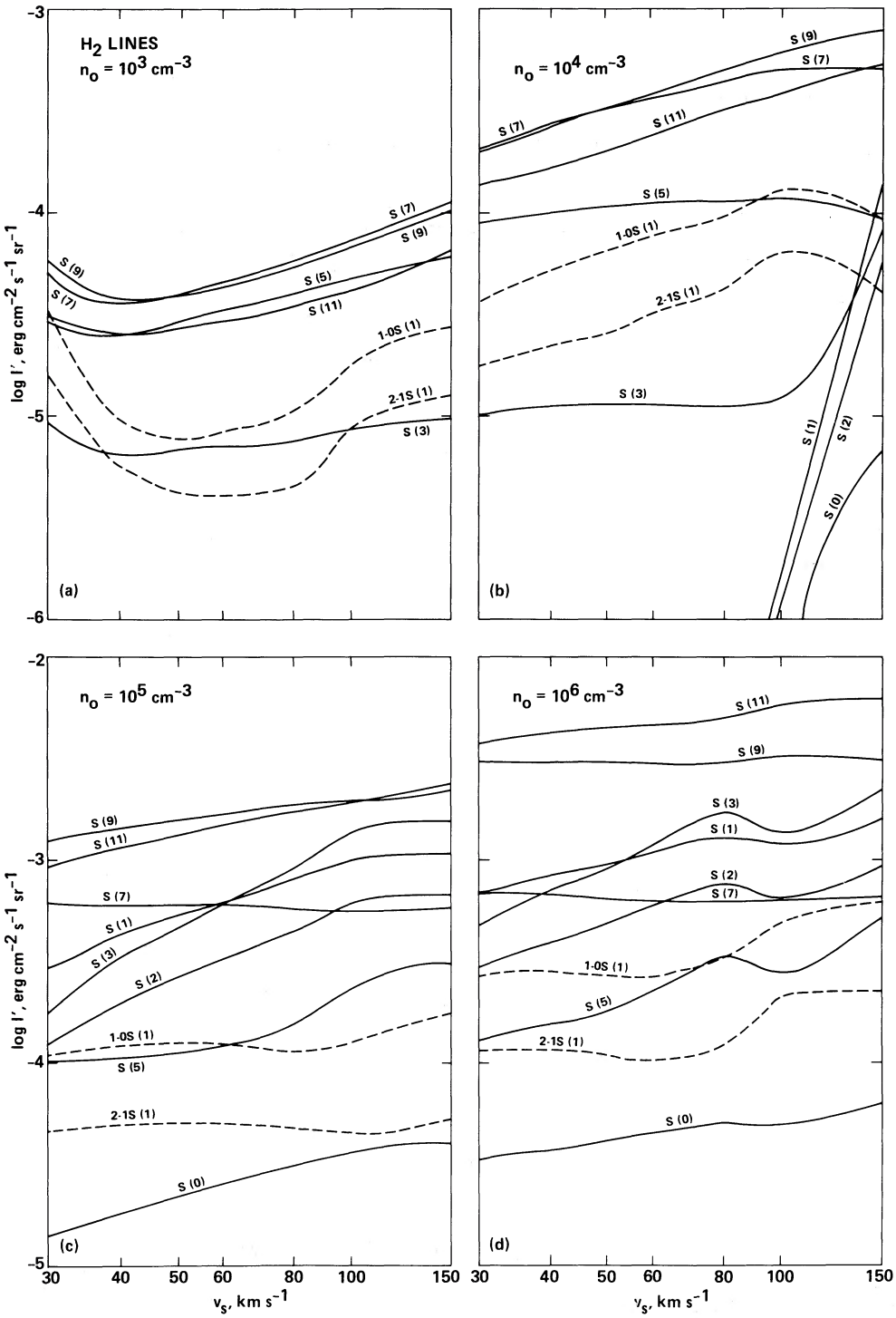

FIG. 5.—(*a–d*) Integrated H_2 intensities emergent normal to the shock for n_0 = (*a*) 10^3, (*b*) 10^4, (*c*) 10^5, and (*d*) 10^6 cm^{-3} are plotted as a function of v_s. The magnetic field is characterized by $b = 0.5$. The vibrational transitions are in dashed lines. Contributions from formation pumping and thermal collisions are evident (*see text*).

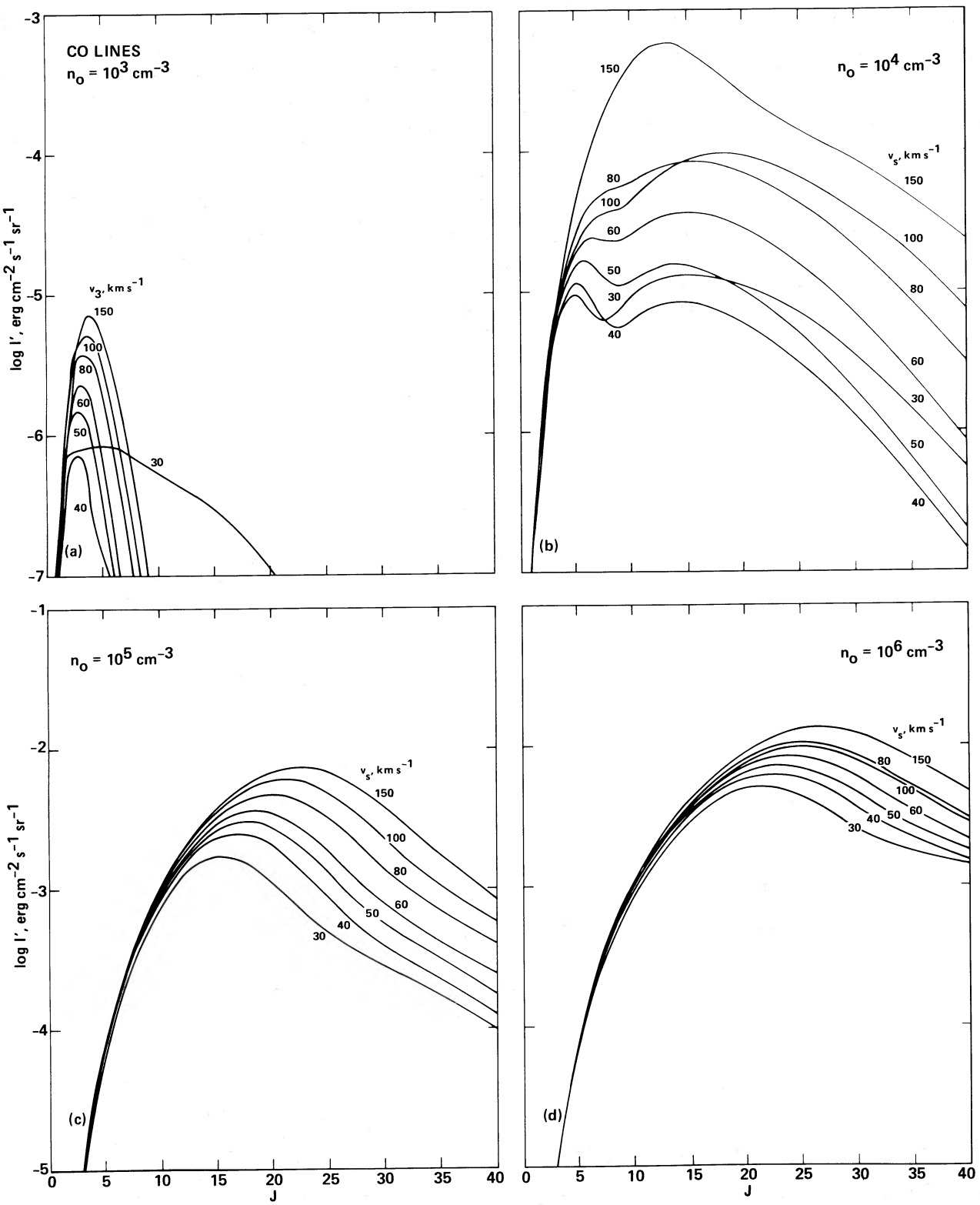

FIG. 6.—(*a–d*) Integrated CO line intensities emergent normal to the shock for $n_0 = (a)\ 10^3$, (*b*) 10^4, (*c*) 10^5, and (*d*) 10^6 cm^{-3} are plotted as a function of J, the upper level of the transition $J \rightarrow J - 1$. The shock velocities v_s in km s^{-1} are labeled on the different curves.

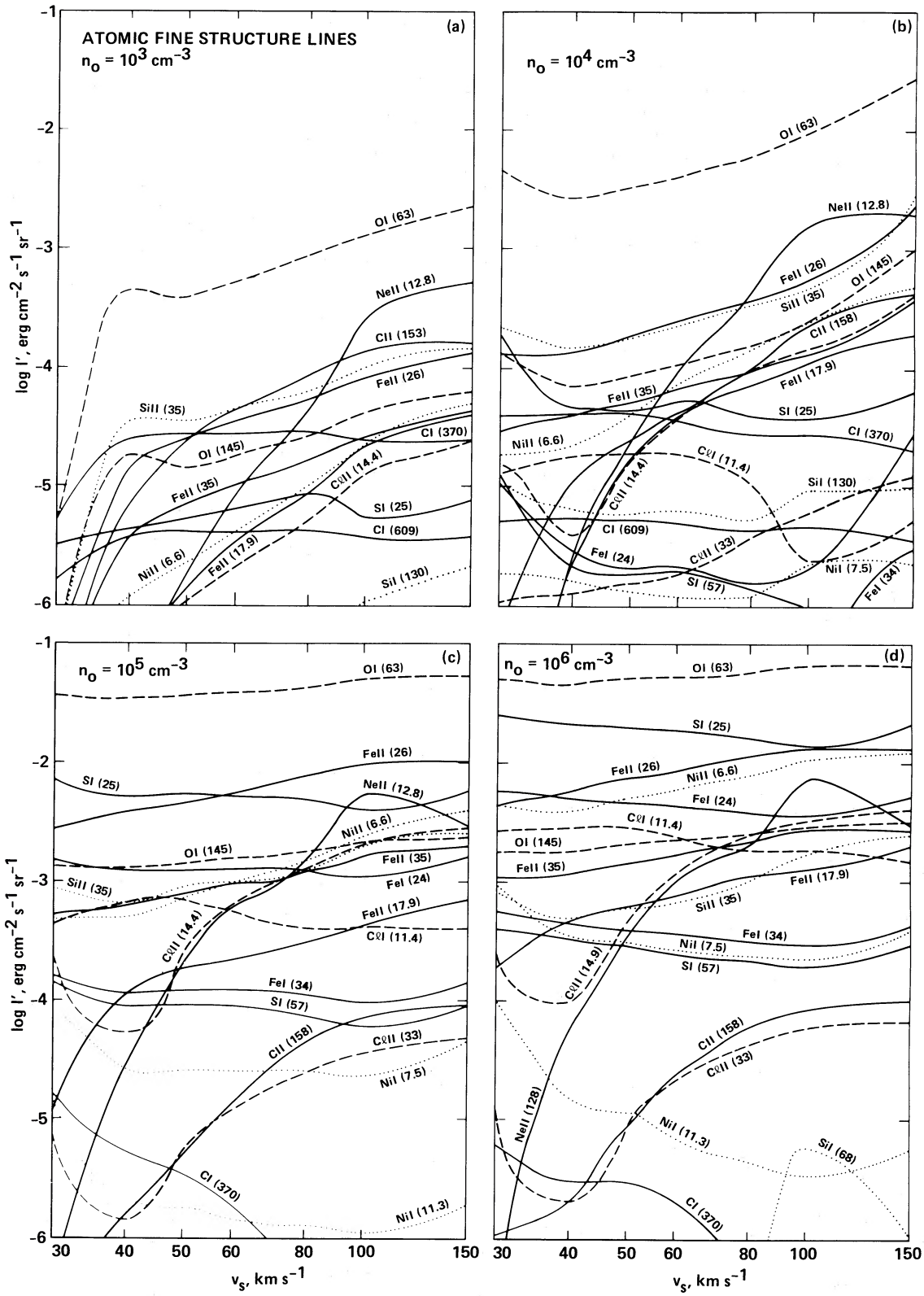

FIG. 7.—(*a–d*) Atomic fine-structure line intensities emergent normal to the shock for $n_0 = (a)\ 10^3$, $(b)\ 10^4$, $(c)\ 10^5$, and $(d)\ 10^6$ cm^{-3} are plotted as a function of v_s. Solid lines are used for transitions of C, Ne, S, and Fe; dashed lines for transitions of O and Cl; dotted lines for Si and Ni. The intensities for S, Fe, Cl, and Ni are upper limits because of the incomplete chemistry in the code (*see text*).

1. O I(63 μm) *versus particle flux.*—Hollenbach (1985) used preliminary results from this *J* shock code to point out that the O I(63 μm) intensity is proportional to the particle flux $n_0 v_s$ into a dissociative shock if $n_0 v_s \lesssim 10^{12}$ cm^{-2} s^{-1}; $I'(63\ \mu\text{m}) \simeq 10^{-13} n_0 v_s$ ergs cm^{-2} s^{-1} sr^{-1}, with n_0 and v_s in cgs units. This proportionality is caused by the dominance of O I(63 μm) cooling for $T \lesssim 5000$ K in these shocks. Each hydrogen nucleus entering the shock has $1.5k(5000\ \text{K})$ of cooling accomplished by O I(63 μm). One interesting application of this result was that the O I(63 μm) luminosity directly measured the mass loss rate from protostars, if the winds suffer "wind shocks."

Our new results verify this relation but show that the relatively good agreement at $n_0 v_s \sim 10^{12}$ cm^{-2} s^{-1} ($n_0 \sim 10^5$ cm^{-3}) is fortuitous if grains are present to catalyze the postshock chemistry. In this case, O I(63 μm) no longer dominates the cooling for $T < 5000$ K, but the H_2 formation heating provides extra energy to be radiated away in the neutral cooling gas.

2. *Shock regions versus photodissociation regions (PDRs).*—PDRs are also prodigious producers of fine-structure emission (see, e.g., Tielens and Hollenbach 1985*a*). These regions, powered usually by the ultraviolet fluxes from young, massive stars, are often associated with shock regions. For example, observations toward the BN-KL region contain both shock and PDR contributions as judged from the spatial morphology of the emission (see, e.g., Werner *et al.* 1984; Haas *et al.* 1986). Therefore, it is important to find an observational discriminant between shock and PDR emission, particularly for distance sources where spatial mapping may be inadequate.

The O I(63 μm)/C II(158 μm) intensity ratio may provide one such diagnostic. This ratio is generally $\lesssim 10$ in PDRs (Tielens and Hollenbach 1985*a*), but we note that the ratio is greater than ~ 10 in shock regions with $I'(63\ \mu\text{m}) \gtrsim 10^{-3}$ ergs cm^{-2} s^{-1} sr^{-1}. This is caused partly by the high postshock densities and temperatures, which favor O I(63 μm), and partly by the rapid conversion of C^+ to CO in the high-temperature, postshock chemistry, which suppresses the C II(158 μm) emission. This diagnostic relies on rather similar gas phase elemental abundances of C and O in shocks and PDRs; existing models of the BN-KL shock (Chernoff *et al.* 1982) and the Orion PDR (Tielens and Hollenbach 1985*b*) support this assumption since the models find that gas phase C and O abundances are nearly solar in both regions.

Another discriminant between shocks and PDRs is the velocity shift and velocity width of the observed lines. Since the shock emission occurs in postshock accelerated gas, the lines may be shifted appreciably ($\sim v_s$) from the velocity of the ambient molecular gas. In addition, since shocks with varying velocity vectors often lie in the beam of the telescope, shocked emission lines are usually quite broad, with FWHM of order of the typical shock velocity. In contrast, PDR emission lines are narrow, with FWHM of order of the turbulent velocity of the ambient gas (~ 1–5 km s^{-1} for typical molecular clouds) and are predicted to have little or no velocity shift with respect to the ambient molecular material.

Finally, the ratio of the integrated line emission to the integrated IR continuum emission in PDRs is necessarily small, $\sim 10^{-2}$–10^{-3}, because the photoelectric heating mechanism is inefficient and reaches an upper limit of $\sim 10^{-2}$ when the electron density is sufficiently high to produce neutral or negatively charged grains (see, e.g., Tielens and Hollenbach 1985*a*). In shocks, however, *most* of the energy is *initially* radiated in line emission from the gas. Grains in and near the shock often convert much of the optical and UV line luminosity from the shock into continuum luminosity, but the longer wavelength infrared line emission generally escapes to the observer. Thus, the ratio of integrated IR line emission to integrated IR continuum emission observed toward shocked regions is often the ratio of IR line emission to optical and UV line emission in the shock. This ratio is of order $\sim 0.1 v_{s7}^{-2}$, which is at least one order of magnitude larger than the PDR ratio if $v_{s7} \lesssim 1$.

3. *C shocks versus J shocks.*—An obvious discriminant of *J* shocks as opposed to *C* shocks is the observation of optical metastable lines such as O I λ6300 or hydrogen recombination emission, which are only produced in *J* shocks. However, molecular shock activity is often obscured so that a far-infrared discriminant is preferred. Intense O I(63 μm) emission [$I'(63\ \mu\text{m}) \gtrsim 10^{-2}$ ergs cm^{-2} s^{-1} sr^{-1}], if not PDR in origin, is probably an indication of *J* shocks, which dissociate molecules and radiate copiously in this line. *C* shocks, which have large molecular abundances, tend to rapidly convert any preexisting atomic oxygen into molecular form; therefore, their O I(63 μm) emission is weak. DRD, however, do produce $I'(63\ \mu\text{m}) \sim 3 \times 10^{-2}$ ergs cm^{-2} s^{-1} sr^{-1} from *C* shocks if $n_0 \simeq 10^6$ cm^{-3}, $v_s \simeq 10$ km s^{-1} and the preshock atomic oxygen abundance is assumed to be 50% of the cosmic abundance. Thus, the O I(63 μm) intensity many not be a clean discriminant between *C* and *J* shocks.

However, few ions exist in *C* shocks, which only form when the shocked gas is largely neutral and molecular. Therefore, the far-infrared observation of ionic lines is an extremely strong indication of *J* shocks if one has eliminated the possibility of H II or PDR origin for these lines. Figure 7 shows many strong ionic lines from *J* shocks. The best two candidates are probably Si II(35 μm) and Ne II(12.8 μm), since their chemistry has been more accurately treated [see below for comments relevant to Fe II(26 μm)]. We find that for $n_0 \gtrsim 10^5$ cm^{-3}, where the H_2 formation plateau exists at $T \sim 400$–500 K, the Si^+, is converted into SiO before the temperature drops below 450 K (thereby confirming that high *J* SiO rotational lines may be intense in such shocks, as pointed out by Neufeld 1987). This conversion significantly reduces the Si II(35 μm) intensity from the value it would have had without molecular chemistry. Nevertheless, the Si II(35 μm) intensity is one of the strongest ionic fine structure lines produced behind *J* shocks.

4. *Fine-structure intensities as a function of abundance.*—O I is the only fine-structure species which provides significant cooling to the shock and thereby influences shock structure; therefore, all other species have intensities which scale as the gas phase elemental abundances (see § II*b* for the standard values). We again caution that the S, Cl, Fe, and Ni lines must be viewed as upper limits, since our restricted chemistry for these species does not allow for their "depletion" into molecular form. In addition, Van Steenberg and Shull (1988) show that the depletion of Fe onto grains is also highly variable. Nevertheless, the S I(25 μm) and Fe II(26 μm) ground-state fine-structure transitions appear to be worthy candidates as strong new signatures of fast ($v_s \gtrsim 30$ km s^{-1}), dense ($n_0 \gtrsim 10^5$ cm^{-3}) interstellar shock waves. Cl II(14.4 μm) may be intense, but it lies in an opaque region of atmospheric transmission, inaccessible to either ground-based or airborne platforms. Cl I(11.4 μm), Fe I(24 μm), Fe II(18 μm, 35 μm), and Ni II(6.6 μm) are other potentially strong fine-structure lines from *J* shocks in molecular material.

5. *Signature of the* H_2 *formation plateau.*—Besides the pro-

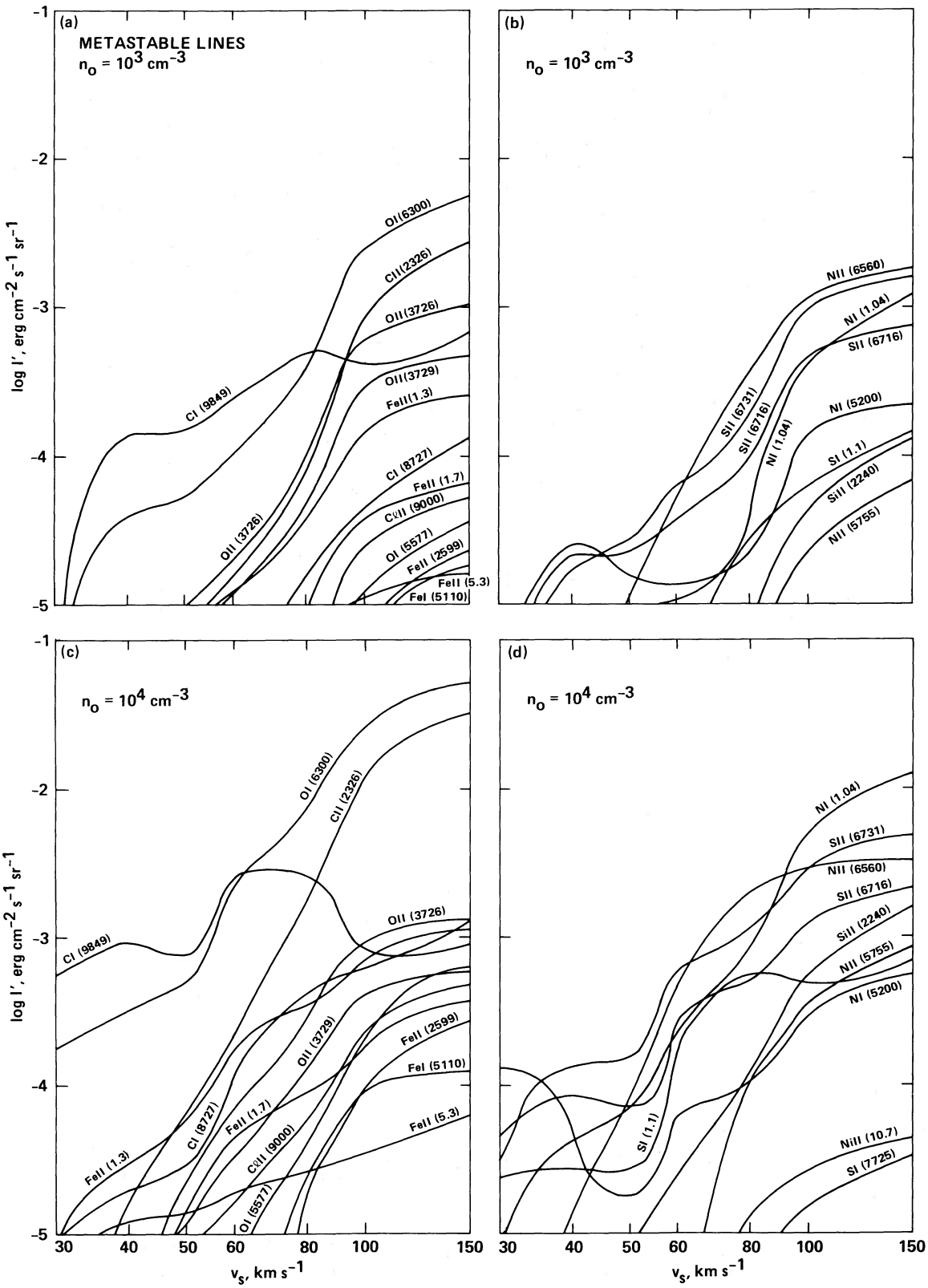

FIG. 8.—(*a–d*) Metastable line intensities emergent normal to the shock for $n_0 = 10^3$ and 10^4 cm^{-3} are plotted vs. v_s. The left-hand figures include transitions of O, C, Cl, and Fe. Note that the permitted Fe II λ2599 and Fe I λ5110 are also included. The right-hand figures include transitions of N, S, Si, and Ni.

duction of strong SiO (see Neufeld 1987), OH, CO, and H_2O high-J emission as well as low-J H_2 emission, the H_2 formation plateau produces a very sharp increase in the intensity of the neutral fine-structure lines S I(25 μm), Fe I(24 μm), Cl I(11.4 μm), and Ni I(7.5 μm). These line intensities increase (compare the $n_0 \geq 10^5$ cm^{-3} cases in Figure 7 with the lower density cases with no H_2 formation plateau) because the H_2 formation heating produces a significant column of heated but UV-shielded postshock material. As noted above, however, a more complete chemical code should be applied to test this preliminary result.

iv) *Metastable and Permitted Transitions*

Figure 8 plots the intensities of numerous metastable transitions of the neutral and singly-ionized states of O, C, N, S, Si, Fe, Cl, and Ni, as well as the permitted transitions Fe II λ2599 and Fe I λ5110. Because these (mostly) optical transitions are likely to be obscured in shocks with high preshock density ($n_0 \gtrsim 10^4$ cm^{-3}), Figure 8 shows results for $n_0 = 10^3$ and 10^4 cm^{-3} only. For three-level systems (0, 1, 2) we have generally presented the line intensities from transitions 1–0 and the strongest of 2–1 or 2–0. The remaining transition from level 2 can be obtained from the A values and energy levels given below in Table 9, in Appendix C. In the case where the lower electronic state of the transition is divided into fine-structure levels, we plot the intensity of the sum of the individual transitions. For example, the "C I λ9849" line is, in fact, the sum of the C I λ9849, C I λ9823, and C I λ9809 transitions from the ^1D state to the ground ^3P triplet. These lines are roughly in the ratio $3:1:2 \times 10^{-4}$. Likewise, the "O I λ6300" line is in fact, the sum of O I λ6300, O I λ6364, and O I λ6392 with very similar ratio, respectively.

Figure 8 shows that C I λ9849, O I λ6300, and C II λ2326 are the dominant coolants of the metastable transitions. Of the longer wavelength metastable transitions which may penetrate more obscure regions, N I(1.04 μm) and Fe II(1.3, 1.7 μm) are promising candidates. The line strengths plotted here may be useful in comparing with optical observations of Herbig-Haro regions, where dissociative shocks incident upon relatively dense gas may provide the excitation mechanism (see e.g., Schwartz 1983).

v) *Grains, H_2O, OH, and Other Important Coolants*

Figure 9 plots the total rotational molecular cooling intensities from the ground vibrational state transitions of CO, the total vibrational cooling intensity of CO, and the total (rotational + vibrational) intensities of H_2, OH, and H_2O. These last three molecular coolants are dominated by the rotational transitions of $v = 0$. We note that the H_2 intensity does not include the formation pump contributions in this figure, in contrast to the individual line intensities plotted on Figure 5. Figure 9 also plots the gas cooling caused by collisions with the dust grains. Finally, it replots the important O I(63 μm), O I λ6300, C I λ9849, and C II λ2326 atomic coolants so that a comparison of the dominant coolants in the $T \lesssim 10^4$ K postshock region can be made.

The grains, H_2O, and OH become dominant coolants for $n_0 \gtrsim 10^5$ cm^{-3} as the postshock densities become so large that collisional deexcitation suppresses other coolants relative to these species and, in addition, H_2O and OH attain higher

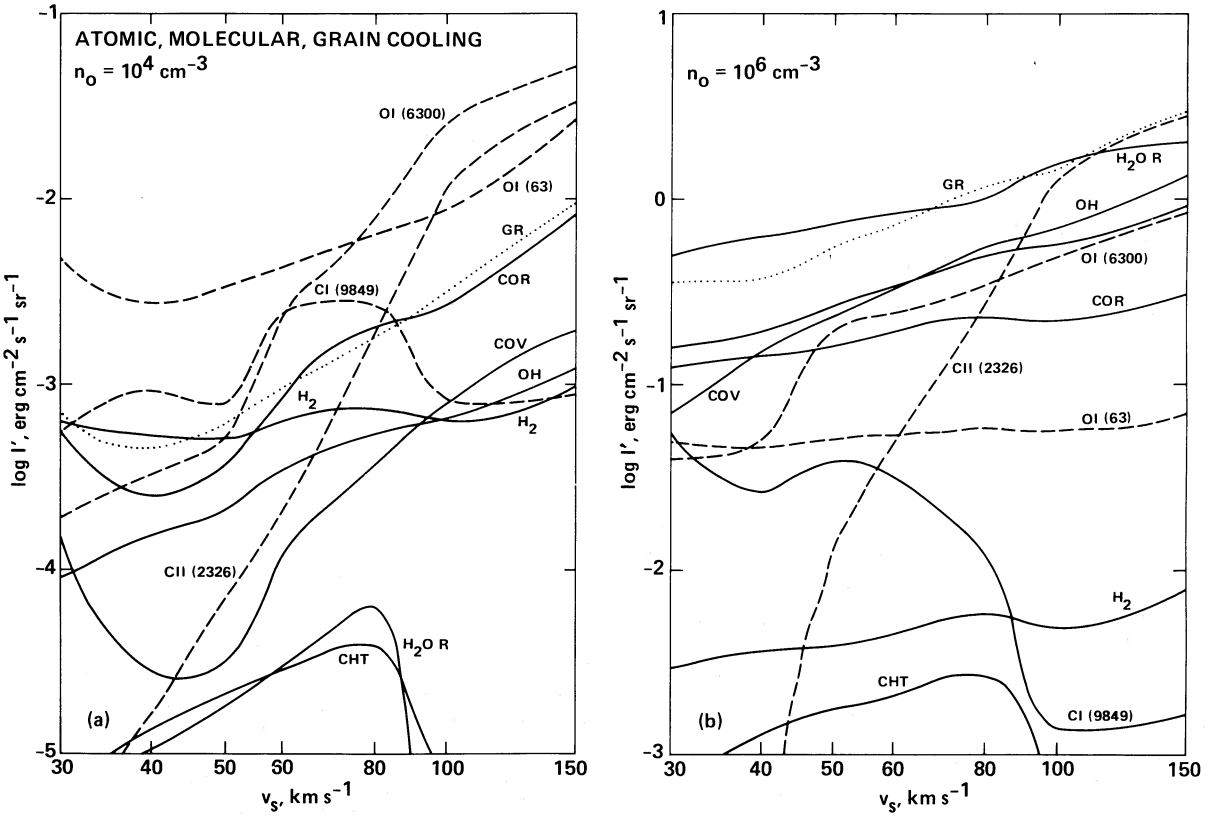

FIG. 9.—The integrated intensities from important molecules and atoms and the contribution to the grain IR continuum intensity from the collisional cooling of the hot gas (labeled GR) for (*left*) $n_0 = 10^4$ and (*right*) 10^6 cm^{-3}. COR is the sum of the rotational transitions of $v = 0$ CO; COV is the sum of the vibrational CO lines; CHT is the sum of the rotational transitions of CH, CH_2, CH_3, and CH_4; H_2, OH, and H_2O include both rotational and vibrational transitions.

abundances in the warm postshock H_2 formation plateau. A crude estimate of the individual rotational line strengths of the stong H_2O or OH transitions can be made by assuming a typical postshock temperature for these coolants of $T \sim 400$ K, and dividing the total intensities by the assumed number of strong rotational lines excited in this gas. Many lines are optically thick, and an accurate estimate of the individual line intensities requires a detailed calculation of the level populations and radiative transfer such as has been performed for *C* shocks by Neufeld and Melnick (1987). We defer such a treatment to a future paper.

vi) H *Recombination and Collisional Excitation*

Table 1 presents Hβ intensities as a function of n_0 and v_s, and Figure 10 plots the ratios of the intensities of various hydrogen lines to Hβ, $I'/I'_{H\beta}$. Table 1 shows that for a given v_s, $I'_{H\beta}$ scales as n_0 since the maximum postshock fractional ionization x_{max} and $N_{10^4\,K}$ are set mostly by v_s and $I'_{H\beta}$ scales as $x^2_{max} n_0 N_{10^4\,K}$. In addition, $I'_{H\beta}$ is very sensitive to v_s for $v_s \lesssim 80$ km s^{-1}, since at these velocities x_{max} increases rapidly with v_s. Thus, the absolute intensities of the hydrogen lines are good speedometers of shock waves if n_0 and the beam-filling factors are known.

Figure 10 shows the effect of both recombination and collisional excitation to the line intensities. Recombination tends to dominate Hα for $v_s \gtrsim 60$ km s^{-1} and the Br lines for $v_s \gtrsim 30$ km s^{-1}. Therefore, at low velocities the dominant collisional excitation tends to increase the Hα and decrease the Br lines relative to Hβ. At $v_s \sim 40$ km s^{-1} the low-density Br/Hβ ratios increase because of the density-dependent *l* mixing of a given *n* level which affects the effective *A* value for a given $n \rightarrow n'$ transition.

The infrared Br lines of hydrogen are also good diagnostics of *J* shocks versus *C* shocks. *C* shocks have such low levels of ionization, low atomic abundances, and low peak neutral temperatures that their Brackett emission is completely insignificant and undetectable. In contrast, dense *J* shocks embedded in molecular clouds can emit detectable numbers of Brackett photons which penetrate the intervening dust to the observer. One must be careful, however, to eliminate possible contamination from H II regions which may lie in the beam.

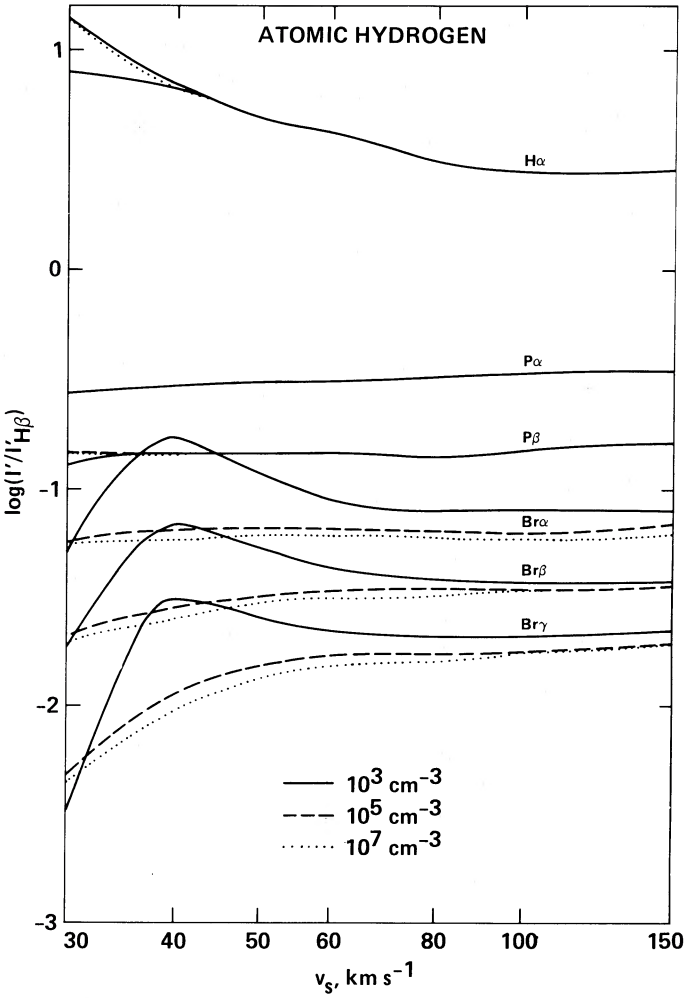

FIG. 10.—The ratio of atomic line intensities to that of Hβ are presented as a function of v_s for $n_0 = 10^3$ cm^{-3} (*solid lines*), 10^5 cm^{-3} (*dashed lines*), and 10^7 cm^{-3} (*dotted lines*). Contributions from both collisions and recombinations are included. Table 1 provides the absolute Hβ intensities for the parameter space studied.

d) Variation of the Standard Shock Spectrum with Other Parameters

Although the relative and absolute intensities of the lines are primarily a diagnostic of n_0, v_s and (implicitly) the beam filling factor, there are several other physical parameters which may cause significant variations in the line intensities. In order to gauge the effect of variation of these parameters, we have performed a parameter study of our standard case. The results are summarized in Table 2, which presents the postshock column densities and integrated intensities in important coolants for the standard case as well as numerous nonstandard cases.

i) *Variation with B*

The standard (*S*) case ($n_0 = 10^5$ cm^{-3}, $v_s = 80$ km s^{-1}) has a preshock field given by $b = 0.5$ ($B_{0\perp} \sim 150$ μG). Columns (3) and (4) of Table 2, labeled "BL" and "BH," give the results of the standard run with fields of $b = 0.1$ ($B_{0\perp} \sim 30$ μG) and $b = 10.0$ ($B_{0\perp} \sim 3$ mG). The principal effect of the magnetic

TABLE 1

Hβ INTENSITIES

n_0	v_s[a]	30	40	50	60	80	100	150
10^3.....		−9.12[b]	−5.31	−4.55	−4.09	−3.53	−3.16	−2.83
10^4.....		−5.77	−4.16	−3.40	−3.09	−2.44	−2.17	−1.83
10^5.....		−4.57	−3.22	−2.55	−2.06	−1.45	−1.17	−0.83
10^6.....		−3.47	−2.21	−1.60	−1.08	−0.51	−0.17	+0.17
10^7.....		−2.62	−1.23	−0.53	−0.13	+0.52	+0.84	+1.17

[a] v_s in km s^{-1}, n_0 in cm^{-3}.
[b] log $I'_{H\beta}$ in ergs cm^{-2} s^{-1} sr^{-1}.

TABLE 2

STANDARD VERSUS NONSTANDARD CASES

Parameter (1)	S[a] (2)	BL[b] (3)	BH[c] (4)	C[d] (5)	GR[e] (6)	HL[f] (7)	CO[g] (8)	HZ[h] (9)	UV[i] (10)
N_{100}[j]	5.6(21)[k]	1.7(21)	3.4(21)	4.2(21)	4.0(21)	2.2(21)	5.7(21)	2.4(21)	4.8(21)
N_{1000}[j]	1.9(20)	1.2(20)	1.3(21)	2.6(20)	1.5(20)	2.5(20)	2.0(20)	1.8(20)	1.6(20)
$H_2(T)$[l]	3.3(−3)[m]	1.4(−3)	7.7(−3)	1.6(−2)	1.8(−3)	4.9(−4)	3.4(−3)	7.9(−4)	2.6(−3)
1–0S(1)	1.0(−4)	4.8(−5)	1.1(−3)	8.1(−4)	1.5(−4)	1.4(−5)	1.0(−4)	3.2(−5)	1.5(−4)
2–1S(1)	4.0(−5)	1.5(−5)	4.3(−4)	3.2(−5)	7.0(−5)	4.5(−6)	3.9(−5)	6.8(−6)	6.0(−5)
S(9)	1.8(−3)	5.7(−4)	5.2(−3)	1.5(−3)	2.0(−3)	1.8(−5)	1.8(−3)	2.3(−5)	1.9(−3)
S(1)	8.4(−4)	2.9(−4)	1.1(−5)	9.8(−4)	4.8(−4)	1.8(−7)	8.5(−4)	1.4(−5)	5.6(−4)
Hβ	3.5(−2)	3.5(−2)	1.7(−2)	3.3(−2)	3.1(−2)	3.5(−2)	3.5(−2)	3.5(−2)	3.1(−2)
O I λ6300	6.7(−2)	7.0(−2)	5.2(−2)	1.4(−2)	5.4(−2)	6.8(−2)	6.8(−2)	6.5(−2)	5.9(−2)
C I λ9850	5.8(−3)	5.7(−3)	7.9(−3)	1.1(−2)	4.5(−3)	5.8(−3)	5.8(−3)	5.7(−3)	1.3(−2)
C II λ2326	2.3(−2)	2.2(−2)	9.2(−3)	2.8(−2)	2.3(−2)	2.3(−2)	2.3(−2)	2.1(−2)	1.7(−2)
N II λ6560	3.5(−3)	2.8(−3)	1.0(−2)	4.0(−3)	3.6(−3)	3.5(−3)	3.5(−3)	3.4(−3)	3.2(−3)
O I(63 μm)	4.5(−2)	2.2(−2)	5.4(−2)	1.1(−3)	3.7(−2)	2.3(−2)	4.5(−2)	1.8(−2)	3.7(−2)
Fe II(26 μm)	7.5(−3)	3.1(−3)	4.1(−3)	6.0(−3)	5.2(−3)	1.9(−3)	7.7(−3)	1.6(−3)	4.5(−3)
Si II(35 μm)	1.4(−3)	4.9(−4)	4.2(−3)	4.8(−3)	1.6(−3)	1.7(−3)	1.5(−3)	1.5(−3)	6.7(−4)
CO(T)[d]	8.4(−2)	6.4(−2)	7.6(−3)	8.8(−2)	6.1(−2)	2.7(−2)	8.3(−2)	3.3(−2)	2.3(−2)
CO(7–6)	2.9(−4)	1.6(−4)	1.5(−4)	1.7(−4)	2.5(−4)	1.0(−4)	2.9(−4)	1.3(−4)	2.6(−4)
CO(16–15)	3.8(−3)	2.3(−3)	3.6(−4)	3.2(−3)	3.1(−3)	5.6(−4)	3.8(−3)	8.6(−4)	3.2(−3)
CO(34–33)	8.1(−4)	1.0(−3)	1.7(−5)	1.3(−3)	5.6(−4)	5.6(−4)	7.8(−4)	6.4(−4)	5.9(−4)
$H_2O(T)$[d]	3.6(−2)	6.1(−2)	3.6(−4)	7.9(−5)	6.0(−3)	3.2(−4)	3.6(−2)	3.4(−4)	6.4(−2)
OH(T)[d]	2.4(−2)	5.4(−2)	3.9(−3)	1.3(−3)	9.6(−3)	3.5(−3)	2.5(−2)	6.2(−3)	2.0(−2)
GR	7.5(−2)	1.1(−1)	1.3(−2)	1.7(−1)	1.7(−1)	4.3(−2)	7.7(−2)	3.7(−2)	5.6(−2)

[a] S = standard.
[b] BL is a low magnetic field $b = 0.1$.
[c] BH is a high magnetic field $b = 10.0$.
[d] C has carbon abundance $x(C) = 2.3(-4)$ and oxygen abundance $x(O) = 1.0(-4)$.
[e] GR extends MRN grain distribution to 10 Å.
[f] HL sets H_2 formation on grains equal to zero.
[g] CO increases photodissociation of CO by a factor of ~ 3.
[h] HZ sets H_2 formation heating to zero.
[i] UV decreases FUV fluxes by a factor of 10.
[j] N_{100}, N_{1000} = postshock column density to $T = 10^2$ K, $T = 10^3$ K, in cm^{-2}.
[k] Column densities in cm^{-2}; numbers in parentheses represent powers of 10.
[l] $H_2(T)$, CO(T), OH(T), and GR represent the total cooling by these molecules and by grains, respectively.
[m] Intensities in ergs cm^{-2} s^{-1} sr^{-1}.

field is to change the maximum compression achieved in the postshock gas. High b results in less compression (eq. [2.4]), which in turn suppresses the formation of molecules, the local cooling rates (hence, larger $N_{100\,K}$ and $N_{1000\,K}$), and the H_2 formation heating (which requires $n > n_{cr}$).

The high B case, "BH," shows a markedly different structure from the standard case or "BL." The magnetic field is so high in this case that the immediate postshock compression is 3.25 (vs. the standard 4 for strong shocks) and the final postshock compression is only 5.5. Because of the reduced cooling rates, $N_{1000\,K}$ is increased by nearly one order of magnitude, but, because of the suppression of the H_2 formation plateau, the column $N_{100\,K}$ is not enhanced. The net result is a large difference, especially in the H_2 intensities. The formation pumped lines have less collisional deexcitation and are therefore stronger, but the (0–0)S(1) line, produced in the H_2 formation plateau for the lower b cases, is significantly less intense.

The integrated intensities in CO, OH, and H_2O lines are much smaller in the BH case because the gas cools before the chemistry produces significant amounts of these molecules. In contrast, the atomic and ionic lines tend to be somewhat stronger.

ii) *Variation with Abundances*

We have already noted that the intensities scale with the assumed abundances for the (optically thin) species which do not dominate the cooling and which, therefore, do not appreciably affect the T and n profiles of the shock. Case C in Table 2 represents a case which potentially could cause extreme differences in the postshock chemistry and structure: the gas phase abundance of oxygen is reduced by a factor of 5.4 so that the carbon abundance is greater than that of oxygen ($x_C = 2.3 \times 10^{-4}$, $x_O = 1.0 \times 10^{-4}$).

Case C shows a drop in the O I λ6300 intensity and an increase in the intensity of other metastable coolants as well as in $N_{1000\,K}$ because of the decrease in x_O. The increase in $N_{1000\,K}$ results in a significant contribution to the (1–0)S(1) intensity from collisions, as opposed to formation pumps, and relatively large changes in the (1–0)S(1) intensity and the (1–0)S(1)/(2–1)S(1) ratio. The O I(63 μm), OH, and H_2O intensities drop significantly because, once CO has formed, little oxygen is left for the other species.

iii) *Variation with Grain Size Distribution*

The grain size distribution affects the formation of H_2, the recombination of ions, and the grain cooling of the gas. Case GR varies the latter two rates ($\propto a_{min}^{-0.5}$) by assuming that the MRN distribution extends to $a_{min} = 10$ Å, instead of the $a_{min} = 100$ Å of the standard case. This case enables us to probe the effect of a substantial population of small grains or polycyclic aromatic hydrocarbons (PAHs), whose existence has been inferred recently through infrared observations (see, Tielens 1989). The H_2 formation rate is held fixed to that of the standard rate in GR; we defer the variation of this rate to § IIIe(i) below. GR differs from standard case minimally, with the exception of the OH and H_2O intensities, which decrease

significantly. The increased grain cooling rates lower the temperature of the H_2 formation plateau by $\sim 10\%$, and the OH and H_2O peak abundances in the plateau are extremely T-sensitive, as can be seen from their formation rate coefficients (Appendix B). The integrated ionic intensities Si II(35 μm) and Fe II(26 μm) decrease only slightly because their ionization is controlled by FUV photoionization and the postshock column density where they neutralize is controlled primarily by dust attenuation of the FUV flux.

e) Uncertainties in Postshock Physical Processes

The postshock physical processes are sufficiently complex and some of the rates sufficiently uncertain that it is useful to obtain a measure of the robustness of the results. We have compared our results to completely independent J shock models of Hartigan *et al.* (1987) and Neufeld (1987). The Hartigan *et al.* results focused on the optical emission from relatively low-density ($n_0 \leq 10^3$ cm^{-3}) atomic shocks. We have compared their $n_0 = 10^3$ cm^{-3}, $v_s = 80$ km s^{-1}, $B_{0\perp} = 0.1$ μG run with our $n_0 = 10^3$ cm^{-3}, $v_s = 80$ km s^{-1}, $B_{0\perp} = 15$ μG run. Their preshock conditions are assumed to be largely atomic, while our preshock conditions are largely molecular. Nevertheless, the metastable and hydrogenic line intensities agree generally to within a factor of ~ 2, which is quite within expectations considering the differences in abundances, the preshock magnetic field, and the preshock chemistry. The largest discrepancy is in the S II $\lambda\lambda$6716, 6731 intensities, which are a factor of ~ 8 larger in our run. This is primarily due to the lower postshock densities due to the magnetic pressure in our run, with a small contribution caused by our neglect of S III, which Hartigan *et al.* include.

The Neufeld (1987) results focused on the chemistry and emission from J shocks in molecular gas, and we have run a standard case with the same H_2 formation rate and elemental abundances as Neufeld. Overall, the agreement between our run and Neufeld's $n_0 = 10^5$ cm^{-3}, $v_s = 80$ km s^{-1} run is good—within a factor of 2 for most of the line intensities and overall shock structure parameters. The main difference seems to be that we have assumed smaller (by a factor of 5) cross sections for OH cooling than Neufeld. As a result, although we agree in this case that OH is the dominant coolant at $T \sim 1000$ K (using Neufeld's higher H_2 formation rates which accelerate the chemistry), our run produces a somewhat higher temperature H_2 formation plateau. Therefore, our individual high-lying (T-sensitive) molecular lines are much more intense than Neufeld's; for example, our CO(34–33) is a factor of 3 higher. We note that, using *our* standard H_2 formation rate coefficient, the OH cooling in the standard case is not as dominant (see Fig. 4), and the results are not nearly as sensitive to the OH cross sections. Another difference with Neufeld is that we find a significant contribution to the H_2 emission from formation pumping, a process which is not included in his work.

An alternate way to test the robustness of the results is to vary some of the more uncertain parameters which characterize the postshock processes. Table 2 includes several such cases.

i) *Uncertainties in the Postshock Chemistry*

The two major uncertainties in the chemistry are the rate of H_2 formation on grains and the rate of CO photodestruction. The first is uncertain because of the elevated grain temperatures in the postshock material. For example, the standard shock has $T_{gr} \sim 50$ K. The formation of H_2 at these high grain temperatures can be suppressed because of the rapid evaporation of H atoms prior to forming molecules; formation relies on (partial) chemical binding or enhanced binding sites which hold the atomic hydrogen (see HM79). Our theoretically estimated H_2 formation rates are close to the physically plausible upper limits. Therefore, we have run a case with the H_2 formation on grains set equal to zero, case HL in Table 2. Interestingly enough, photoelectric heating by grains is sufficient to provide a temperature plateau at $T \sim 200$ K and the H^- mechanism produces sufficient H_2, $x(H_2) \sim 10^{-3}$, to allow a large abundance of CO, $x(CO) \sim 10^{-4}$, to form. The net result is that the H_2, H_2O, and OH lines are much weaker (although note that the H_2 vibrational lines and the OH total intensity are reduced by only a factor of ~ 10), while the atomic, ionic, grain, and CO intensities are relatively unaffected.

CO photodissociation is uncertain because of the simplistic manner in which we have treated self-shielding. We have smoothed the radiation field over a very coarse (11.2–13.6 eV) bin instead of treating the overlap of the shock UV emission lines with the CO lines which initiate photodissociation. We have ignored the shielding by H_2 lines of the discrete frequencies which photodissociate CO. Therefore, to test the sensitivity of the integrated intensities to our simplifying assumptions, we have increased the unshielded rate of photodissociation (see eq. [2.11]) by a factor of 3 in case "CO" of Table 2 (to $\sim 2 \times 10^{-10}$ s^{-1} in the ambient interstellar field). It is reassuring to see that the integrated intensities for $J < 34$ are decreased by less than 5%; the photodissociation of CO is still negligible in the regions where CO cooling is important.

ii) *Uncertainties in H_2 Formation Heating*

Although it is quite likely that newly formed H_2 molecules escape grain surfaces on extremely short time scales ($\sim$vibrational period), it might be argued that H_2 molecules transfer their formation energy to the grain before their departure. In such a case, there is no H_2 formation heating of the gas, and the H_2 formation plateau disappears. In addition, the formation pumping of H_2 lines is inoperant. Case HZ in Table 2 plots this case of newly formed H_2 molecules leaving the grains in $v = 0$ and $J = 0$ or 1. The H_2 line intensities drop significantly because of the lack of formation pumping and the absence of an H_2 formation plateau. OH, and especially H_2O, drop because the lack of an H_2 formation plateau means that the high-temperature chemistry cannot produce high OH and H_2O abundances. As discussed previously, the intensities of the neutral fine-structure lines S I(25 μm), Fe I(24 μm), Cl I(11.4 μm), and Ni I(7.5 μm) decrease significantly in the case of no H_2 formation plateau. In the other extreme, if all the H_2 binding energy is transferred to H_2 translational energy upon formation, then we would obtain a temperature plateau in low-density ($n_0 \lesssim 10^5$ cm^{-3}) shocks, since the collisional deexcitation of vibrationally excited H_2 is not required.

iii) *Uncertainties in the Radiation Field*

The mean intensity of the FUV radiation field at a given point in the postshock gas depends upon the shock geometry, the ultraviolet scattering and absorption properties of the grains, and the complex scattering by hydrogen atoms of the very optically thick Lyα line. Although we feel that our treatment of the FUV intensity is probably accurate to a factor of ~ 3, we have run a case where the FUV fluxes in the three wavelength bins are decreased by a factor of 10 (case "UV" in Table 2). In general, the integrated intensities change by less than a factor of 2.

IV. POTENTIAL APPLICATIONS

The detailed application of these results to specific regions of J shock emission is deferred to separate and future papers. Here we outline four types of objects in which these models may be quite useful and present and review some preliminary results.

a) Herbig-Haro Objects

Cohen *et al.* (1988) compare O I(63 μm), O I λ6300, and H_2 (1–0)S(1) intensities from HH 7-11, T Tau, HH 42A, and HH 43 with preliminary results from these J shock calculations in order to constrain n_0, v_s, and the shock area filling factors toward these sources. Because the observed ratios O I(63 μm)/H_2 (1–0)S(1) ~ 10, whereas the J shock models predict ratios $\gtrsim 100$ (see Figs. 5 and 7), Cohen *et al.* postulate the existence of lower velocity, nondissociating C shocks which dominate the H_2 (1–0)S(1) emission. We also note that dissociating J shocks would also produce lower ratios (~ 3) of (1–0)S(1)/(2–1)S(1) than are observed (~ 10). In addition, using the method described in § III*c*(iii)1, Cohen *et al.* use the observed O I(63 μm) luminosity to estimate mass loss rates ($\sim 10^{-5.5}$–10^{-7} $M_\odot$ yr^{-1}) from the stars exciting these HH objects.

Currently, because of the low beam-filling factors and low preshock densities ($n_0 \lesssim 10^{3-4}$ cm^{-3}), the J shocks in HH objects are not likely to be observed in far-infrared lines other than O I(63 μm). C II(158 μm), Si II(35 μm), and Fe II(26 μm) all have intensities which lie a factor of $\gtrsim 10$ below O I(63 μm).

In the near and mid-infrared, we point out that (besides the H_2 emission which may be dominated by any C shocks present) the Ne II(12.8 μm), Fe II(1.3 and 1.7 μm), Si I(1.1 μm), N I(1.04 μm), and C I λ9840 lines may be helpful J shock diagnostics in HH objects. These transitions suffer less extinction than the intrinsically stronger O I λ6300, N II λ6560, and S II $\lambda\lambda$6717, 6731 metastable transitions.

b) Winds from Protostars

McKee and Hollenbach (1987) discuss the morphology produced by protostellar winds interacting with the ambient molecular cloud. A "two-shock" structure is rapidly produced, with the free-flowing wind impacting a shell which is being supersonically driven into the ambient medium. A shock bounds each side of the shell; the inner shock is called the "wind shock," where the wind decelerates as it enters the shell; the outer shock is called the "ambient" or "molecular" shock, where the ambient gas is accelerated to the shell velocity. McKee and Hollenbach (1987) show that the wind from IRc2 in Orion BN-KL may produce such a morphology, and model the wind shock as an $n_0 = 3 \times 10^4$ cm^{-3} and $v_s = 70$ km s^{-1} J shock with a beam filling factor of ~ 4, corresponding to a spherical shell which fills the beam. Such a shock explains both the molecular shock parameters (see Chernoff *et al.* 1982) as well as the H51α recombination line observed in the shock by Hasegawa and Akabane (1984). Figure 7 shows that such a shock is predicted to produce an O I(63 μm) intensity of $\sim 6 \times 10^{-2}$ ergs cm^{-2} s^{-1} sr^{-1} and a Si II(35 μm) intensity of $\sim 2 \times 10^{-3}$ ergs cm^{-2} s^{-1} sr^{-1} if the Si abundance is depleted by a factor of ~ 10 from solar abundance. Werner *et al.* (1984) and Haas *et al.* (1986) observed the shock contribution of these lines to be 1.5×10^{-2} and 2.5–4.5×10^{-3} ergs cm^{-2} s^{-1} sr^{-1}, respectively (in a 1′ beam). We therefore find that the fine-structure observations may be better matched with a smaller beam filling factor of ~ 1, and a silicon abundance that is nearly solar (as may be expected in a grainless wind, or in postshock gas if significant shock destruction of grains occurs). In such a model, the observed upper limit to the Brα dereddened intensity of $\sim 3 \times 10^{-4}$ ergs cm^{-2} s^{-1} sr^{-1} at Peak 1 (Geballe and Garden 1987) is about equal to the expected intensity for a shock at normal incidence with a beam filling factor of unity (see Table 1 and Fig. 10). This model fails, however, by a factor of 4, to produce the H51α observations of Hasegawa and Akabane. A remeasurement of the H51α emission from the shock and sensitive mapping of the BN-KL region in infrared recombination lines of hydrogen, such as Brα, are essential if the dynamics of the outflow is to be elucidated.

c) Supernova Remnants Interacting with Molecular Clouds

To date, there are not many known examples of supernova remnants interacting with molecular clouds and IC 443 is the best known example (see, e.g., deNoyer 1979*a*, *b*; Burton *et al.* 1988 and references therein). Burton *et al.* (1988, 1989) observed H_2 (1–0)S(1) and O I(63 μm) and set upper limits to the Si II(35 μm) and high J CO emission at the peak of the H_2 emission. Burton *et al.* (1989) used the preliminary results of the J shock results presented here to constrain n_0, v_s, and shock-filling factors in IC 443. Like the case of HH objects, they find that the H_2 (1–0)S(1) intensity is too large relative to O I(63 μm) to be explained by dissociative J shock emission, so that a mix of lower velocity, nondissociating C shocks and higher velocity J shocks may explain the observations.

Graham, Wright, and Longmore (1987) used preliminary results of the J shock results to interpret their observed Fe II(1.664 μm) emission (our "1.7" μm line is a blend of 1.644 and 1.681 μm Fe II lines) in IC 443 as shock emission. This confirms the potential importance of these lines as shock diagnostics.

Burton *et al.* (1989) conclude that the O I(63 μm) flux contributes $\gtrsim 30\%$ to the observed *IRAS* 60 μm flux and that H_2, O I(63 μm), and H_2O line emission may exceed the grain continuum emission toward the H_2 (1–0)S(1) peak in IC 443. As discussed above, this confirms the shock, as opposed to PDR, origin of this emission.

Intense and broad O I(63 μm) line emission may be a signature of hithertofore undiscovered supernova remnants deeply embedded in molecular clouds. Such "buried" supernova remnants are predicted to be strong infrared sources (Shull 1980; Wheeler, Mazurek, and Sivaramakrishnan 1980). A search of unidentified strong *IRAS* sources in the galactic plane for broad (FWHM $\gtrsim 100$ km s^{-1}) O I(63 μm) emission is suggested.

d) H_2O *Masers*

H_2 formation heating behind J shocks in dense ($n_0 \gtrsim 10^6$ cm^{-3}) gas produces an extended temperature plateau of warm gas rich in H_2O. For example, if $n_0 = 10^7$ cm^{-3} (a case to be considered in detail in a future paper) and $v_{s7} = 1$, then the temperature of the plateau is 400–500 K, its column density is $\sim 3 \times 10^{22}$, and its density is $\sim 10^9$ cm^{-3} ($b \sim 0.5$). Such a slab provides a natural environment for H_2O masers since the characteristic size scale ($N/n \sim 3 \times 10^{13}$ cm) and gas density match the observed or inferred H_2O maser parameters, the postshock chemistry naturally produces high ($x \gtrsim 10^{-4}$) H_2O abundances, and the high gas temperature provides a natural explanation for excitation of the maser—collisions with thermal H

atoms and H_2 molecules. Elitzur, Hollenbach, and McKee (1989) have performed a detailed calculation of H_2O masing behind these J shocks, and conclude that brightness temperatures up to 10^{13-15} K can be achieved. This model provides a natural explanation for galactic water masers, and it may account for the more luminous extragalactic water masers as well.

V. CONCLUSIONS

Shocks in molecular gas are beacons which reveal the energetic processes occurring there, particularly those associated with star formation. The structure of such shocks depends on the relative importance of radiative losses and ambipolar diffusion. If the radiation length scale exceeds the ambipolar diffusion length scale, which is typically the case for atomic gas, then the shock front has the classical form in which the density and temperature of the upstream gas "jump" to their downstream values in about one mean free path or less. Such shocks are termed J shocks. Interstellar shocks are J type for shock velocities exceeding 40–50 km s^{-1} for typical magnetic field strengths; at such velocities, the shocks are dissociative.

We have studied the structure and emission spectrum of J shocks in molecular gas over a broad range of conditions. We have treated shock velocities in the range $v_s = 30$–150 km s^{-1} and preshock densities $n_0 = 10^3$–10^6 cm^{-3}. The component of the magnetic field normal to the shock velocity has been taken to be $0.5 \times 10^{-6} n_0^{0.5} G$ (corresponding to an Alfvén velocity of 0.9 km s^{-1}), which limits the final compression of the gas. Our work extends previous calculations of interstellar shocks in atomic gas (e.g., Cox 1972; Dopita 1977; Raymond 1979; Shull and McKee 1979) to higher densities and includes the dominant chemistry that occurs behind the shock front. The fact that the gas is initially molecular rather than atomic in our calculations is not essential, since the molecules are completely dissociated in the shock in any case. At low densities ($n_0 \lesssim 10^3$ cm^{-3}) the chemistry has only one significant effect on the emission spectrum: the H_2 formed on the grains produces a rovibrational spectrum similar to that of a UV pumped source as the newly formed, excited H_2 molecules cascade down to the ground state. In this case the chemistry occurs at such low temperatures that collisional excitation of H_2 or of the other molecules that form is indistinguishable from that of cold, dense ambient gas.

The principal result of our analysis is that at high densities ($n_0 \gtrsim 10^{4-5}$ cm^{-3}) chemistry has a profound effect on the emission spectrum: the density behind the shock is sufficient high that some of the internal energy of the newly formed H_2 molecules is transformed to the gas as heat by collisional deexcitations, producing the H_2 *formation plateau.* In this temperature plateau, endothermic reactions and neutral-neutral chemical reactions with activation energies can proceed efficiently, producing significant quantities of *warm* H_2, CO, OH, and H_2O and enhanced columns of *warm* atoms and ions. The heat generated by the H_2 formation is radiated in collisionally excited atomic fine-structure lines [particularly O I(63 μm), Si II(35 μm), S I(25 μm), Fe I(24 μm), Fe II(26, 35 μm), Cl I(11.4 μm), and Ni II(6.6 μm)] and molecular rotational lines (H_2 and CO, and, for $n_0 \gtrsim 10^5$ cm^{-3}, OH and H_2O). Observation of strong emission of these lines, or of the formation-pumped high v transitions of H_2 would provide observational verification that newly formed (on grains) H_2 molecules are ejected into the gas in high v states. Our estimates for the line intensities from the species S, Fe, Cl, and Ni may be upper limits because we have not included these elements in the chemical reaction network, but only follow their ionization and recombination. On the other hand, their gas phase abundances may be higher than we have assumed, which could produce greater intensities than those predicted.

Interstellar J shocks can be distinguished spectroscopically from their cousins, interstellar C shocks, through observation of hydrogen recombination lines and fine-structure lines from ions, such as Ne II(12.8 μm), Si II(35 μm), and Fe II(26, 35 μm), since the ion abundance in C shocks is very low. (Of course, J shocks also have higher velocities than C shocks, but the shock velocity is sometimes difficult to measure directly: an emission line from a high-velocity J shock can have a low-velocity shift if the velocity vector lies nearly perpendicular to the line of sight or, conversely, an emission line from a low-velocity C shock traversing a high-velocity clump may produce a high velocity shift). The spectrum of an interstellar J shock differs from that of a photodissociation region around a massive star in several respects: the line widths are substantially larger in the shock; the line to continuum ratio is higher in the shock; and the O I(63 μm)/C II(158 μm) ratio is larger for the shocks, provided the O I(63 μm) is strong.

We have considered the applications of these results only briefly, deferring a more detailed discussion to other papers. The spectra of Herbig-Haro objects and of shocked gas in the supernova remnant IC 443 show evidence for both J shocks and C shocks (see Cohen *et al.* 1988 and Burton *et al.* 1989, respectively). Intense, broad O I(63 μm) emission is predicted to be a primary spectroscopic signature of a supernova remnant buried in a molecular cloud. In the BN-KL region of Orion, there is evidence for a J-type wind shock as well as for a C shock which produces the strong H_2 and CO emission, but detailed mapping of this region in infrared hydrogen recombination lines is required to clarify the situation (McKee and Hollenbach 1987). The O I(63 μm) luminosity from "wind shocks" may provide a good estimate of the mass-loss rates from protostars (Hollenbach 1985). Finally, at very high densities ($n_0 \gtrsim 10^6$ cm^{-3}) the H_2 formation temperature plateau is an ideal site for H_2O masers. Elitzur *et al.* (1989) have argued that shocks in dense gas can account for the observed properties of galactic H_2O masers and possibly extragalactic ones as well.

We would like to acknowledge helpful discussions with D. Chernoff, A. Dalgarno, B. Draine, T. Jernigan, D. Neufeld, and S. Prasad. The comments of the referee, M. Shull, were extremely valuable. N. Jennerjohn, P. Rauckhorst, and J. Varney provided valuable assistance with figures and tables. This work has been conducted in part under the auspices of a special NASA astrophysics theory program which supports a joint Center for Star Formation Studies at NASA Ames Research Center, U. C. Berkeley, and U. C. Santa Cruz. D. J. H. acknowledges additional support through NASA RTOP 188-41-53. The research of C. F. M. is supported in part through NSF grant AST86-15177.

APPENDIX A

PHOTOIONIZING PRECURSOR

Radiation emitted behind the shock front travels upstream and heats, dissociates, and ionizes the unshocked gas. This radiative precursor self-consistently alters the structure of the shock: since the number of particles per hydrogen nucleus, x_t, is increased, the temperature just behind the shock is decreased (eq. [2.5]); on the other hand, less energy of the shocked gas goes into collisional dissociation and ionization. Shull and McKee (1979) developed the theory of ionizing radiative precursors for shocks in atomic gas. Here we shall generalize their treatment somewhat and apply it to shocks in molecular gas.

H_2 can be dissociated through (1) absorption of Lyman-Werner band photons followed by a transition to the vibrational continuum; or (2) by photoionization to H_2^+ followed by dissociative recombination or by other chemical reactions. The first path is relatively unimportant because the number of photons in the Lyman-Werner bands generated behind the shock is small compared to the particle flux through the shock and, in any case, only $\sim 10\%$ of the absorptions result in dissociation.

Photoionization of H_2 requires photons with $h\nu > 15.4$ eV. Once the H_2^+ is formed, there are three major possibilities.

1. *Dissociative recombination.*—Hickman (1987) has calculated the cross section for dissociative recombination of H_2^+ for electron energies above 0.03 eV. Assuming that the rate coefficient γ varies as $T^{-0.5}$, we estimate $\gamma = 8 \times 10^{-8}(T/300)^{-0.5}$ cm^3 s^{-1} from his results.

2. *Reaction with H_2 to form H_3^+.*—The reaction rate for this process is 2.1×10^{-9} cm^3 s^{-1} from Table 4 below, so it competes with dissociative recombination only for low ionization: $x_2\gamma(H_2 + H_2^+ \rightarrow H_3^+ + H) > x_e\gamma(H_2^+ + e \rightarrow H + H)$ implies $x_e \lesssim 0.01$ for $T \lesssim 300$ K. The fate of the H_3^+ is uncertain because its dissociative recombination rate in unknown. It is believed to be low in the ground (the value in Table 4 is consistent with the upper limit set by Smith and Adams 1984), although a high value has been reported for H_3^+ in the ground vibrational state but not necessarily the ground rotational state (Amano 1988). Here we shall assume that if dissociative recombination of H_3^+ is important, then the channel $H_3^+ + e \rightarrow H_2 + H$ is dominant so that $H_2^+ + H_2 \rightarrow H_3^+ + H$ and $H_3^+ + e \rightarrow H_2 + H$ leads to 2 neutral atomic hydrogens. This outcome is the same as that for the direct dissociative recombination of H_2^+.

3. *The H_2^+ can be swept through the shock before it has time to react.*—The characteristic column density of the precursor is $[\sigma(\text{photoionization})]^{-1} \sim 10^{17}$ cm^{-2}, so the flow time through the precursor is $t_{\rm pre} = N/n_0 v_s \sim (10^{10}/n_0 v_{s7})$ s. The number of dissociative recombinations per H_2^+ for an H_2^+ formed halfway through the precursor is then $0.5 n_e \gamma(H_2^+ + e \rightarrow H + H) t_{\rm pre} = 400 x_e/v_{s7}$, which is greater than unity for $x_e > v_{s7}/400$. We conclude that once the precursor ionization rises above 1%, photoionization of H_2 leads to the formation of two neutral hydrogen atoms. The H is subject to further photoionization, but it does not have time to recombine unless the precursor becomes fully ionized and an ionization front propagates ahead of the shock (a case we do not consider).

Since the dominant reactions in the precursor are of the form

$$A_j + h\nu \rightarrow \eta_j A_{j+1} + \mu_j e^- , \tag{A1}$$

where $(\eta_j, \mu_j) = (2, 0)$ for photoionization of H_2 and (1, 1) for photoionization of H, the rate of change of species j can be expressed as

$$\frac{dn_j}{dt} = \eta_{j-1} n_{j-1} \int_0^\infty 4\pi J_\nu^*(t)\sigma_{j-1}(\nu)d\nu - n_j \int_0^\infty 4\pi J_\nu^*(t)\sigma_j(\nu)d\nu , \tag{A2}$$

where J_ν^* is the mean photon intensity (in photons cm^{-2} s^{-1} Hz^{-1} sr^{-1}) and $\sigma_j(\nu)$ is the photoionization cross section (see, e.g., Shull and McKee 1979). Because J_ν^* is the mean photon intensity irradiating a particular fluid element, it increases with time as the fluid element approaches the shock front. Let

$$y_j = \int_{-\infty}^t dt' \int_0^\infty 4\pi J_\nu^*(t')\sigma_j(\nu)d\nu , \tag{A3}$$

which is the total number of ionizations per particle j experienced up to time t. Equation (A2) then becomes

$$\dot{n}_j = \eta_{j-1}\dot{y}_{j-1} n_{j-1} - \dot{y}_j n_j , \tag{A4}$$

where the dots denote time derivatives. This equation ensures conservation of the constituent particles; for example, in a three-species system

$$\eta_1\eta_2 n_1 + \eta_2 n_2 + n_3 = \text{constant} . \tag{A5}$$

To solve (A4) we assume that the y_j are all proportional to each other, $y_j = a_j y$, with a_j constant and y a fiducial y_j, such as that corresponding to H. (This assumption is implicit in the treatment of Shull and McKee 1979.) Equation (A4) then becomes

$$\frac{dn_j}{dy} = a_{j-1}\eta_{j-1} n_{j-1} - a_j n_j , \tag{A6}$$

which is readily integrated.

For the case at hand, H_2 can be photoionized by fewer photons than H because of its higher threshold, but its cross section is generally higher. To obtain an analytic solution we therefore assume that $y(H_2) = y(H)$, so that $a_1 = a_2 = 1$, where we identify $j = 1$

for H_2, $j = 2$ for H, and $j = 3$ for H^+. Recalling that $\eta_1 = 2$ and $\eta_2 = 1$, we then find the concentrations $x_j = n_j/n$ from equation (A6):

$$x(H_2) = 0.5e^{-y}, \qquad x(H) = ye^{-y}, \qquad x(H^+) = 1 - (y + 1)e^{-y}. \tag{A7}$$

Far ahead of the shock, $y \to 0$ and the gas is entirely molecular. The concentrations at the shock front depend on y_s, the value of y at the shock front, which must be found from the equation of radiative transfer. Let F_H^* be the total photon flux above the ionization edge of the atomic hydrogen, and let $\kappa_\nu = n(H_2)\sigma_{H_2}(\nu) + n(H)\sigma_H(\nu)$ be the continuum opacity (we neglect helium for simplicity). Then the equation of transfer implies

$$\frac{dF_H^*}{v_s\,dt} = 4\pi \int_0^\infty \kappa_\nu J_\nu^*\,d\nu = n(H_2)\dot{y}_{H_2} + n(H)\dot{y}_H . \tag{A8}$$

Each photodissociation of H_2 makes 2 H's, so that it requires 0.5 photons per H. It requires one additional photon to make H^+, for a total of 1.5 photons per H^+. Hence, we conclude

$$\frac{dF_H^*}{v_s\,dt} = \frac{d}{dt}\,[0.5n(H) + 1.5n(H^+)] , \tag{A9}$$

as may be verified directly from equations (A4) and (A8). Define

$$\Phi_H = \left.\frac{F_H^*}{n_0 v_s}\right|_{\text{shockfront}} \tag{A10}$$

as the ionizing flux per hydrogen nucleus. The integral of equation (A9) together with equation (A7) then yields

$$\Phi_H = 1.5 - (1.5 + y_s)e^{-y_s} . \tag{A11}$$

Equations (A7) and (A11) determine the hydrogen composition of the gas entering the shock front once the ionizing flux Φ_H is known. An approximate solution of these equations, accurate to within 5% for $x_j > 0.01$ and $\Phi_H < 1.5$, is

$$x(H_2) \simeq \frac{(3 - 2\Phi_H)[1 + (1/3)\Phi_H(1 - \Phi_H)]}{2(3 + 4\Phi_H)} , \tag{A12a}$$

$$x(H) \simeq \frac{2\Phi_H(3 - 2\Phi_H)[1 - (1/4)\Phi_H(1 - \Phi_H)]}{3 + 4\Phi_H} , \tag{A12b}$$

$$x(H^+) \simeq \frac{16\Phi_H^2}{9(1 + 2\Phi_H)} . \tag{A12c}$$

Trace amounts of H_3^+ (up to several percent) and H_2^+ are also present. Since it takes 1.5 photons to form each H^+, the precursor becomes fully ionized for $\Phi_H > 1.5$. The analogous criterion for atomic shocks (again neglecting helium) is $\Phi_H > 1$ (Shull and McKee 1979). Helium can absorb some of the ionizing photons, so in a cosmic plasma the threshold values of Φ_H are increased by a small amount, to ~ 1.6 and 1.1 for molecular and atomic shocks, respectively. Based on the results of Seab *et al.* (1989), we estimate that the critical velocity for full preionization of hydrogen is increased from about 110 km s^{-1} for shocks in atomic gas to somewhat over 120 km s^{-1} for shocks in molecular gas.

It is convenient to have an analytic approximation for $\Phi_H(v_s)$. The values of Φ_H for atomic shocks (Seab *et al.* 1989) can be converted to values for molecular shocks using the concept of the "equivalent atomic shock" introduced by McKee and Hollenbach (1987): because of the energy lost in dissociating H_2 behind the shock front, a shock in molecular gas velocity v_s produces the same ionizing radiation as an atomic shock at the lower velocity

$$v_{eq} = [v_s^2 - 2x_{2s}(17.5 \text{ km s}^{-1})^2]^{0.5} , \tag{A13}$$

where x_{2s} is the H_2 concentration just ahead of the shock front. With $\Phi_H(v_{eq})$ from Seab *et al.* (1989) and x_{2s} from equation (A12a), we find that

$$\Phi_H(v_s) = 2.35H(v_{s7} - 0.76)\exp - \left(\frac{0.50}{v_{s7}^2 - 0.57}\right) + 0.90v_{s7}^2 \exp - \left(\frac{1.67}{v_{s7}^{1.5}}\right) \tag{A14}$$

is accurate to within $\sim 10\%$ for $0.4 \leq v_{s7} \leq 1.3$, where $H(x)$ is the step function.

The composition of the precursor at the shock front is displayed in Figure 11. This figure is based on equations (A12) and (A14), except that the point of full preionization ($\Phi_H = 1.5$) has been adjusted to $v_s = 120$ km s^{-1} (Seab *et al.* 1989) rather than the 115 km s^{-1} value given by equation (A14). The molecular concentration is reduced by at least 10% for $v_s \gtrsim 80$ km s^{-1}, and the H^+ concentration exceeds 10% for $v_s \gtrsim 90$ km s^{-1}.

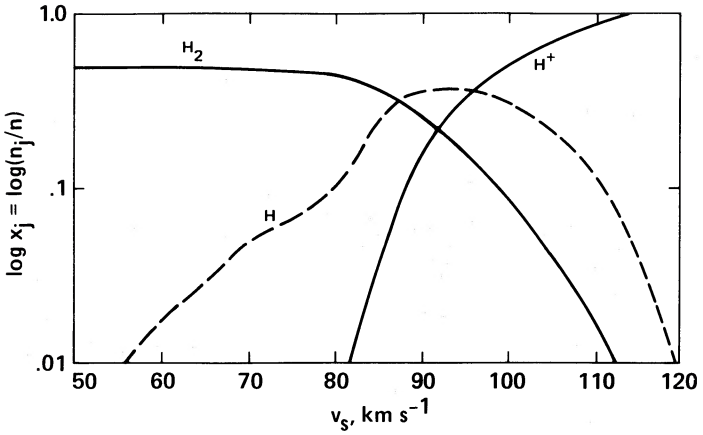

FIG. 11.—The relative number abundances of H_2, H, and H^+ in the preshock gas just upstream from the shock front are plotted as a function of v_s. The radiation field from the shock dissociates the ambient molecular gas for $v_s \gtrsim 90$ km s^{-1} and ionizes it for $v_s \gtrsim 120$ km s^{-1}.

APPENDIX B

CHEMISTRY

I. PARTICLE-PARTICLE REACTIONS

The rate coefficients for neutral-neutral, ion-neutral, and electronic reactions are given in Tables 3–5. The rate coefficients γ are taken to be

$$\gamma = A\left(\frac{T}{300\ \mathrm{K}}\right)^B e^{-C/T}\ \mathrm{cm^3\ s^{-1}}\ . \tag{B1}$$

Table 5 includes recombination of electrons with atomic ions. We apply a three-body recombination factor to the starred reactions given by

$$f_{\mathrm{tb}} = 1 + \frac{100 n_e^{0.5}}{T^2}\ , \tag{B2}$$

with n_e the electron density in cm^{-3} and T in degrees K (fitted from Bates *et al.* 1962). Table 5 also lists the endothermic reactions initiated by electrons to which we apply the non-Maxwellian factor discussed in § II*c*(iv) of the text.

A small number of reaction rate coefficients have a form more complicated than that given in equation (B1). These include the on-the-spot approximation to He^+ recombination

$$He^+ + e \rightarrow\ \rightarrow He + h\nu$$

whose rate coefficient is taken to be

$$\gamma = 8.9 \times 10^{-13} T_{300}^{-0.49}\left[\frac{x(\mathrm{H}) + 3x(\mathrm{H_2})}{x(\mathrm{H}) + 3x(\mathrm{H_2}) + 7x(\mathrm{He})}\right] + 2.5 \times 10^{-12} T_{300}^{-0.64}\ \mathrm{cm^3\ s^{-1}}\ , \tag{B3}$$

where $T_{300} = T/300$ K and $x(i)$ is the abundance of species i. The first term in equation (B3) represents recombinations to the ground state whose photons ionized H or H_2, and the second term represents recombinations to excited electronic states (Osterbrock 1974). In addition, we incorporate the non-LTE effects discussed by Wagner and Graff (1987) for the reaction

$$O + H_2 \rightarrow OH + H$$

by taking as its rate coefficient

$$\gamma = 3.7 \times 10^{-12} c_f T_{300}^{1.53} \exp(-4060/T) + 2.32 \times 10^{-12}(1 - c_f) T_{300}^{1.93} \exp(-3940/T)\ \mathrm{cm^3\ s^{-1}}\ , \tag{B4}$$

where $c_f = 1/(1 + n_{\mathrm{cr}}/n)$ is the abundance of H_2 in excited vibrational states relative to the LTE value and we take n_{cr} to be

$$n_{\mathrm{cr}} = \frac{10^6 T^{0.5}}{3.2x(\mathrm{H}) \exp[-(400/T)^2] + 2.8x(\mathrm{H_2}) \exp[-18100/(T + 1200)]}\ \mathrm{cm^{-3}}\ . \tag{B5}$$

We have fitted a simple analytic expression to recent data (see discussion in Draine and Katz 1986) on the important reaction

$$H + CH^+ \rightarrow H^+ + H_2$$

taking

$$\gamma = 2 \times 10^{-10} + \frac{10^{-9}}{1 + T_{300}}\ \mathrm{cm^3\ s^{-1}}\ . \tag{B6}$$

TABLE 3

NEUTRAL-NEUTRAL REACTIONS

Reaction (1)	A[a] (2)	B[a] (3)	C[a] (4)	Reference (5)
$H + H \rightarrow H^+ + H + e$	1.70(−13)	5.00(−1)	1.58(5)	1
$H + H \rightarrow H^+ + H + e$[b]	3.00(−13)	5.00(−1)	1.49(5)	2
$He + H \rightarrow He^+ + H + e$	8.63(−14)	4.30(−1)	2.85(5)	1
$He + H_2 \rightarrow He^+ + H_2 + e$	8.63(−14)	4.30(−1)	2.85(5)	1
$C + H \rightarrow C^+ + H + e$	5.90(−13)	4.00(−1)	1.31(5)	1
$C + H_2 \rightarrow C^+ + H_2 + e$	5.90(−13)	4.00(−1)	1.31(5)	1
$C + H_2 \rightarrow CH + H$	4.50(−11)	5.00(−1)	1.56(4)	3
$C + OH \rightarrow CO + H$	1.11(−10)	5.00(−1)	...	4
$C + H_2O \rightarrow CH + OH$	1.43(−10)	5.00(−1)	2.40(4)	5
$C + O_2 \rightarrow CO + O$	1.80(−11)	5.00(−1)	...	5
$O + H \rightarrow O^+ + H + e$	3.04(−13)	4.90(−1)	1.58(5)	1
$O + H_2 \rightarrow O^+ + H_2 + e$	3.04(−13)	4.90(−1)	1.58(5)	1
$O + CH \rightarrow CO + H$	9.53(−11)	5.00(−1)	...	3
$O + CH \rightarrow C + OH$	1.73(−11)	5.00(−1)	4.00(3)	3
$O + CH_4 \rightarrow CH_3 + OH$	3.50(−11)	...	4.55(3)	5
$O + OH \rightarrow O_2 + H$	4.33(−11)	−5.00(−1)	3.00(1)	6
$O + H_2O \rightarrow OH + OH$	1.35(−12)	1.75	7.86(3)	6
$O + CO \rightarrow C + O_2$	2.90(−11)	5.00(−1)	6.93(4)	5
$CH + H \rightarrow C + H_2$	1.80(−11)	5.00(−1)	4.00(3)	3
$CH + H \rightarrow CH^+ + H + e$	8.83(−14)	5.00(−1)	1.29(5)	estimate, 1
$CH + H_2 \rightarrow CH_2 + H$	3.60(−10)	...	3.90(3)	5
$CH + H_2 \rightarrow CH^+ + H_2 + e$	8.83(−14)	5.00(−1)	1.29(5)	estimate, 1
$CH + OH \rightarrow H_2O + C$	1.00(−10)	...	...	estimate, 1
$CH_2 + H \rightarrow CH + H_2$	3.60(−10)	...	2.65(3)	5
$CH_2 + H_2 \rightarrow CH_3 + H$	5.30(−12)	...	3.53(3)	5
$CH_3 + H \rightarrow CH_2 + H_2$	5.30(−12)	...	1.08(4)	5
$CH_3 + H_2 \rightarrow CH_4 + H$	1.40(−12)	...	5.50(3)	5
$CH_4 + H \rightarrow CH_3 + H_2$	1.00(−10)	...	5.99(3)	5
$CH_4 + OH \rightarrow CH_3 + H_2O$	2.40(−12)	...	1.71(3)	5
$OH + H \rightarrow O + H_2$	6.60(−13)	1.53	2.97(3)	6
$OH + H \rightarrow OH^+ + H + e$	8.83(−14)	5.00(−1)	1.53(5)	estimate, 1
$OH + H_2 \rightarrow H_2O + H$	8.80(−13)	1.95	1.42(3)	6
$OH + H_2 \rightarrow OH^+ + H_2 + e$	8.83(−14)	5.00(−1)	1.53(5)	estimate, 1
$OH + OH \rightarrow H_2O + O$	4.20(−12)	...	2.42(2)	5
$H_2O + H \rightarrow OH + H_2$	7.44(−12)	1.57	9.14(3)	6
$H_2O + H \rightarrow H_2O^+ + H + e$	7.55(−14)	4.50(−1)	1.47(5)	estimate, 1
$H_2O + H_2 \rightarrow H_2O^+ + H_2 + e$	7.55(−14)	4.50(−1)	1.47(5)	estimate, 1
$CO + H \rightarrow C + OH$	1.11(−10)	5.00(−1)	7.77(4)	4
$CO + H \rightarrow CH + O$	9.53(−11)	5.00(−1)	8.83(4)	3
$CO + H \rightarrow CO^+ + H + e$	1.13(−13)	6.00(−1)	1.63(5)	estimate, 1
$CO + H_2 \rightarrow CO^+ + H_2 + e$	1.13(−13)	6.00(−1)	1.63(5)	estimate, 1
$O_2 + H \rightarrow OH + O$	1.63(−09)	−9.00(−1)	8.75(3)	6
$O_2 + H \rightarrow O_2^+ + H + e$	2.37(−15)	1.04	1.40(5)	estimate, 1
$O_2 + H_2 \rightarrow O_2^+ + H_2 + e$	2.37(−15)	1.04	1.40(5)	estimate, 1
$Si + OH \rightarrow SiO + H$	2.00(−11)	...	...	4

[a] The reaction rate coefficients have the form $A(T/300\ \mathrm{K})^B e^{-C/T}\ \mathrm{cm^3\ s^{-1}}$. A blank in cols. (3) and (4) indicates a value of zero.

[b] The intermediate step in this reaction is the formation of $H^+ + H^-$; H^- is assumed to promptly go to $H + e$.

REFERENCES.—(1) HM79; (2) GvZ87; (3)DK86; (4)PH80; (5)P86; (6)WG87.

DRD's expression is used for the rate coefficient of the reaction

$$H + H_2 \rightarrow H^- + H_2^+$$

$$\gamma = 10^{-15} T_{300}^{1.5}(1 + 5.3 \times 10^{-3} T_{300}) \exp(-1.7 \times 10^5/T)\ \mathrm{cm^3\ s^{-1}}\ . \quad \text{(B7)}$$

and we assume that the H^- immediately photodissociates to $H + e$. Similarly, the second reaction in Table 3 has the products $H^+ + H^-$, but we assume that H^- dissociates to $H + e$. We have fitted analytic expressions to the cross sectional data (Fleischmann and Young 1969; Peterson and Eisner 1973) for the collisional ionization of H and H_2 by collisions with H and H_2

$$H + H_2 \rightarrow H_2^+ + H + e$$

$$\gamma = 5.29 \times 10^{-19} T^{1.3} R[(1.789 \times 10^5/T), 0.80]\ \mathrm{cm^3\ s^{-1}} \quad \text{(B8)}$$

$$H + H_2 \rightarrow H^+ + H_2 + e$$

$$\gamma = 5.29 \times 10^{-19} T^{1.3} R[(1.577 \times 10^5/T), 0.80]\ \mathrm{cm^3\ s^{-1}} \quad \text{(B9)}$$

$$H_2 + H_2 \rightarrow H_2^+ + H_2 + e$$

$$\gamma = 2.39 \times 10^{-26} T^{2.54} R[(1.789 \times 10^5/T), 2.04]\ \mathrm{cm^3\ s^{-1}} \quad \text{(B10)}$$

TABLE 4

ION-NEUTRAL REACTIONS

Reaction	A	B	C	Reference
$D + H^+ \rightarrow H + D^+$	2.00(−09)	...	4.30(1)	1
$He + H^+ \rightarrow He^+ + H^+ + e$	8.63(−14)	4.30(−1)	2.85(5)	estimate, 2
$C + H^+ \rightarrow C^+ + H^+ + e$	5.90(−13)	4.00(−1)	1.31(5)	estimate, 2
$CH + H^+ \rightarrow CH^+ + H^+ + e$	8.83(−14)	5.00(−1)	1.29(5)	estimate, 2
$O + H^+ \rightarrow H + O^+$	7.00(−10)	...	2.32(2)	3
$O + H^+ \rightarrow O^+ + H^+ + e$	3.04(−13)	4.90(−1)	1.58(5)	estimate, 2
$H_2 + H^+ \rightarrow H + H_2^+$	6.40(−10)	...	2.13(4)	4
$HD + H^+ \rightarrow H_2 + D^+$	3.00(−10)	...	4.59(2)	3
$HD + H^+ \rightarrow H_2 + D^+$	9.00(−10)	...	6.29(2)	3
$CH + H^+ \rightarrow H + CH^+$	1.90(−09)	...	...	5
$OH + H^+ \rightarrow H + OH^+$	2.10(−10)	...	...	5
$OH + H^+ \rightarrow OH^+ + H^+ + e$	8.83(−14)	5.00(−1)	1.53(5)	estimate, 2
$H_2O + H^+ \rightarrow H + H_2O^+$	8.20(−09)	...	...	5
$H_2O + H^+ \rightarrow H_2O^+ + H^+ + e$	7.55(−14)	4.50(−1)	1.47(5)	estimate, 2
$CO + H^+ \rightarrow H + CO^+$	1.90(−10)	...	4.66(3)	5
$CO + H^+ \rightarrow CO^+ + H^+ + e$	1.13(−13)	6.00(−1)	1.63(5)	estimate, 2
$O_2 + H^+ \rightarrow H + O_2^+$	1.20(−09)	...	...	5
$O_2 + H^+ \rightarrow O_2^+ + H^+ + e$	2.37(−15)	1.04	1.40(5)	estimate, 2
$H + D^+ \rightarrow D + H^+$	2.00(−09)	...	...	1
$H_2 + D^+ \rightarrow HD + H^+$	2.00(−09)	...	...	4
$H + He^+ \rightarrow He + H^+$	1.90(−15)	...	...	5
$H_2 + He^+ \rightarrow H + H^+ + He$	1.10(−13)	...	...	3
$H_2O + He^+ \rightarrow H + OH^+ + He$	2.86(−10)	...	...	4
$H_2O + He^+ \rightarrow OH + H^+ + He$	2.03(−10)	...	...	4
$H_2O + He^+ \rightarrow He + H_2O^+$	6.05(−11)	...	...	4
$CO + He^+ \rightarrow O + C^+ + He$	1.70(−09)	...	...	4
$O_2 + He^+ \rightarrow O + O^+ + He$	1.10(−09)	...	...	3
$H_2 + C^+ \rightarrow CH_2^+$	4.00(−16)	−2.00(−1)	...	6
$H_2 + C^+ \rightarrow H + CH^+$	2.00(−10)	...	4.64(3)	7
$OH + C^+ \rightarrow H + CO^+$	7.70(−10)	...	...	5
$H_2O + C^+ \rightarrow H_2 + CO^+$	2.70(−09)	...	...	3
$O_2 + C^+ \rightarrow O + CO^+$	3.76(−10)	...	...	3
$O_2 + C^+ \rightarrow CO + O^+$	6.14(−10)	...	...	3
$SiO + C^+ \rightarrow CO + Si^+$	5.40(−10)	...	...	5
$SiO + C^+ \rightarrow C + SiO^+$	5.40(−10)	...	...	5
$H + O^+ \rightarrow O + H^+$	7.00(−10)	...	...	3
$H_2 + O^+ \rightarrow H + OH^+$	1.60(−09)	...	...	5
$OH + Si^+ \rightarrow H + SiO^+$	6.30(−10)	...	...	5
$H_2O + Si^+ \rightarrow H + SiOH^+$	2.30(−10)	...	...	3
$O_2 + Si^+ \rightarrow O + SiO^+$	9.20(−11)	...	4.03(3)	8
$H + H_2^+ \rightarrow H_2 + H^+$	1.00(−10)	...	...	5
$O + H_2^+ \rightarrow H + OH^+$	1.50(−09)	...	...	5
$H_2 + H_2^+ \rightarrow H + H_3^+$	2.10(−09)	...	...	5
$H_2 + H_2^+ \rightarrow H_2 + H^+ + H$	4.17(−11)	5.00(−1)	3.07(4)	9
$OH + H_2^+ \rightarrow H_2 + OH^+$	7.60(−10)	...	...	5
$H_2O + H_2^+ \rightarrow H_2 + H_2O^+$	3.90(−09)	...	...	5
$H_2O + H_2^+ \rightarrow H + H_3O^+$	3.40(−09)	...	...	5
$O_2 + H_2^+ \rightarrow O_2^+ + H_2$	2.70(−09)	...	...	5
$CO + H_2^+ \rightarrow H_2 + CO^+$	2.80(−09)	...	...	5
$H + H_3^+ \rightarrow H_2 + H_2^+$	2.08(−09)	...	1.88(4)	4
$H_2 + H_3^+ \rightarrow H_2 + H_2^+ + H$	3.41(−11)	5.00(−1)	7.16(4)	estimate, 9
$H_2 + H_3^+ \rightarrow H_2 + H^+ + H_2$	3.41(−11)	5.00(−1)	5.04(4)	estimate, 9
$O + H_3^+ \rightarrow H_2 + OH^+$	8.00(−10)	...	...	5
$OH + H_3^+ \rightarrow H_2 + H_2O^+$	1.30(−09)	...	...	5
$H_2O + H_3^+ \rightarrow H_2 + H_3O^+$	5.90(−09)	...	...	5
$CO + H_3^+ \rightarrow H_2 + CO^+$	1.70(−09)	...	...	5
$C + H_3^+ \rightarrow H_2 + CH^+$	2.00(−09)	...	...	5
$H + OH^+ \rightarrow OH + H^+$	2.10(−09)	...	2.80(3)	5
$H + OH^+ \rightarrow O + H_2^+$	1.60(−09)	...	2.26(4)	5
$H + OH^+ \rightarrow H_2 + O^+$	4.90(−10)	−3.00(−2)	1.97(3)	10
$H_2 + OH^+ \rightarrow OH + H_2^+$	7.60(−10)	...	2.36(4)	5
$H_2 + OH^+ \rightarrow O + H_3^+$	8.00(−10)	...	2.90(3)	5
$H_2 + OH^+ \rightarrow H + H_2O^+$	1.10(−09)	...	...	5
$H + H_2O^+ \rightarrow H_2 + OH^+$	1.70(−09)	2.90(−1)	1.40(4)	10
$H + H_2O^+ \rightarrow H_2O + H^+$	8.20(−09)	...	1.15(4)	5
$H + H_2O^+ \rightarrow OH + H_2^+$	7.60(−10)	...	4.00(4)	5
$H_2 + H_2O^+ \rightarrow OH + H_3^+$	1.30(−09)	...	2.03(4)	5
$H_2 + H_2O^+ \rightarrow H_2O + H_2^+$	3.90(−09)	...	3.27(4)	5
$H_2 + H_2O^+ \rightarrow H + H_3O^+$	6.10(−10)	...	...	10
$H + H_3O^+ \rightarrow H_2 + H_2O^+$	6.00(−09)	3.90(−1)	1.98(4)	5
$H + H_3O^+ \rightarrow H_2O + H_2^+$	3.40(−09)	...	5.25(4)	5
$H_2 + H_3O^+ \rightarrow H_2O + H_3^+$	5.90(−09)	...	3.28(4)	5

TABLE 4—*Continued*

Reaction	*A*	*B*	*C*	Reference
$H + CH^+ \rightarrow H_2 + C^+$	6.00(−10)	−2.50(−1)	...	7
$H_2 + CH^+ \rightarrow H + CH_2^+$	1.00(−09)	...	...	5
$H + CH_2^+ \rightarrow H_2 + CH^+$	1.00(−09)	...	1.20(4)	5
$H_2 + CH_2^+ \rightarrow CH + H_3^+$	1.20(−09)	...	4.22(4)	5
$O + CH_2^+ \rightarrow H + CO^+$	7.50(−10)	...	...	5
$H + CO^+ \rightarrow CO + H^+$	1.90(−10)	...	...	5
$H + O_2^+ \rightarrow O_2 + H^+$	2.80(−10)	−4.00(−2)	1.78(4)	10
$H_2 + SiO^+ \rightarrow H + SiOH^+$	3.20(−10)	...	...	3

REFERENCES.—(1) BD73; (2) HM79; (3) AH86; (4) P86; (5) PH80; (6) H85; (7) DK86; (8) FFFV81; (9) VB66; (10) SZ75.

TABLE 5

ELECTRON REACTIONS

Reaction	*A*	*B*	*C*	Reference
$e + H^+ \rightarrow H$	3.60(−12)[a]	−7.50(−1)	...	1
$e + He^+ \rightarrow He$	(see text)	...	...	...
$e + C^+ \rightarrow C$	1.80(−12)[a]	−6.20(−1)	...	1
$e + O^+ \rightarrow O$	1.80(−12)[a]	−6.20(−1)	...	1
$e + Si^+ \rightarrow Si$	4.87(−12)[a]	−6.01(−1)	...	1
$e + H_2^+ \rightarrow H + H$	8.00(−08)	−5.00(−1)	...	2
$e + H_3^+ \rightarrow H_2 + H$	5.00(−09)	−5.00(−1)	...	3
$e + H_3^+ \rightarrow H + H + H$	5.00(−09)	−5.00(−1)	...	3
$e + OH^+ \rightarrow O + H$	2.00(−07)	−5.00(−1)	...	4
$e + H_2O^+ \rightarrow OH + H$	2.00(−07)	−5.00(−1)	...	4
$e + H_2O^+ \rightarrow O + H_2$	2.00(−07)	−5.00(−1)	...	4
$e + H_3O^+ \rightarrow H_2O + H$	1.00(−06)	−5.00(−1)	...	5
$e + H_3O^+ \rightarrow OH + H_3$	3.00(−07)	−5.00(−1)	...	5
$e + O_2^+ \rightarrow O + O$	2.00(−07)	−5.00(−1)	...	4
$e + CO^+ \rightarrow C + O$	1.80(−07)	−5.00(−1)	...	4
$e + CH^+ \rightarrow C + H$	3.00(−07)	−4.00(−1)	...	6
$e + CH_2^+ \rightarrow C + H_2$	2.50(−07)	−5.00(−1)	...	6
$e + CH_2^+ \rightarrow CH + H$	2.50(−07)	−5.00(−1)	...	6
$e + SiO^+ \rightarrow SI + O$	1.96(−07)	−5.00(−1)	...	4
$e + SiOH^+ \rightarrow Si + OH$	1.45(−07)	−5.00(−1)	...	estimate
$e + SiOH^+ \rightarrow SiO + H$	1.45(−07)	−5.00(−1)	...	estimate
$e + H \rightarrow H^+ + e + e$	1.00(−09)[b]	5.00(−1)	1.58(5)	7
$e + H_2 \rightarrow H_2^+ + e + e$	6.80(−11)[b]	3.70(−1)	1.81(5)	8
$e + H_2 \rightarrow H + H + e$	3.20(−09)[b]	3.50(−1)	1.02(5)	9
$e + HD \rightarrow H + D + e$	3.20(−09)[b]	3.50(−1)	1.02(5)	9
$e + He \rightarrow He^+ + e + e$	5.10(−10)[b]	4.30(−1)	2.85(5)	7
$e + O \rightarrow O^+ + e + e$	1.79(−09)[b]	4.90(−1)	1.58(5)	7
$e + C \rightarrow C^+ + e + e$	3.40(−09)[b]	4.00(−1)	1.31(5)	7
$e + OH \rightarrow OH^+ + e + e$	5.20(−10)[b]	5.00(−1)	1.50(5)	estimate
$e + H_2O \rightarrow H + OH + e$	9.20(−09)[b]	−5.00(−1)	6.96(4)	10
$e + H_2O \rightarrow H_2O^+ + e + e$	4.40(−10)[b]	4.50(−1)	1.47(5)	11
$e + O_2 \rightarrow O + O + e$	2.30(−09)[b]	−5.00(−1)	6.96(4)	10
$e + O_2 \rightarrow O_2^+ + e + e$	1.40(−11)[b]	1.04	1.40(5)	12
$e + CH \rightarrow CH^+ + e + e$	5.20(−10)[b]	5.00(−1)	1.50(5)	estimate
$e + CO \rightarrow CO^+ + e + e$	6.70(−10)[b]	6.00(−1)	1.63(5)	8
$e + CO \rightarrow C + O + e$	8.10(−10)[b]	−5.00(−1)	1.14(5)	10

[a] These reactions have the three-body recombination factor f_{tb} applied to them.

[b] These reactions have the non-Maxwellian factor discussed in text applied to them.

REFERENCES.—(1) AP73, (2) H87; (3) SA84; (4) PH80; (5) B86; (6) DK86; (7) HM79; (8) REG65; (9) C65; (10) K69; (11) ME76; (12) M75.

where the function $R(a, b)$ is given

$$R(a, b) = (r - a)^b r e^{-r} \left(\frac{\pi}{2\phi_d}\right)^{0.5} \{1 - \text{erf}\,[(0.5\phi_d)^{0.5}(r - a)]\}\,, \tag{B11}$$

and where

$$r = 0.5[y + (y^2 - 4a)^{0.5}]\,, \tag{B12}$$

$$y = 1 + a + b\,, \tag{B13}$$

$$\phi_d = b/(r - a)^2 + r^{-2}\,. \tag{B14}$$

TABLE 6

COSMIC RAY IONIZATION

Reaction	Rate
$H + cr \rightarrow H^+ + e$	0.46ζ
$He + cr \rightarrow He^+ + e$	0.50ζ
$H_2 + cr \rightarrow H_2^+ + e$	0.93ζ
$H_2 + cr \rightarrow H + H$	0.10ζ
$H_2 + cr \rightarrow H + H^+ + e$ ...	0.022ζ

ζ is taken to be 4×10^{-17} s^{-1}, after VDB86. Relative rates are from PH80.

In addition, we have included a number of reactions with complicated rate coefficients which treat the dissociation of molecules by rapidly drifting grains, the ionization of hydrogen by collisions with "hot" neutrals which are produced in collisions with drifting grains, and the ionization of hydrogen by collisions with ions. These processes are important for *C* shocks, but have no effect on *J* shocks, where the grain drift speeds are small and where the electronic ionization dominates the ionization by ions. These reactions will be discussed in a future paper which compares *C* shock spectra with *J* shock spectra (Chernoff, Hollenbach, and McKee 1989).

There are several "pseudo-reactions" in Table 4; these are reactions which have the proper rates but slightly altered products chosen to close the chemical matrix while preserving the essential chemistry and the approximate ion mass for the *C* shock calculations. The reactions include $O_2 + H_2^+$, $CO + H_3^+$, $D + H_2^+$, $CO + H_3^+$, and $C^+ + H_2O$. These reactions in fact produce some O_2H^+, HCO^+, and HD^+ which are not included as species in our code, but we assume instead as products O_2^+, CO^+, and H^+, respectively. Note also in Table 4 that we have assumed that the collisional ionization of neutrals by H^+ proceeds with the same rate coefficients as those for the corresponding ionizations by H. This may underestimate the ionization caused by H^+. However, the uncertain H^+ rates are certainly smaller than the corresponding electronic rates in *J* shocks, so that this uncertainty does not affect our results.

Cosmic-ray ionization has been included with the rates given in Table 6. Although of major importance to the chemistry of cold, opaque molecular gas, cosmic-ray ionization is of little significance to postshock chemistry because of its relatively long time scale ($\sim 10^6$ yr) to appreciably affect the chemistry and because it is dwarfed by high-temperature chemistry and photochemistry in the warm postshock gas.

II. GAS-GRAIN CHEMISTRY

The text discusses the formation of H_2 on grain surfaces. Another important grain process is the recombination of ions on grains in regions of low electron fraction ($\lesssim 10^{-2}$). We include the grain recombination of all the ionic species in the code, using the analytic rate coefficient of Draine and Sutin (1987) for a MRN distribution of grain sizes

$$\alpha = 1.3 \times 10^{-13}\left(\frac{a_{\min}}{3\ \text{Å}}\right)^{-1.5}\left(\frac{20\ \text{K}}{T}\right)^{0.5}\left(\frac{25 m_{\rm H}}{m_i}\right)^{0.5}\left[1 + 2.2 \times 10^{-3}\left(\frac{a_{\min}}{3\ \text{Å}}\right)\left(\frac{T}{20\ \text{K}}\right)\right] f_A\ \text{cm}^3\ \text{s}^{-1}\ , \tag{B15}$$

where ($m_{\rm H}$, m_i) is the (hydrogen, ion mass) and f_A is given by

$$f_A = \left(\frac{f_{\rm gr}}{5 \times 10^{-3}}\right)\left(\frac{2\ \text{g cm}^{-3}}{\rho_{\rm gr}}\right). \tag{B16}$$

Here, f_A (normalized to unity for standard grain abundances and properties) expresses the change in grain area due to variations in the fraction of dust to gas mass $f_{\rm gr}$ and in the material density of the grain material $\rho_{\rm gr}$. Note that this recombination coefficient gives the recombination rate per unit volume when multiplied by the ion density and the hydrogen nucleus density n (i.e., not the electron or grain number density).

III. PHOTOCHEMISTRY

Table 7 gives an updated version from HM79 of the FUV photodissociation and photoionization cross sections used in the code. The photoionization of hydrogen and helium by the Lyman continuum photons produced in the shock is treated as in HM79. The

TABLE 7

FUV PHOTOIONIZATION AND PHOTODISSOCIATION

Reaction	σ(4.14–11.26 eV)	σ(Lyα)	σ(11.26–13.6 eV)	Reference
$C + h\nu \rightarrow C^+ + e$	...	...	1.60(−17)	1
$Si + h\nu \rightarrow Si^+ + e$	1.70(−17)	2.80(−17)	1.40(−17)	2
$H_2 + h\nu \rightarrow H + H$	...	...	2.00(−21)	2
$HD + h\nu \rightarrow H + D$	...	...	2.00(−21)	2
$OH + h\nu \rightarrow O + H$	1.00(−18)	2.00(−18)	3.00(−19)	3
$OH + h\nu \rightarrow OH^+ + e$ ..	...	...	2.00(−18)	3
$H_2O + h\nu \rightarrow OH + H$ ..	1.00(−18)	7.40(−18)	1.00(−17)	4
$O_2 + h\nu \rightarrow O + O$	3.00(−18)	1.50(−18)	2.00(−18)	2
$CH + h\nu \rightarrow C + H$	7.00(−19)	7.00(−19)	2.00(−17)	2
$SiO + h\nu \rightarrow SiO^+ + e$ ..	...	...	1.00(−17)	estimate

REFERENCES.—(1) BT79; (2) HM79; (3) VDD83; (4) L84.

photochemistry in the precursor gas is treated as in Shull and McKee (1979), with the exception that only one iteration is performed.

The H_2, HD, and CO photodissociations are primarily accomplished via the line absorption of FUV radiation. These important photodissociations unfortunately cannot be treated very accurately since much of the FUV radiation is itself line radiation so that line coincidences may play an important role. The high postshock temperatures, which populate many rotational and vibrational states of these molecules, increases the prospects for such overlaps. In addition, the H_2 line absorptions help to shield the CO from photodissociation, because of overlaps of H_2 and CO lines (see, e.g., van Dishoeck 1987). We have chosen to adopt rather simple analytic expressions for the rate of photodissociation of H_2, HD, and CO, as discussed in § II*c*(iii) and HM79.

APPENDIX C

ATOMIC COOLING

Above 10^4 K the atomic cooling in fast shocks is generally dominated by Lyα, and the treatment of atomic hydrogen is discussed in the text. Between 10^4 K and $\sim$5000 K, metastable transitions of the dominant metal species often dominate the cooling, with particularly strong emission from C I λ9849, C II λ2324, Fe II(1.26 μm), N I(1.04 μm), N II $\lambda\lambda$6548, 6584, O I λ6300, and S II $\lambda\lambda$6716, 6731. At very high postshock densities ($n \gtrsim 10^9$ cm^{-3}) the low-lying permitted transitions Fe I λ5110 and Fe II λ2599 become significant. For $T \lesssim 5000$ K, the fine-structure transitions such as O I(63 μm), Si II(35 μm), and C II(158 μm) dominate the atomic contribution to the cooling.

TABLE 8

FINE-STRUCTURE ATOMIC COOLING PARAMETERS

Species (0, 1, 2)[a]	$\frac{E_{ij}}{k}$ (K)[b]	λ_μ[c]	n_{cr}^e (cm^{-3})[d]	n_{cr}^H (cm^{-3})[d]	A_{ij} (s^{-1})[e]	γ_{ij}^e (cm^{-3} s^{-1})[f]	γ_{ij}^H (cm^3 s^{-1})[f]	N_τ (cm^{-2})[g]
C I ($^3P_0$, $^3P_1$, $^3P_2$)	2.4(1)	609.2	$3.9(0)T_2^{-0.13}$	$1.6(2)T_2^{-0.34}$	7.9(−8)	3.0(−9)	$1.6(-10)T_2^{0.14}$	2.3(20)
	6.3(1)	229.9	1.3(1)	$7.0(2)T_2^{-0.26}$	2.0(−14)	5.0(−9)	$9.2(-11)T_2^{0.26}$	9.8(27)
	3.9(1)	369.0	...	...	2.7(−7)	1.5(−8)	$2.9(-10)T_2^{0.26}$	5.3(20)
C II ($^2P_{1/2}$, $^2P_{3/2}$)	9.2(1)	157.7	$8.7(0)T_2^{0.50}$	$3.0(2)T_2^{-0.07}$	2.4(−6)	$2.8(-7)T_2^{-0.5}$	$8.0(-10)T_2^{0.07}$	6.5(20)
Cl I ($^2P_{3/2}$, $^2P_{1/2}$)	1.3(3)	11.4	2.6(5)	$1.4(7)T_2^{-0.17}$	1.2(−2)	4.7(−8)	$8.3(-10)T_2^{0.17}$	1.1(24)
Cl II ($^3P_2$, $^3P_1$, $^3P_0$)	1.0(3)	14.4	$1.4(4)T_2^{0.45}$	5.4(6)	7.5(−3)	$5.3(-7)T_2^{-0.5}$	1.4(−9)	7.5(23)
	1.4(3)	10.0	$1.6(3)T_2^{0.50}$	8.1(5)	4.8(−7)	$5.3(-7)T_2^{-0.5}$	1.1(−9)	1.0(29)
	4.3(2)	33.4	...	...	1.4(−3)	$3.2(-7)T_2^{-0.5}$	6.3(−10)	5.7(23)
Fe I ($^5D_4$, $^5D_3$, $^5D_2$)	6.0(2)	24.0	$2.1(4)T_2^{-0.13}$	$3.1(6)T_2^{-0.28}$	2.5(−3)	1.2(−7)	$8.0(-10)T_2^{0.17}$	6.6(21)
	1.0(3)	14.2	7.5(3)	$1.3(6)T_2^{-0.17}$	1.0(−9)	1.2(−7)	$6.9(-10)T_2^{0.17}$	9.3(26)
	4.2(2)	34.2	...	...	1.6(3)	9.3(−8)	$5.3(-10)T_2^{0.17}$	3.7(21)
Fe II ($^6D_{9/2}$, $^6D_{7/2}$, $^6D_{5/2}$) ..	5.6(2)	26.0	$1.2(3)T_2^{0.41}$	$2.2(6)T_2^{-0.09}$	2.1(−3)	$1.8(-6)T_2^{-0.5}$	9.5(−10)	6.0(21)
	9.6(2)	15.0	$6.0(2)T_2^{0.50}$	1.5(6)	1.5(−9)	$1.8(-6)T_2^{-0.5}$	5.7(−10)	5.9(28)
	4.1(2)	35.4	...	...	1.6(−3)	$8.7(-7)T_2^{-0.5}$	4.7(−10)	3.3(21)
Ne II ($^2P_{3/2}$, $^2P_{1/2}$)	1.1(3)	12.8	$5.4(4)T_2^{0.50}$	6.6(6)	8.6(−3)	$1.6(-7)T_2^{-0.5}$	1.3(−9)	1.9(22)
Ni I ($^3F_4$, $^3F_3$, $^3F_2$)	1.9(3)	7.5	$5.2(5)T_2^{-0.06}$	$7.8(7)T_2^{-0.22}$	6.2(−2)	1.2(−7)	$8.0(-10)T_2^{0.17}$	1.1(23)
	3.2(3)	4.5	1.2(5)	$2.0(7)T_2^{0.17}$	3.6(−9)	1.2(−7)	$6.9(-10)T_2^{0.17}$	1.3(31)
	1.3(3)	11.3	...	...	2.5(−2)	9.3(−8)	$5.3(-10)T_2^{0.17}$	8.9(22)
Ni II ($^2D_{5/2}$, $^2D_{3/2}$)	2.2(3)	6.6	$5.0(4)T_2^{0.50}$	5.0(7)	5.5(−2)	$1.1(-6)T_2^{-0.5}$	1.1(−9)	2.2(23)
O I ($^3P_2$, $^3P_1$, $^3P_0$)	2.3(2)	63.1	$6.3(3)T_2^{-0.03}$	$8.5(5)T_2^{-0.69}$	9.0(−5)	1.4(−8)	$9.2(-11)T_2^{0.67}$	4.9(20)
	3.3(2)	44.2	8.9(2)	$1.1(5)T_2^{-0.57}$	1.0(−10)	1.4(−8)	$4.3(-11)T_2^{0.80}$	3.8(27)
	9.8(1)	145.6	...	...	1.7(−5)	5.0(−9)	$1.1(-10)T_2^{0.44}$	3.7(20)
S I ($^3P_2$, $^3P_1$, $^3P_0$)	5.7(2)	25.2	$4.2(4)T_2^{-0.03}$	$1.8(6)T_2^{-0.22}$	1.4(−3)	3.3(−8)	$7.5(-10)T_2^{0.17}$	2.0(22)
	8.2(2)	17.4	6.7(3)	$2.7(5)T_2^{-0.17}$	7.1(−8)	3.3(−8)	$7.1(-10)T_2^{0.17}$	3.7(27)
	2.5(2)	56.6	...	...	3.0(−4)	1.2(−8)	$4.2(-10)T_2^{0.17}$	1.5(22)
Si I ($^3P_0$, $^3P_1$, $^3P_2$)	1.1(2)	129.6	$7.2(2)T_2^{-0.50}$	$1.9(4)T_2^{-0.47}$	8.4(−6)	7.2(−9)	$3.5(-10)T_2^{-0.03}$	2.3(21)
	3.2(2)	44.8	1.4(3)	$6.3(4)T_2^{-0.17}$	2.4(−10)	7.2(−9)	$1.7(-10)T_2^{0.17}$	2.0(27)
	2.1(2)	68.4	...	...	4.2(−5)	2.2(−8)	$5.0(-10)T_2^{0.17}$	5.6(21)
Si II ($^2P_{1/2}$, $^2P_{3/2}$)	4.1(2)	34.8	$1.2(2)T_2^{0.50}$	3.2(5)	2.1(−4)	$1.7(-6)T_2^{-0.5}$	$8.0(-10)T_2^{-0.07}$	7.1(21)

[a] The levels are arranged as follows: 0 = ground state, 1 = first excited state, and 2 = second excited state.

[b] For three-level systems, the energies listed are E_{10}, E_{20}, and E_{21}, respectively.

[c] The wavelength in microns; note that the 2→0 transition is generally forbidden.

[d] The critical densities (*see text*) are listed to achieve LTE in levels 1 and 2, respectively, $T_2 = T/100$ K. The power law fits for the three level systems are accurate to 30% in the temperature range 30 K < T < 3000 K.

[e] The spontaneous transition rates listed in order A_{10}, A_{20}, and A_{21}. These are taken from Aller (1984), Garstang 1958, 1962, 1964, 1968; Grevesse, Nussbaumer, and Swings 1971; and Wiese *et al.* 1966, 1969.

[f] The rate coefficients for collisional deexcitation are listed in the same order. They are calculated from formulae given by Bahcall and Wolf 1968 with the exceptions C I and O I (Launay and Roueff 1977*a*), C II (Launay and Roueff 1977*b*), Fe II (Aannestad 1973), Ne II (Osterbrock 1974). Proton rates are substituted for electron rates for neutral target atoms.

[g] N_τ is the column density of hydrogen nuclei which provide unit optical depth at line center, assuming solar abundances of the species in the lower state of the transition.

TABLE 9

OTHER FORBIDDEN AND SEMIFORBIDDEN ATOMIC COOLING PARAMETERS

Species (0, 1, 2)[a]	$\frac{E_{ij}}{k}$ (K)[b]	λ[c] (Å)	n_{cr}^{e}[d] (cm^{-3})	n_{cr}^{H}[d] (cm^{-3})	A_{ij}[e] (s^{-1})	$\gamma_{ij}^{e}(T_4 < 1)$[f]	$\gamma_{ij}^{e}(1 < T_4 < 20)$[f]	N_τ[g] (cm^{-2})
C I ($^3P, ^1D, ^1S$)	1.5(4)	9823 9850	$1.1(4)T_4^{-0.58}$	$3.0(8)T_4^{-0.02}$	3.4(−4)	$2.7(-8)T_4^{0.57}$	$2.7(-8)T_4^{-0.13}$	5.4(25)
	3.1(4)	4622	$2.9(7)T_4^{-0.57}$	2.5(11)	2.6(−3)	$1.3(-8)T_4^{0.57}$	1.3(−8)	1.4(26)
	1.7(4)	8727	...	...	0.5	$1.2(-8)T_4^{0.57}$	1.2(−8)	1.8(23)
C II ($^2P, ^4P$)	6.2(4)	2326	$1.6(8)T_4^{0.50}$	3.6(12)	3.6	$2.3(-8)T_4^{-0.50}$	...	1.3(23)
Cl II ($^3P, ^1D, ^1S$)	1.7(4)	8580 9126	$1.9(6)T_4^{0.49}$	$1.3(11)T_4^{-0.01}$	0.13	$6.7(-8)T_4^{-0.50}$	...	2.7(26)
	4.1(4)	3675	$3.7(7)T_4^{0.50}$	1.8(12)	1.3	$3.5(-8)T_4^{-0.50}$	...	4.6(26)
	2.4(4)	6153	...	...	2.3	$6.4(-8)T_4^{-0.50}$	...	9.3(25)
Fe I ($^5D_4, ^5F_5, ^5F_4$)	9.9(3)	1.44 μm	$7.9(3)T_4^{-0.43}$	$1.4(9)T_4^{-0.09}$	2.0(−3)	$2.0(-7)T_4^{0.57}$	$2.0(-7)T_4^{-0.13}$	2.1(25)
	1.1(4)	1.36 μm	$2.6(4)T_4^{-0.16}$	6.6(9)	1.5(−3)	$1.0(-7)T_4^{0.57}$	1.0(−7)	2.1(25)
	6.4(2)	22.3 μm	...	...	3.6(−3)	1.5(−7)	...	4.4(21)
Fe II ($^6D_{9/2}, ^4F_{9/2}, ^4F_{7/2}$) ...	2.7(3)	5.34 μm	$1.0(4)T_4^{0.50}$	$1.6(8)T_4^{-0.11}$	2.8(−4)	$2.2(-8)T_4^{-0.50}$	...	3.5(24)
	3.5(3)	4.12 μm	$1.4(5)T_4^{0.50}$	2.9(9)	1.0(−4)	$7.1(-9)T_4^{-0.50}$	...	2.6(25)
	8.1(2)	17.9 μm	...	...	6.1(−3)	$3.8(-8)T_4^{-0.50}$	...	5.3(21)
Fe II ($^6D_{9/2}, ^4F_{9/2}, ^4D_{7/2}$) ..	2.7(3)	5.34 μm	$6.7(3)T_4^{0.40}$	$1.6(8)T_4^{-0.11}$	2.8(−4)	$2.2(-8)T_4^{-0.50}$	...	3.5(24)
	1.1(4)	1.26 μm	$9.7(4)T_4^{0.50}$	3.7(9)	5.6(−3)	$5.2(-8)T_4^{-0.50}$	...	1.7(25)
	8.6(3)	1.64 μm	...	...	1.9(−3)	$2.5(-8)T_4^{-0.50}$	...	2.2(25)
N I ($^4S, ^2D, ^2P$)	2.8(4)	5198 5201	$2.0(3)T_4^{-0.73}$	$2.0(7)T_4^{-0.06}$	1.1(−5)	$8.0(-9)T_4^{0.57}$	$8.0(-9)T_4^{-0.13}$	2.7(28)
	4.1(4)	3466	$1.9(7)T_4^{-0.57}$	2.6(11)	5.0(−3)	$4.5(-9)T_4^{0.57}$	4.5(−9)	1.2(26)
	1.4(4)	1.04 μm	...	...	7.9(−2)	$2.3(-8)T_4^{0.57}$	2.3(−8)	7.4(23)
N II ($^3P, ^1D, ^1S$)	2.2(4)	6548 6583	$7.8(4)T_4^{0.50}$	$4.0(9)T_4^{-0.01}$	4.1(−3)	$5.2(-8)T_4^{-0.50}$	...	4.6(25)
	4.7(4)	3063	$1.8(7)T_4^{0.50}$	5.7(11)	3.4(−2)	$2.8(-8)T_4^{-0.50}$	...	1.2(26)
	1.5(4)	5755	...	...	1.1	$3.4(-8)T_4^{-0.50}$	...	9.4(23)
Ni I ($^3F_4, ^3D_3, ^3D_2$)	2.9(2)	48.8 μm	$6.0(-4)T_4^{-0.47}$	$4.9(1)T_4^{-0.11}$	8.0(−11)	$7.0(-8)T_4^{0.57}$	$7.0(-8)T_4^{-0.13}$	3.2(29)
	1.3(3)	11.4 μm	$7.0(4)T_4^{-0.10}$	7.0(9)	3.2(−8)	$3.4(-8)T_4^{0.57}$	3.4(−8)	8.7(28)
	9.7(2)	14.8 μm	...	...	7.0(−3)	9.3(−8)	...	1.4(23)
Ni II ($^2D_{5/2}, ^4F_{9/2}, ^4F_{7/2}$) ...	1.2(4)	1.19 μm	$2.9(1)T_4^{0.36}$	$3.2(6)T_4^{-0.15}$	7.5(−6)	$1.1(-7)T_4^{-0.50}$	...	1.5(29)
	1.3(4)	1.07 μm	$1.2(5)T_4^{0.50}$	1.4(10)	1.4(−3)	$1.1(-7)T_4^{-0.50}$	...	2.6(27)
	1.3(3)	10.7 μm	...	...	2.7(−2)	$1.1(-7)T_4^{-0.50}$	...	8.8(22)
O I ($^3P, ^1D, ^1S$)	2.3(4)	6300 6363	$1.3(6)T_4^{-0.58}$	$6.6(9)T_4^{-0.01}$	6.7(−3)	$5.1(-9)T_4^{0.57}$	$5.1(-9)T_4^{0.17}$	9.3(24)
	4.9(4)	2972	$1.8(8)T_4^{-0.57}$	6.9(11)	6.7(−2)	$2.5(-9)T_4^{0.57}$	$2.5(-9)T_4^{0.13}$	1.1(25)
	2.6(4)	5577	...	...	1.3	$5.2(-9)T_4^{0.57}$	$5.2(-9)T_4^{0.15}$	1.5(23)
O II ($^4S, ^2D_{5/2}, ^2D_{3/2}$)	3.9(4)	3729	$1.4(3)T_4^{0.50}$	2.5(7)	5.1(−5)	$1.3(-8)T_4^{-0.50}$	...	2.0(27)
	3.9(4)	3726	$4.7(3)T_4^{0.50}$	9.0(7)	1.7(−4)	$1.3(-8)T_4^{-0.50}$	...	7.1(26)
	3.0(1)	508 μm	...	...	1.3(−7)	$2.5(-8)T_4^{-0.50}$	...	5.6(20)
S I ($^3P, ^1D, ^1S$)	1.3(4)	1.08 μm 1.13 μm	$7.0(5)T_4^{-0.01}$	$3.5(10)T_4^{-0.01}$	3.6(−2)	$5.1(-8)T_4^{0.57}$	$5.1(-8)T_4^{-0.13}$	(3.4(23)
	3.2(4)	4589	$4.5(7)T_4^{-0.57}$	1.1(12)	0.36	$2.5(-8)T_4^{0.57}$	2.5(−8)	5.8(23)
	1.9(4)	7725	...	...	1.8	$2.3(-8)T_4^{0.57}$	2.3(−8)	4.0(22)
S II ($^4S, ^2D_{3/2}, ^2D_{5/2}$)	2.1(4)	6731	$1.1(4)T_4^{0.50}$	7.2(8)	1.8(−3)	$4.9(-8)T_4^{-0.50}$	...	1.2(25)
	2.1(4)	6717	$3.6(3)T_4^{0.50}$	2.4(8)	4.7(−4)	$4.9(-8)T_4^{-0.50}$	...	3.1(25)
	4.5(1)	318 μm	...	...	3.3(−7)	$8.0(-8)T_4^{-0.50}$	...	4.1(20)
Si I ($^3P, ^1D, ^1S$)	9.1(3)	1.62 μm	$5.7(5)T_4^{-0.58}$	$3.4(10)T_4^{-0.02}$	3.6(−2)	$6.2(-8)T_4^{0.57}$	$6.2(-8)T_4^{-0.13}$	1.5(24)
	2.2(4)	6527	$1.4(7)T_4^{-0.57}$	4.0(11)	3.7(−2)	$3.0(-8)T_4^{0.57}$	3.0(−8)	1.1(26)
	1.3(4)	1.1 μm	...	...	0.8	$2.8(-8)T_4^{0.57}$	2.8(−8)	5.9(23)
Si II ($^2P, ^4P$)	6.2(4)	2240	$1.0(11)T_4^{0.50}$	6.8(15)	6.4(3)	$6.5(-8)T_4^{-0.50}$	...	1.5(21)

[a] See footnote *a* of Table 8.

[b] See footnote *b* of Table 8.

[c] The wavelength in angstroms, unless marked as μm (microns).

[d] The critical densities are listed for levels 1 and 2 for three-level systems.

[e] Transition probabilities from Garstang 1958, 1962, 1964, 1968; Wiese *et al.* 1966, 1969; Grevesse *et al.* 1971; Raymond 1979; Nussbaumer and Storey 1980, 1982; and Aller 1984.

[f] Rate coefficients for electron collisions are taken from Bahcall and Wolf 1968; Aller 1984; Osterbrock 1974, Czyzak *et al.* 1968; Raymond 1979; and Henry *et al.* 1969. A blank in the high-temperature column indicates the low temperature rate is also used in this regime. The rate coefficients for atomic hydrogen collisions γ_{ij}^{H} are estimated to be 10^{-12} cm^3 s^{-1} (Federman and Shipsey 1983).

[g] See footnote *g* of Table 8.

The relative strengths of these atomic coolants depends on the temperature, density, and optical depths in the transitions. The temperature dependence is primarily caused by the exp $(-E_u/kT)$ dependence of the upper level of a given transition, where E_u is the energy of the upper level. Thus, the metastable and permitted transitions, which all lie $E_u/k \gtrsim 10^4$ K above ground, play an insignificant role for low ($T \lesssim 5000$ K) temperatures.

The density dependence is best understood in terms of the critical density n_{cr}, which is roughly the density above which the levels collisionally thermalize. We use the standard definition $n_{cr} = A_{ul}/\gamma_{ul}$ for two-level systems, where A_{ul} is the spontaneous radiative rate from u to l and γ_{ul} is the collisional deexcitation rate coefficient. For three-level systems, we take $n_{cr1} = A_{10}/(\gamma_{10} + \gamma_{12})$ and $n_{cr2} = (A_{20} + A_{21})/(\gamma_{20} + \gamma_{21})$ (Osterbrock 1974) and fit a temperature power law to the results for display in Tables 8 and 9.

Tables 8 and 9 give the metastable and fine-structure transitions included in the code, $\Delta E_{ul}/k$, A_{ul}, γ^e_{ul}, γ^H_{ul}, n^e_{cr}, and n^H_{cr}, where e and H refer to electronic collisions and collisions with hydrogen atoms. For the metastable transitions, we have estimated $\gamma^H_{ul} = 10^{-12}$ cm^3 s^{-1}, based on the result for O I λ6300 deexcitation reported by Federman and Shipsey (1983). The rate coefficients for collisions with H_2 are taken to be $\gamma^{H_2}_{ul} = 0.5\gamma^H_{ul}$, based on the ratio of the H_2 to H excitation of the C II fine-structure level (Flower and Launay 1977; Launay and Roueff 1977*a*, *b*). The exceptions to this rule are the rate coefficients for the $J = 1$–0 transitions of C I and O I, which are taken to be $\gamma^{H_2}_{ul} = 0.05\gamma^H_{ul}$, as suggested by Monteiro and Flower (1987). Proton rate coefficients exceed electron rate coefficients for the neutral fine structure transitions. Therefore, in Table 9, we have substituted proton rate coefficients in the γ^e_{ul} column of the neutral species.

For the collisionally excited permitted transitions of H, Fe I, and Fe II, we have neglected collisional deexcitation since the critical densities are extremely high ($\sim 10^{15}$ cm^{-3}) and have assumed each collisional excitation produces a cooling photon. We discuss the treatment of H in the text; we assume the collisional excitation rates for Fe I λ5110 are 10 times the H rates and we take a collision strength of $\Omega = 5.2$ for the electronic excitation of Fe II λ2599 (van Regemorter 1962). Electronic excitation of H I, Fe I, Fe II, and the metastable states of the metals generally dominates neutral excitation because the rate coefficients for electrons $\sim 10^2$–10^4 times those for hydrogen atoms and molecules (see e.g., Drawin 1969) and the ionization fraction usually exceeds 10^{-2}–10^{-4} in the relevant temperature range. On the other hand, in the lower temperature regions where fine-structure transitions dominate the cooling, the ionization fractions are often sufficiently low that neutral hydrogen collisions dominate the excitation. Generally, as the gas cools from 5000 K to 100 K and most of the fine-structure emission is generated, $x(H) \gtrsim x(H_2)$ and the atomic excitation dominates the molecular excitation.

Some of the fine-structure transitions in the postshock gas can become optically thick. Self-absorption in the lines can then reduce the cooling efficiency of the optically thick transitions relative to the optically thin ones (see HM79). HM79 define a column density N_τ which provides a measure of the optical depth in a given transition. Essentially, N_τ is the hydrogen column density required for there to be unit optical depth in the line assuming that a solar abundance of the species is in the lower level of the transition. Thus, N_τ is a lower limit on the column density required for optical depth effects to be important. Hydrogen column densities of warm ($T \gtrsim 100$ K) postshock gas can reach 10^{22-23} cm^{-2} behind dense ($n_0 \gtrsim 10^5$ cm^{-3}) shocks. The last column of Table 9 gives N_τ for the fine-structure transitions, and we see that numerous transitions may become optically thick behind such shocks. On the other hand, N_τ for the metastable transitions all exceed $\sim 10^{21}$ cm^{-2}, which is much greater than the column $N \lesssim 10^{20}$ cm^{-2} of hot ($T \gtrsim 5000$ K) gas which produces the metastable emission. These photons can readily escape, therefore, in the upstream direction.

REFERENCES

Aannestad, P. 1973 *Ap. J. Suppl.*, **25**, 223.
Allen, C. W. 1983, *Astrophysical Quantities* (3d ed.; London: Athlone).
Aller, L. H. 1984, *Physics of Thermal Gaseous Nebulae* (Dordrecht: Reidel).
Amano, A. 1988, *Ap. J.* (*Letters*), in press.
Aldrovandi, S. M. V., and Pequinot, D. 1973, *Astr. Ap.*, **25**, 137 (AP73).
Anicich, V. G., and Huntress, W. T. 1986, *Ap. J. Suppl.*, **62**, 553 (AH86).
Bahcall, J. N., and Wolf, R. A. 1968, *Ap. J.*, **152**, 701.
Bally, J., and Lada, C. J. 1983, *Ap. J.*, **265**, 824.
Bates, D. R. 1986, *Ap. J.* (*Letters*), **306**, L45 (B86).
Bates, D. R., Kingston, A. W., and McWhirter, R. W. P. 1962, *Proc. Roy. Soc. London A*, **267**, 297.
Berrington, K. A., Burke, P. G., Freitas, L. C. G., and Kingston, A. E. 1985, *J. Phys. B.*, **18**, 4135.
Bieniek, R. J., and Dalgarno, A. 1979, *Ap. J.*, **228**, 635.
Black, J. H., and Dalgarno, A. 1973, *Ap. J.* (*Letters*), **184**, L102 (BD73).
———. 1976, *Ap. J.*, **203**, 132.
Black, J., Porter, A., and Dalgarno, A. 1981, *Ap. J.*, **249**, 138.
Blais, N. C., and Truhler, D. G. 1982, *Ap. J.* (*Letters*), **258**, L79.
Brocklehurst, M. 1971, *M.N.R.A.S.*, **153**, 471.
Burke, P. G., and Taylor, K. T. 1979, *J. Phys. B*, **12**, 2971 (BT79).
Burton, M. G., Geballe, T. R., Brand, P. W. J. L., and Webster, A. S. 1988, *M.N.R.A.S.*, **231**, 617.
Burton, M. G., Hollenbach, D. J., Haas, M., and Erickson, E. 1989, in preparation.
Chernoff, D. F., Hollenbach, D. J., and McKee, C. F. 1982, *Ap. J.* (*Letters*), **259**, L97.
———. 1989, in preparation.
Cohen, M., Hollenbach, D. J., Haas, M. R., and Erickson, E. F. 1988, *Ap. J.*, **329**, 863.
Corrigan, S. J. B. 1965, *J. Chem. Phys.*, **43**, 4381.
Cox, D. P. 1972, *Ap. J.*, **178**, 143.
Cox, D. P., and Raymond, J. C. 1985, *Ap. J.*, **298**, 651.
Czyzak, S. J., Kreuger, T. K., Martins, P., Saraph, H. E., Seaton, M. J., and Shemming, J. 1968, *IAU Symposium 34, Planetary Nebulae*, ed. C. R. O'Dell and D. Osterbrock (Dordrecht: Reidel), 143.
DeJong, T. 1980, *Highlights Astr.*, **5**, 301.
deNoyer, L. 1979*a*, *Ap. J.* (*Letters*), **228**, L41.
———. 1979*b*, *Ap. J.* (*Letters*), **232**, L165.
Dewangen, D. P., and Flower, D. R. 1982, *M.N.R.A.S.*, **199**, 457.
Dopita, M. A. 1977, *Ap. J. Suppl.*, **33**, 437.
Dove, J. E., and Mandy, M. E. 1986, *Ap. J.* (*Letters*), **311**, L93.
Dove, J. E., Rusk, A. C. M., Cribb, P. H., and Martin, P. G. 1987, *Ap. J.*, **318**, 379.
Draine, B. T. 1980, *Ap. J.*, **241**, 1021.
Draine, B. T., and Katz, N. 1986, *Ap. J.*, **306**, 655 (DK86).
Draine, B. T., Roberge, W. G., and Dalgarno, A. 1983, *Ap. J.*, **264**, 485 (DRD).
Draine, B. T., and Sutin, B. 1987, *Ap. J.*, **320**, 803.
Drawin, H. W. 1969, *Zs. Phys.*, **225**, 483.
Elitzur, M., Hollenbach, D. J., and McKee, C. F. 1989, *Ap. J.*, submitted.
Fahey, D. W., Fehsenfeld, F. C., Ferguson, E. E., and Viehland, L. A. 1981, *J. Chem. Phys.*, **75**, 3365 (FFFV81).
Federman, S. R., and Shipsey, E. J. 1983, *Ap. J.*, **269**, 791.
Fleischmann, H. H., and Young, R. A. 1969, *Phys. Rev.*, **178**, 254.
Flower, D., Pineau, des Fôrets, J., and Hartquist, T. 1986, *M.N.R.A.S.*, **218**, 729.
Garstang, R. H. 1958, *M.N.R.A.S.*, **118**, 572.
———. 1962, *M.N.R.A.S.*, **124**, 321.
———. 1964, *J. Res. NBS*, **68A**, 61.
———. *IAU Symposium 34, Planetary Nebulae*, ed. C. R. O'Dell and D. Osterbrock (Dordrecht: Reidel).
Gealy, M. W., and van Zyl, B. 1987, *Phys. Rev. A*, **36**, 3100 (GvZ97).
Geballe, T. R., and Garden, R. 1987, *Ap. J.* (*Letters*), **317**, L107.
Giles, K. 1977, *M.N.R.A.S.*, **180**, 57P.
Giovanardi, C., Natta, A., and Palla, F. 1987, *Astr. Ap. Suppl.*, **70**, 269.
Graham, J. R., Wright, G. S., and Longmore, A. J. 1987, *Ap. J.*, **313**, 847.
Grevesse, N., Nussbaumer, H., and Swings, J. P. 1971, *M.N.R.A.S.*, **151**, 239.
Haas, M. R., Hollenbach, D. J., and Erickson, E. F. 1986, *Ap. J.* (*Letters*), **301**, L57.
Harris, A. W., Gry, C., and Bromage, G. E. 1984, *Ap. J.*, **284**, 157.
Hartigan, P., Raymond, J., and Hartmann, L. 1987, *Ap. J.*, **316**, 323.

Hasegawa, T., and Akabane, K. 1984, *Ap. J. (Letters)*, **287**, L91.
Henry, R. J. W., Burke, P. G., and Sinfailem, A. L. 1969, *Phys. Rev.*, **178**, 218.
Herbst, E. 1985, *Ap. J.*, **291**, 226 (H85).
Hickman, A. P. 1987, *J. Phys. B.*, **20**, 2091 (H87).
Hollenbach, D. J. 1982, *Ann. of NY Acad. Sci.*, **395**, 242.
———. 1985, *Icarus*, **61**, 36.
———. 1988, *Astr. Letters and Comm.*, **26**, 191.
Hollenbach, D. J., and McKee, C. F. 1979, *Ap. J. Suppl.*, **41**, 555 (HM79).
Kieffer, L. J. 1969, *Atomic Data*, **1**, 19 (K69).
Launay, J.-M., and Roueff, E. 1977*a*, *Astr. Ap.*, **56**, 289.
———, 1977*b*, *J. Phys. B*, **10**, 879.
Lee, L. C. 1984, *Ap. J.*, **282**, 172 (L89).
Lepp, S., and Shull, J. M. 1983, *Ap. J.*, **270**, 578.
Mac Low, M.-M., and Shull, J. M. 1986, *Ap. J.*, **302**, 585.
Mark, T. D. 1975, *J. Chem. Phys.*, **63**, 3731 (M75).
Mark, T. D., and Egger, F. 1976, *Internat. J. Mass. Spectrom. Ion Phys.*, **20**, 89 (ME79).
Mathis, J. S., Rumpl, W., and Nordsieck, K. H. 1977, *Ap. J.*, **217**, 425 (MRN).
McKee, C. F., Chernoff, D., and Hollenbach, D. J. 1984, in *Proc. 16th ESLAB Symposium, Galactic, and Extragalactic Infrared Spectroscopy*, ed. M. Kessler and J. Phillips (Dordrecht: Reidel), p. 103.
McKee, C. F., and Hollenbach, D. J. 1987, *Ap. J.*, **322**, 275.
McKee, C. F., Hollenbach, D. J., Seab, C. G., and Tielens, A. G. G. M. 1987, *Ap. J.*, **318**, 674.
McKee, C. F., Storey, J. W. V., Watson, D. M., and Green, S. 1982, *Ap. J.*, **259**, 647.
Millikan, R. C., and White, D. R. 1963, *J. Chem. Phys.*, **39**, 3209.
Monteiro, T. S., and Flower, D. R. 1987, *M.N.R.A.S.*, **228**, 101.
Mouschovias, T. 1976, *Ap. J.*, **207**, 141.
Myers, P. C. 1987, in *Interstellar Processes*, ed. D. J. Hollenbach and H. A. Thronson (Dordrecth: Reidel), p. 71.
Neufeld, D. 1987, Ph.D. thesis, Harvard University,
Neufeld, D., and McKee, C. F. 1988, *Ap. J. (Letters)*, **331**, L87.
Nussbaumer, H., and Storey, P. J. 1980, *Astr. Ap.*, **89**, 308.
———. 1982, *Astr. Ap.*, **110**, 295.
Osterbrock, D. E. 1974, *Astrophysics of Gaseous Nebulae* (San Francisco: Freeman).
Peterson, R., and Eisner, M. 1973, *Phys. Rev. A*, **8**, 1289.
Pikel'ner, S. B. 1954, *Izv. Krym. Astrofiz. Obs.*, **12**, 94.
Prasad, S. S. 1986, private communication (P86).
Prasad, S. S., and Huntress, W. T. 1980, *Ap. J. Suppl.*, **43**, 1 (PH80).
Rapp, D., and Englander-Golden, P. 1965, *J. Chem. Phys.*, **43**, 1464 (REG65).
Raymond, J. C. 1979, *Ap. J. Suppl.*, **39**, 1.
Raymond, J. C., Black, J. H., Dupree, A. K., Hartmann, L., and Wolff, R. S. 1980, *Ap. J.*, **238**, 881.
Roberge, W., and Dalgarno, A. 1982, *Ap. J.*, **255**, 176.
Schinke, R., and Andreson, P. 1984, *J. Chem. Phys.*, **81**, 5644.
Schinke, R., Engel, V., Buck, U., Meyer, H., and Dierksen, G. H. F. 1985, *Ap. J.*, **299**, 939.
Schwartz, R. D. 1983, *Ann. Rev. Astr. Ap.*, **21**, 209.
Seab, C. G., Shull, J. M., and McKee, C. F. 1989, in preparation.
Shapiro, P. R., and Kang, H. 1987, *Ap. J.*, **318**, 32.
Shoub, E. C. 1977, *Ap. J. Suppl.*, **34**, 259.
Shull, J. M. 1980, *Ap. J.*, **237**, 769.
Shull, J. M., and Draine, B. T. 1987, in *Interstellar Processes*, ed. D. J. Hollenbach and H. A. Thronson (Dordrecht: Reidel), p. 283.
Shull, J. M., and Hollenbach, D. J. 1978, *Ap. J.*, **220**, 525.
Shull, J. M., and McKee, C. F. 1979, *Ap. J.*, **227**, 131.
Smith, D., and Adams, N. G. 1984, *Ap. J. (Letters)*, **284**, L13 (SA84).
Spitzer, L., and Scott, E. H. 1969, *Ap. J.*, **158**, 161.
Sternberg, A., and Dalgarno, A. 1988, *Ap. J.*, **338**, 197.
Sutherland, C. D., and Zinn, J. 1975, Los Alamos Informal Rept.-6055MS (SZ75).
Thompson, R. 1973, *Ap. J.*, **181**, 1039.
Tielens, A. G. G. M. 1989, in *Proc. Internat. Conf. on Submillimeter and Millimeter Astronomy*, ed. A. Webster (Dordrecht: Kluwer), in press.
Tielens, A. G. G. M., and Hollenbach, D. 1985*a*, *Ap. J.*, **291**, 722.
———. 1985*b*, *Ap. J.*, **291**, 747.
Vance, D. W., and Bailey, T. L. 1966, *J. Chem. Phys.*, **44**, 486 (VB66).
van Dishoeck, E. F. 1987, in *IAU Symposium 120, Astrochemistry*, ed. M. S. Vardya and S. P. Tarafdar (Dordrecht: Reidel), p. 51.
Van Dishoeck, E. F., and Black, J. H. 1986, *Ap. J. Suppl.*, **62**, 109 (vDB86).
———. 1987, in *Physical Processes in Molecular Clouds*, ed. G. Morfill, (Dordrecht: Reidel), p. 225.
———. 1988, *Ap. J.*, **334**, 711.
Van Dishoeck, E. F., and Dalgarno, A. 1983, *J. Chem. Phys.*, **79**, 873 (vDD83).
van Regemorter, H. 1962, *Ap. J.*, **136**, 906.
Van Steenberg, M. E., and Shull, J. M. 1988, *Ap. J.*, **330**, 942.
Viscuso, P., and Chernoff, D. 1988, *Ap. J.*, **327**, 364.
von Rosenberg, C. W., Taylor, R. L., and Teare, J. D. 1971, *J. Chem. Phys.*, **54**, 1974.
Wagner, A. F., and Graff, M. M. 1987, *Ap. J.*, **317**, 423 (WG87).
Werner, M. W., Crawford, M. K., Genzel, R., Hollenbach, D. J., Townes, C. H., and Watson, D. M. 1984, *Ap. J. (Letters)*, **282**, L81.
Wheeler, J. C. Mazurek, T. J., and Sivaramakrishnan, A. 1980, *Ap. J.*, **237**, 781.
Wiese, W. L., Smith, M. W., and Glennon, B. M. 1966, *Atomic Transition Probabilities*, Vol. **1**, NSRDS-NBS4, (Washington, DC: US GPO).
Wiese, W. L., Smith, M. W., and Miles, B. M. 1969, *Atomic Transition Probabilities*, Vol. **2**, NSRDS-NBS22, (Washington, DC: US GPO).

DAVID HOLLENBACH: Mail Stop 245-6, NASA Ames Research Center, Moffett Field, CA 94035

CHRISTOPHER MCKEE: Department of Physics, University of California, Berkeley, Berkeley, CA 94720